2023

# Investigation of microstructurally dependent mechanical properties of cold sprayed copper using correlative microscopy

Quintin Otto
n01408900@unf.edu

# Investigation of Microstructurally Dependent Mechanical Properties of Cold Sprayed Copper Using Correlative Microscopy

By

Quintin Otto


A thesis submitted to the School of Engineering

in partial fulfillment of the requirements for the degree of

Master of Science in Mechanical Engineering

University of North Florida

COLLEGE OF COMPUTING, ENGINEERING, and CONSTRUCTION

May 2023

The thesis “Investigation of Microstructurally Dependent Mechanical Properties of Cold Sprayed Copper Using Correlative Microscopy” submitted by Quintin Otto in partial fulfillment of the requirements for the degree of Master of Science in Mechanical Engineering has been

**Approved by the thesis committee:** **Date**

_____ _____

Dr. Paul Eason

Thesis Advisor and Committee Chairperson

_____ _____

Dr. Stephen Stagon

_____ _____

Dr. Grant Bevill

Accepted for the School of Engineering:

_____ _____

Dr. Alan Harris

Director of the School of Engineering

Accepted for the College of Computing, Engineering, and Construction:

_____ _____

Dr. William Klostermeyer

Dean of the College

Accepted for the University:

_____ _____

Dr. John Kantner

Dean of the Graduate School

# Dedication

This thesis is dedicated to my family, friends, professors, and mentors that have generously aided and supported me throughout my education journey. I especially want to thank my girlfriend Taylor Graham, for directly supporting me during my time at UNF. The gratitude I have for your support goes beyond words and I sincerely could not have accomplished this without you.

# Acknowledgements

I would like to acknowledge my advisor Dr. Eason for providing me an opportunity to work in MSERF as an undergraduate student, but more importantly allowing me to pursue a graduate education under the accelerated program. Conducting research in an incredibly limited time frame while also participating in summer internships is not something most advisors would recommend or allow their students to undertake. Dr. Eason had the confidence I would be able to accomplish this task and I am especially grateful. I would also like to thank Dr. Brian Wingender and Dr. Albina Mikhaylova for assisting me throughout my time working and researching at MSERF. I would like to acknowledge the mechanical engineering faculty and staff who have graciously helped me during my education journey. I specifically want to thank my advisor Sue Levin who helped me navigate the difficult logistical challenge of accomplishing a graduate degree in a single year. Lastly, I would like to acknowledge Molly Dobrow, Reed Harper, and Kenny Bowman, I am grateful for the time we spent working together, I appreciate your help, and I wish everyone the best in their future endeavors.

# Table of Contents

List of Figures ..... 9

List of Tables ..... 14

Symbols and Abbreviations ..... 15

Abstract ..... 16

Chapter 1: Introduction ..... 17

Chapter 2: Literature Review ..... 20

2.0 Introduction to Cold Spray ..... 20

2.1 Applications of Cold Spray ..... 23

2.2 Cold Spray Process Parameters ..... 25

2.2.1 Critical Velocity ..... 26

2.2.2 Process Gas ..... 29

2.2.3 Temperature ..... 30

2.2.4 Process Powder ..... 32

2.3 Interparticle Bonding ..... 34

2.4 Cold Rolling and The Relationship to Cold Spray ..... 38

2.5 Microstructure of Cold Spray ..... 40

2.5.1 Hall-Petch Relationship to Cold Spray ..... 43

2.6 Mechanical Property Evaluation ..... 44

2.7 Microscopy and Microstructural Characterization ..... 46

2.8 Scanning Probe Microscopy ..... 48

Chapter 3: Experimental Methods ..... 50

3.0 Methodology and Experimental Process ..... 50

3.0.1 Materials ..... 53

3.1 Metallographic Specimen Preparation....54
3.2 Scanning Electron Microscopy and Electron Back Scattered Diffraction Image Collection....56
3.3 Pre-Indented Image Collection....57
3.3.1 High Magnification Individual Pre-Indent Imaging....58
3.3.2 Electron Back Scattered Diffraction Pre-Indent Imaging....59
3.3.3 Low Magnification Secondary and Backscattered Electron Pre-Indent Imaging....60
3.4 Physical Measurements: Microhardness....61
3.4.1 Process for Correlating Pre and Post Indent Images....63
3.5 Scanning Probe Microscopy....64
3.6 Area Fraction Analysis Process Using Image-J....64
Chapter 4: Results and Discussion....66
4.0 Results Introduction....66
4.0.1 Polishing Procedure Discussion....66
4.1 Microstructure of Cold Sprayed Material....68
4.1 Characterization of Pressed Powder Material....73
4.2 EBSD Results and Analysis – Cold Spray....76
4.3 EBSD Results and Analysis – Pressed Powder....79
4.4 High Magnification Images and Indentation of Cold Spray Material....80
4.4.1 High Magnification Images and Indentation of Pressed Powder....86
4.5 Spray Direction and Transverse Direction Cold Spray EBSD and Indentation Arrays....89
4.6 Low Magnification Images and Indent Arrays....95
4.7 Hardness and Area Fraction Results....98
4.7.1 Associated Microhardness Data for High Magnification Images....99
4.7.2 Associated Microhardness Data for EBSD Images....100

4.7.3 Associated Microhardness Data for Low Magnification Images ..... 101
4.7.4 Combined Microhardness Data. ..... 102
4.7.5 Considering the Volume of an Indent ..... 105
4.8 Scanning Probe Microscopy ..... 106
4.8.1 Nano 3D Mechanical Mapping ..... 110
Chapter 5: Conclusions and Future Works ..... 115
References ..... 117
Appendix ..... 123
A.1.0 Additional Indentation Images ..... 123
A.1.0.1 Spray Direction Cold Spray High Magnification Images ..... 123
A.1.0.2 Transverse Direction Cold Spray High Magnification Images ..... 124
A.1.0.3 EBSD Array Cold Spray Indentation Images ..... 126
A.1.0.4 Low Magnification Indentation Images ..... 128
A.2.0 Cold Rolled Microstructural Characterization ..... 130
A.2.1 Cold Rolled High Magnification Imaging and Indentation ..... 132
A.2.2 Cold Rolled EBSD and Indentation Arrays ..... 135
A.2.3 Cold Rolled Low Magnification Indentation Arrays ..... 139
A.2.4 Cold Rolled Hardness Data ..... 140

# List of Figures

Figure 1 Cold Spray Publications and Citations by year from 1998 to 2021. [14] .....18

Figure 2 Cold Spray process flow diagram. [20] .....21

Figure 3 Descending images capturing several phases of the CS process; (a.) A vertically oriented CS system showing each component as well as the substrate. (b.) Illustrates particle deposition with size, velocity, and rebounding particles. (c.) Shows the microstructure including grains and pores (i-iii). (d.) Magnification down to individual dislocations within the microstructure. (e.) Scale bar for comparison from macro to nanoscopic features. [23] .....22

Figure 4 GE T700 front frame housing showing cold spray restoration process. [6].....25

Figure 5 Empirically determined critical velocities to illicit adhesion for several common metals using 25 µm sized particles. Dark gray region is range of uncertainty. [36] .....27

Figure 6 Deposition efficiency as a function of mean particle velocity (Copper Feedstock) showing a comparison between model and experimental results. [37] .....28

Figure 7 Diagram comparing adhesion conditions of CS showing that hardness of feedstock in relation to the hardness of the substrate affects adhesion. Soft feedstock and a soft substrate produce the best scenario. [16] ...29

Figure 8 Optical images of coating thickness of copper cold sprayed compacts compared to pre-heat temperature. Demonstrates that an increase in temperature increased coating thickness and deposition efficiency. (a.) 25°C. (b.) 100°C. (C.) 200°C. (d.) 300°C. [41].....31

Figure 9 Gas Atomization system for metallic powder preparation. [43] .....32

Figure 10 Electron Microscope image showing copper feedstock morphology for 15 - 38 µm size particles produced by gas atomization. Arrows indicate spherical and aspherical shaped powder particles. [2] .....34

Figure 11 Illustration of dislocation cloud forming in CS particle 10 ps after impact with uniform upper half. [46] ..36

Figure 12 Illustration of CS particle after contact with substrate showing jetting zones occurring at the perimeter of the particle-substrate interface. [46] .....37

Figure 13 Schematic of a Cold Rolling mill. [50] .....39

Figure 14 Characteristic deformation regimes resulting from cold sprayed copper. Arrows indicate high deformation and low deformation regions (BSE). .....41

Figure 15 Micrographs of Copper CS deposits following bidirectional spray patters. Top row (a,b,c), As-Sprayed CS deposits a: Spray Direction, b&c Transverse Direction. Bottom Row (d,e,f), Annealed CS Deposits d: Spray direction, e&f: Transverse Direction. [2].....42

Figure 16 Micrograph of Vickers microhardness indent on CS Aluminum material showing multiple nano-scaled grains captured within indent region. .....46

Figure 17 Electron Back Scattered Diffraction schematic with major components labeled. [60] .....47

Figure 18 Atomic Force Microscope schematic with major components labeled. [62] .....49

Figure 19 Force curve and nano 3D map of copper surface taken on Shimadzu 9700HT SPM. .....49

Figure 20 Flow chart of experimental process. Each section is color coded to indicate a separate procedure with a subsequent methodological flow chart. .....50

Figure 21 Illustrates the process of image and hardness data acquisition. (1.) Individual indents using high magnification pre-indent images for analysis. (2.) 9 indents using pre-indent EBSD inverse pole figures. (3.) 12 indents using low magnification pre-indent images.....51

Figure 22 Flow chart showing (a.) as-received material, and (1-3) Metallographic preparation process. .....54

Figure 23 Example of specimen on 12.7 mm SEM stub post ion mill – (Cold spray transverse direction sample shown). .....55

Figure 24 Pre-indentation micrograph collection process. .....57

Figure 25 High resolution pre-indentation image taken in BSE. CS spray direction shown. Arrow indicates the typical size of a single indent - 22x22µm. .....58

Figure 26 Example showing pre-indented EBSD pole figure with 175 µm field of view of CS specimen in Spray direction. Arrow indicates the typical size of a single indent - 22x22 µm. .....59

Figure 27 Backscattered electron micrograph of pre-indented microstructure (185 µm field of view). Arrow indicates typical size of a single indent - 22x22 µm.....60

Figure 28 Target indent location identification flow chart using HMV-G Microhardness tester. .....62

Figure 29 Flow chart showing process for superimposing post-indented image over pre-indented micrograph. .....63

Figure 30 Image-J analysis software with cropped high magnification indent outline. Arrow indicates the polygon selection tool and regions of highly deformed grains outlined by the tool. .....65

Figure 31 SE micrograph of CS material oriented in the spray direction. Arrows indicate the characteristic high and low deformation regions. Also indicated are two particles that retained their circular shape after splat. .....69

Figure 32 BSE micrograph of CS material in the spray direction. Arrows indicate regions during deposition where particles did not completely adhere as well as twinned grains spread throughout the microstructure. .....70

Figure 33 SE micrograph of CS material in transverse direction. Arrows indicate particle stacking regions as well as low deformation and high deformation regions. .....71

Figure 34 BSE micrograph of CS material shown in transverse direction. Arrows indicate tie-dye region. .....72

Figure 35 BSE micrograph of CS material with arrows indicating tie-dye region next to contrasting grain structure – (transverse direction). .....73

Figure 36 BSE micrograph of powder pressed specimen. Arrows indicate porosity as well as twinned grains throughout the microstructure. .....74

Figure 37 SE micrograph of pressed powder showing less topography than the sprayed material. .....75

Figure 38 CS sample oriented in the transverse direction. (Top) Band contrast image with high deformation region highlighted. (Bottom) Inverse pole figure in Z-direction - Arrows indicates tie-dye regions. .....77

Figure 39 CS sample oriented in the spray direction. (Top) Band contrast image with arrow indicating high deformation region. (Bottom) Inverse pole figure in Z-direction. .....78

Figure 40 EBSD figures for pressed powder. (Top) Band Contrast. (Bottom) Inverse Pole Figure in Z-Direction.....79

Figure 41 Indent #8 shown in BSE from the high magnification images with outline of indent over pre-indented microstructure (Spray Direction CS) - Arrow indicates high deformation region.....81

Figure 42 Indent #2 shown in BSE from the high magnification images with outline of indent over pre-indented microstructure (Spray Direction CS) – Arrow indicates low deformation region. .....82

Figure 43 (a.) High and (b.) Low, HV values for 10 high magnification image and indent series on spray direction CS Specimens - Images taken in BSE.....83

Figure 44 Indent #2 shown in BSE from the High magnification images with outline of indent over pre-indented microstructure (Transverse Direction CS) - Arrow indicates low deformation region. .....84

Figure 45 Indent #9 shown in BSE from the high magnification images with outline of indent over pre-indented microstructure (Transverse Direction CS) - Arrow indicates low deformation region. .....85

Figure 46 (a.) High and (b.) Low, HV values for 10 high magnification image and indent series on Transverse Direction CS Specimens. Arrow indicates lack of adhesion on figure (b.) Images taken in BSE. .....86

Figure 47 Indents 1-5 from the high magnification images with outlines of indents over pre-indented microstructure (pressed powder). Image taken in BSE. .....87

Figure 48 Indents 6-10 from the high magnification images with outlines of indents over pre-indented microstructure (pressed powder). Image taken in BSE. .....88

Figure 49 Band contrast EBSD figure showing CS spray direction. Outlines of each Vickers microhardness indent and their associated microhardness values are indicated. Arrows indicate HDRs captured within the 3 indents with the highest microhardness values in the array. .....90

Figure 50 Inverse pole figure in Z-direction showing CS spray direction specimen. Outlines of each Vickers microhardness indent and their associated microhardness values are indicated. .....91

Figure 51 Band contrast EBSD figure of CS transverse direction specimen with outlines of 3x3 indent array and their associated Vickers microhardness values.....93

Figure 52 Inverse pole figure in Z-direction of CS transverse direction specimen with indent outlines of 3x3 array and their associated Vickers microhardness values. .....94

Figure 53 BSE Micrograph of 12 microhardness indent outlines for CS spray direction specimen. Each outline is numbered with their associated microhardness value. .....96

Figure 54 BSE Micrograph of 12 microhardness indent outlines for CS transverse direction specimen. Each outline is numbered with their associated microhardness value. .....97

Figure 55 Graph comparing Vickers microhardness to percentage of high deformation captured within the indent region. (a.) CS Spray Direction. (b.) CS Transverse Direction.....104

Figure 56 Transverse direction CS BSE micrograph with cross sectional visualization of potential indent placed on the spray direction surface. Arrows indicate the preferential powder particle stacking seen in the transverse direction sample. .....106

Figure 57 (Top) CS Spray direction deflection image in tapping mode. (Bottom) 3D view of spray direction sample in tapping mode showing sample height and topography. .....108

Figure 58 (Top) CS Transverse direction deflection image in tapping mode. (Bottom) 3D view of transverse direction sample in tapping mode showing sample height and topography. .....109

Figure 59 (Top) Deflection image taken in contact mode with nano mapping window highlighted over single grain - Spray direction CS specimen. (Bottom) 3D nano mechanical map for grain in highlighted window. .....111

Figure 60 (Top) Deflection image taken in contact mode with nano mapping window highlighted over many small grains - Spray direction CS specimen. (Bottom) 3D nano mechanical map for highly deformed grains in highlighted window. .....112

Figure 61 (Top) Deflection image taken in contact mode with nano mapping window highlighted over single grain - Transverse direction CS specimen. (Bottom) 3D nano mechanical map for grain in highlighted window.....113

Figure 62 (Top) Deflection image taken in contact mode with nano mapping window highlighted over many small grains - Transverse direction CS specimen. (Bottom) 3D nano mechanical map for highly deformed grains in highlighted window. .....114

Figure 63 High Magnification CS pre-indentation images in spray direction with associated microhardness values (BSE).....123

Figure 64 High Magnification CS post-indentation images in spray direction with associated microhardness values (BSE).....124

Figure 65 High Magnification CS pre-indentation images in transverse direction with associated microhardness values (BSE).....124

Figure 66 High Magnification CS post-indentation images in transverse direction with associated microhardness values (BSE).....125

Figure 67 Post-indentation CS image of EBSD 3x3 Array in spray direction with associated microhardness values (BSE).....126

Figure 68 Post-indentation CS image of EBSD 3x3 Array in transverse direction with associated microhardness values (BSE).....127

Figure 69 Post-indentation CS image of low magnification 4x3 Array in spray direction with associated microhardness values (BSE).....128

Figure 70 Post-indent CS image of low magnification 4x3 array in transverse direction with associated microhardness values (BSE).....129

Figure 71 BSE micrograph of CR specimen oriented in the normal direction. Arrow indicates tie-dye grain structure. .....131

Figure 72 SE micrograph of CR specimen. Arrow indicates dimple structure from possible mechanical pullout during polishing. .....132

Figure 73 BSE Micrograph of 8 microhardness indent outlines for CR normal direction specimen. Each outline is numbered with their associated microhardness value (BSE). .....133

Figure 74 BSE Micrograph of 2 microhardness indent outlines for CR normal direction specimen. Each outline is numbered with their associated microhardness value. .....134

Figure 75 CR specimen oriented in normal direction - (Top) Band contrast image - (Bottom) Z-Direction Pole figure. .....136

Figure 76 Band contrast image of normal direction CR specimen with indent outline for 3x3 array and associated Vickers microhardness values.....137

Figure 77 Z-Direction EBSD Pole figure for normal direction CR specimen with indent outline for 3x3 array and associated Vickers microhardness values.....138

Figure 78 CR specimen with indent outline for 3x3 array and associated Vickers microhardness values (BSE).....139

# List of Tables

Table 1 Comparison of typical metals and their respective strain hardening exponent. [49] .....40

Table 2 Image and Indent collection table. .....52

Table 3 Mechanical polishing procedure for copper specimens used in the experiment. .....55

Table 4 Associated Vickers microhardness data for CS Spray direction high magnification images. .....99

Table 5 Associated Vickers microhardness data for CS Transverse direction high magnification images. .....99

Table 6 Associated Vickers microhardness data for Pressed powder high magnification images. .....100

Table 7 Associated Vickers microhardness data for CS Spray direction EBSD images. .....100

Table 8 Associated Vickers microhardness data for CS Transverse direction EBSD images. .....101

Table 9 Associated Vickers microhardness data for CS Spray direction low magnification images. .....101

Table 10 Associated Vickers microhardness data for CS Transverse direction low magnification images. .....102

Table 11 Microhardness data totals and statistics. .....103

Table 12 Associated Vickers microhardness data for CR high magnification images. .....140

Table 13 Associated Vickers microhardness data for CR EBSD images. .....141

Table 14 Associated Vickers microhardness data for CR low magnification images. .....141

# Symbols and Abbreviations

ASI – Adiabatic Shear Instability

ARL – Army Research Laboratory

DE – Deposition Efficiency

FCC – Face Centered Cubic

FIB – Focused Ion Beam

FOV – Field of View

BSE – Backscattered Electron

MSERF – Materials Science and Engineering Research Facility

CFD – Computational Fluid Dynamics

CR – Cold Rolling

CS – Cold Spray

CSAM – Cold Spray Additive Manufacturing

CV – Critical Velocity

HDR – High Deformation Region

LDR – Low Deformation Region

SE – Secondary Electron

SPD – Severe Plastic Deformation

SPM – Scanning Probe Microscopy

UFG – Ultra Fine Grain

UNF – University of North Florida

UTS – Ultimate Tensile Strength

# Abstract

*This project employs multi-instrument materials characterization to analyze material made with the "Cold Spray" additive manufacturing process. Cold spray is an emerging additive manufacturing technique with unique benefits resulting from its low temperature adhesion process induced by plastic deformation. Metallic powder collides at high speeds creating three dimensional materials and coatings without the need for melting. Copper cold sprayed specimens were analyzed using a series of imaging techniques to characterize the microstructure at varying levels of detail and magnification. Scanning electron microscopy and electron back scattered diffraction were paired with microhardness testing to generate a correlative comparison between microstructure and physical properties of cold sprayed material. This research investigates how microhardness changes across the surface of highly deformed cold sprayed materials and the role inhomogeneous plastic deformation plays in level of microhardness. Both sprayed and transverse orientations were investigated providing a better understanding of the anisotropic mechanical properties created by the cold spray process. Results demonstrated that the cold sprayed microstructure exhibits an increase in microhardness with increasing levels of grain refinement in the sprayed orientation. This correlation was less apparent in the transverse orientation which reinforces the documented evidence that shows as-sprayed cold sprayed materials possess both anisotropic microstructure and properties.*

# Chapter 1: Introduction

The applications for copper metal and its numerous derivatives remain prevalent in engineering and science. The structure, processing, and property relationship is a fundamental aspect of materials science, and the cold-gas dynamic spray process is a unique and modern deposition technique that independently captures all three elements of this relationship. Cold gas dynamic spray or Cold Spray (CS) possesses attractive characteristics surrounding cold worked metal through its adhesion process and subsequent micro and nanostructure. CS involves the acceleration of micron sized metallic particles onto a substrate causing sub-melting temperature, mechanical and metallurgic bonding through severe plastic deformation (SPD) [1]-[4]. Bonding multiple layers of feedstock produces a bulk compact that can be used for a variety of different applications. Invented in the 1980's by scientists at the Institute of Theoretical and Applied Mechanics in Novosibirsk, Russia, CS is now emerging as a practical additive manufacturing technique. Once thought only useful for component repair and surface coatings, CS can now produce viable 3-dimensional structures [5]-[9]. This new development has produced its own subcategory of CS called "Cold Spray Additive Manufacturing" (CSAM) [10]-[12]. Several commercial enterprises are manufacturing CSAM equipment and two notable players in the industry are Titomic and SPEE3D [13]. Both producers have created fully automated systems that produce engineering grade components and parts. Overall, the interest in CS research and application has increased rapidly since its inception and Figure 1 demonstrates this surge with CS publications graphed from 1998 to 2021 [14].

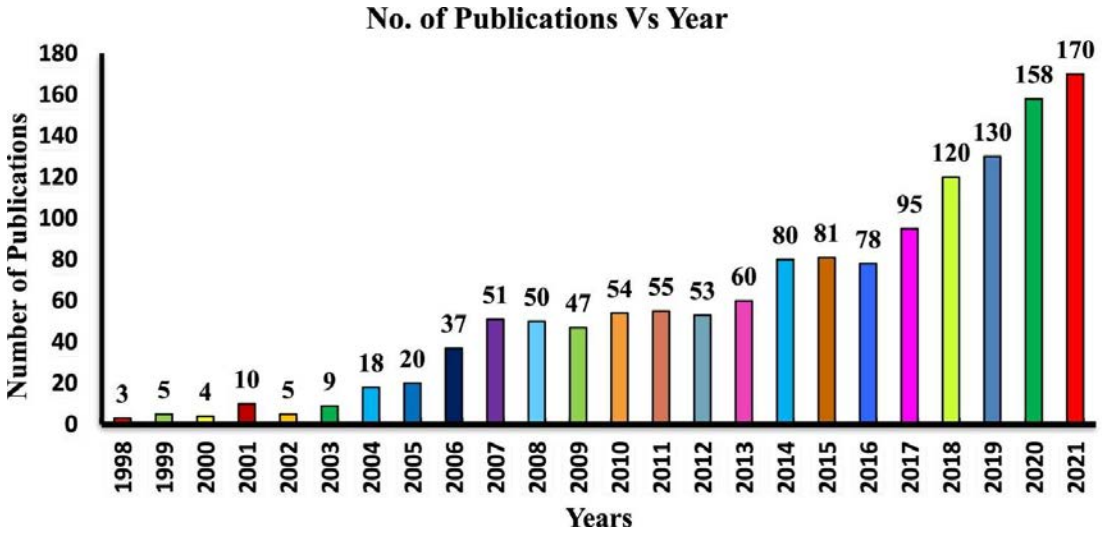


**Figure 1 Cold Spray Publications and Citations by year from 1998 to 2021.** *[14]*

The microstructure produced by the CS process possesses potentially useful characteristics and mechanical properties which are not yet fundamentally understood. CS materials contain an inhomogeneous microstructure with regions exhibiting both high and low levels of plastic deformation. These high plastic deformation regions contain grain size on the order of nanometers and are contrasted by grains often extending several microns in length. This inhomogeneous microstructure limits the capabilities of using noninvasive techniques such as microhardness testing to verify large scale mechanical properties, hindering the industrial capabilities of CS. Additionally, CS material contains high levels of residual cold work, dynamically crystallized grains, porosity, areas of lack of adhesion, and a variety of other prohibitive characteristics including the possibility of an inverse Hall Petch Response. The Hall Petch relationship shows that as grain size decreases yield strength increases. The inverse

occurs when grain reduction reaches a critical size, which further demonstrates the difficulty of characterizing CS material.

The study looks to extend previous works done investigating the inhomogeneity of CS materials using microhardness testing and Copper CS compacts. Copper is an abundant, face centered cubic (FCC), and highly ductile metal, with well characterized structure, processing, and properties relationships. FCC materials contain slip systems that lie along close-packed planes of atoms [15]. These close-packed planes transmit resolved shear stresses more easily causing slip with less required force, lending to its formability. Ductility has a strong impact on adhesion and copper particles impacting a copper substrate presents an optimal case for study [15]. With its well understood properties, copper can be used to aid in the extrapolation of CS properties to other metals.

The experimentation process used a combination of Vickers microhardness tests, Scanning Probe Microscopy (SPM), and Scanning Electron Microscopy (SEM) with Electron Backscattered Diffraction (EBSD). The combination of these techniques allowed for correlation between properties and microstructure using images collected before and after microhardness indentation. It was hypothesized that regions exhibiting a larger fraction of high deformation within the size of the microhardness indent would result in higher levels of microhardness. The CS samples and copper control material used for experimenting were provided by the Penn State Applied Research Laboratory and all testing and characterization was executed at the University of North Florida's (UNF) Materials Science and Research Facility (MSERF).

# Chapter 2: Literature Review

## 2.0 Introduction to Cold Spray

The CS process uses pressurized gas, metallic powder feedstock, and a nozzle (De-Laval) to impact particles onto a substrate [2], [16]-[21]. The working gas, usually consisting of nitrogen, helium, or air enters the system at high pressure and is heated [15]. Increasing the temperature reduces gas viscosity and drag, and thermally softens the metallic feedstock [15]. Particles ranging from 5-45µm in diameter enter the gas and become entrained forming a gas-solid mixture. The entrained mixture enters the converging stage of the nozzle, and the mixture is compressed, increasing its pressure and temperature. Kinetic energy is developed during the expansion phase occurring in the diverging section of the nozzle [17]. The reduction in temperature during expansion causes particles to reach the substrate well below their melting temperature. The particles collide at supersonic speed causing severe plastic deformation (SPD) and consolidation of feedstock material upon impact [15], [16], [20]. During impact the interparticle regions eject material around the periphery of particles called “jetting” [15]. Jetting directly affects interparticle bonding and materials used for CS must be sufficiently ductile to achieve jetting and make good cohesion. Multiple impacts create a dense coating that can rapidly generate a bulk compact. A diagram for a high-pressure CS system is shown in Figure 2 with major components labeled.

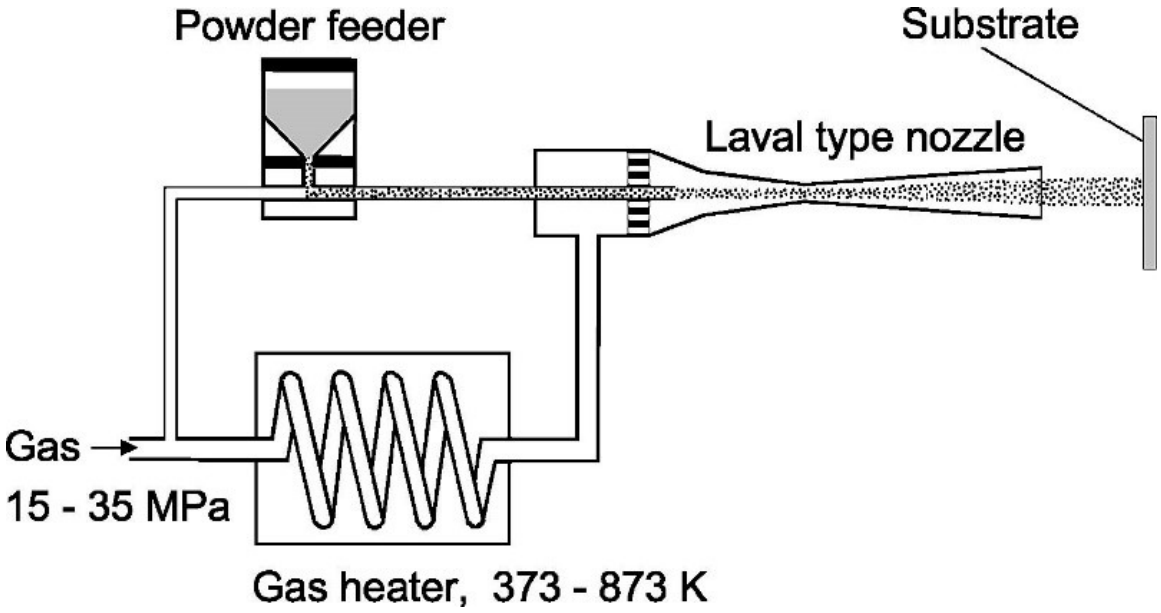


**Figure 2 Cold Spray process flow diagram.** *[20]*

The name “cold” spray stems from the process occurring well below the melting temperature of the material, yet the metallic particles become permanently bonded through a mixture of mechanical and metallurgical mechanisms [16], [21]. Several benefits are exploited by this sub-melting temperature process. By avoiding high temperatures, undesirable problems such as oxidation and brittleness can be avoided [15], [22]. Furthermore, low temperature adhesion allows for porosities of less than 1% to be achieved in sprayed material due to the lack of cooling of liquid metal, which creates pores from the absorption of gasses. [16], [18]. Figure 3 illustrates the entire process further with a series of magnifying graphics that capture each phase of the technique [23].

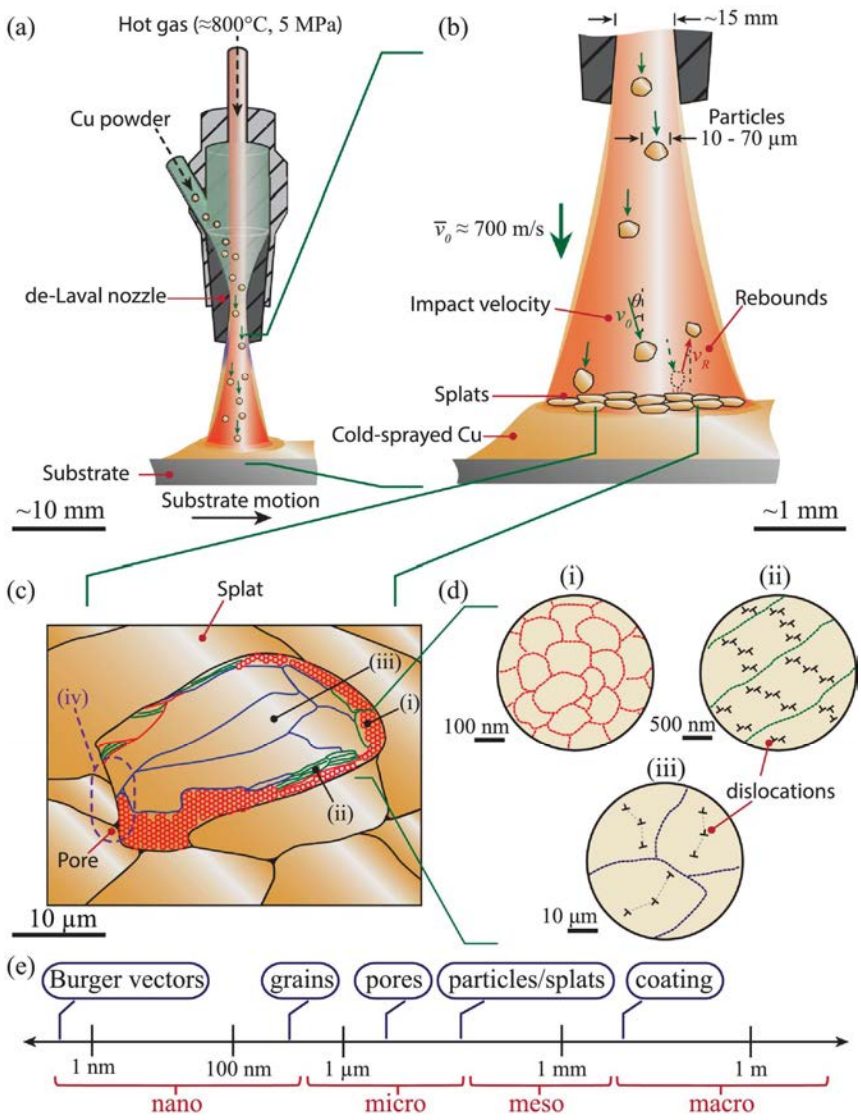


**Figure 3 Descending images capturing several phases of the CS process; (a.) A vertically oriented CS system showing each component as well as the substrate. (b.) Illustrates particle deposition with size, velocity, and rebounding particles. (c.) Shows the microstructure including grains and pores (i-iii). (d.) Magnification down to individual dislocations within the microstructure. (e.) Scale bar for comparison from macro to nanoscopic features.** *[23]*

There are some inherent limitations associated with the CS process. Brittle materials such as glass and ceramics are not viable feedstock choices as they do not exhibit sufficient

ductility to achieve SPD. Additionally, bulk properties of large CS structures don't often retain the same mechanical properties post spray, and high variability of these properties leads to low reliability. Issues associated with extreme strain hardening and low ductility make as-sprayed components poorly suited for structural applications [15]. Cost competitive and high efficiency deposition necessary for industry requires optimized material-dependent process parameters, which are ultimately yet to be determined due to the infancy of the technique. Overall, addressing the limitations, uncovering the fundamental mechanisms involved, and optimizing parameters will continue to increase the industrial viability of CS.

## 2.1 Applications of Cold Spray

Despite the limitations, 3-dimentional structures can still be developed through CS, often called CSAM. For many years, the Army Research Laboratory (ARL) has been exploring the benefits of CSAM technology for Aerospace applications [6]. Aerospace component repair and restoration is of particular interest due to high loads and wear associated with aircraft, coupled with unique materials, and complicated geometry [6], [24]. Furthermore, magnesium – often used in aerospace components – also suffers from galvanic corrosion and surface weakness [25]. CS deposition using commercially pure aluminum feedstock offers a potential restoration method for magnesium parts, by leveraging corrosion resistant alloys generated from the combination of aluminum and magnesium [25]. Mechanical tests conducted on parts repaired with CSAM aluminum have demonstrated adhesion strengths necessary to certify parts for

flight [11]. Figure 4 shows a CS restoration process of a GE TE700 front frame housing from the as-received condition to final anodization [6].

A variety of other applications have been developed since the inception of the CS process. Corrosion resistant coatings are promising applications for manufacturing or repair requiring adhesion of dissimilar metals. Moreover, low temperature adhesion and minimal oxidation provide excellent adhesion conditions between dissimilar metals [26]. Biomedical applications are also promising, and CS copper coatings can produce anti-bacterial surfaces [12], [27]. Researchers at McGill University reported 99.9% deactivation of COVID-19 virus in 30 minutes on metallic surfaces coated with copper CS [6]. The deposition process associated with CS also proves superior compared to other spray deposition processes and their ability to eliminate pathogens [28]. Champagne et al. compared Plasma, Wire Arc, and CS deposition techniques using copper coated aluminum substrates. MRSA was inoculated onto the surfaces and survivability was calculated after 2 hours. Results demonstrated a 5-order magnitude efficacy in favor of CS deposition [29]. Joint replacements using titanium feedstock are another possibility for CS applications. CS structures provide ideal cell growth conditions increasing biocompatibility and implant stability [6].

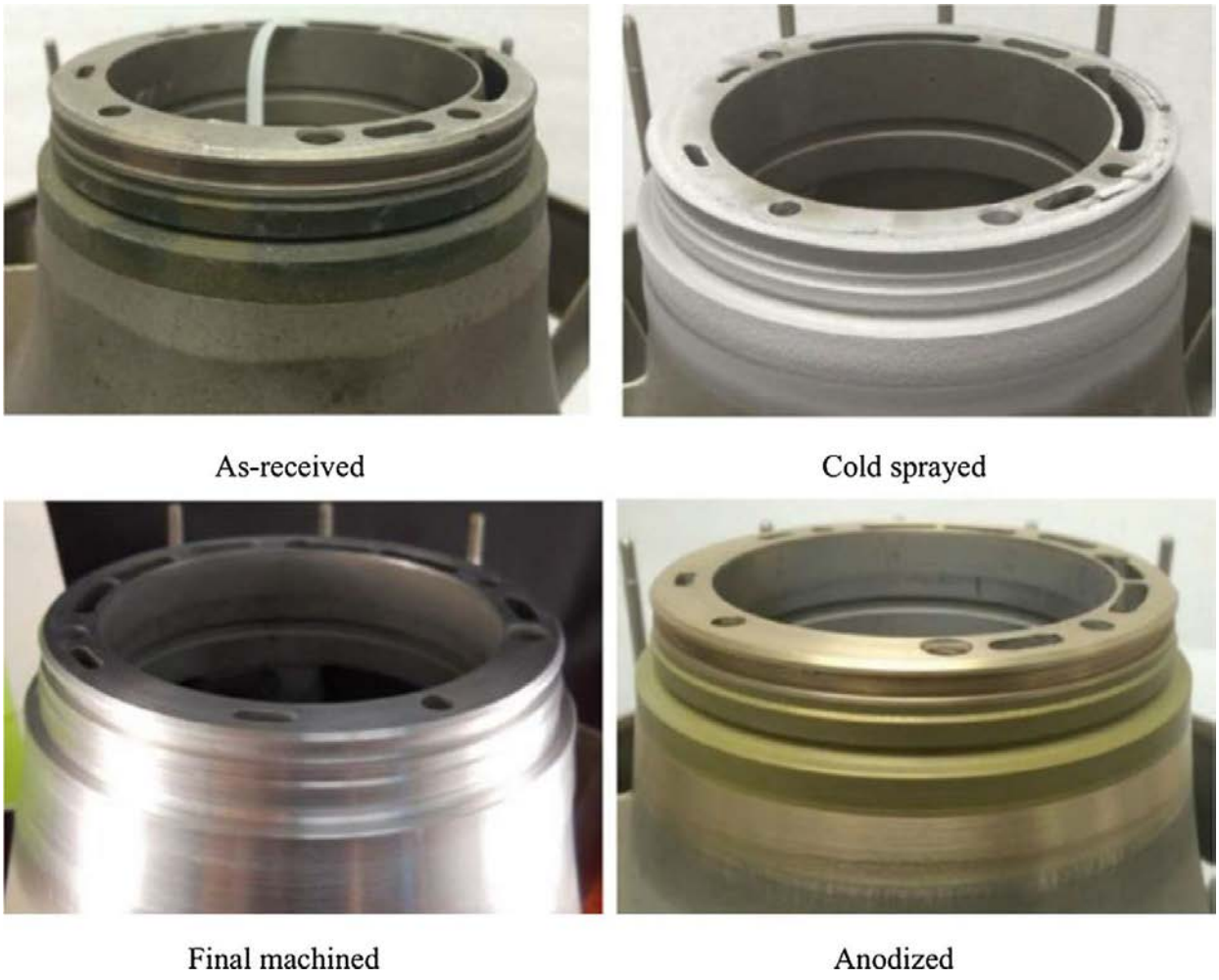


**Figure 4 GE T700 front frame housing showing cold spray restoration process.** *[6]*

## 2.2 Cold Spray Process Parameters

There are variety different process parameters for CS, including carrier gas, gas temperature, particle size, nozzle standoff distance, and particle morphology. All these properties, however, affect particle velocity which is a critical parameter for determining interparticle bonding [1], [16], [30]. Many of these CS process parameters can be manipulated at

the De-Laval Nozzle [15]. The De-Laval Nozzle is a converging-diverging nozzle that compresses a heated acceleration gas which rapidly expands and drives the mixture of gas and feedstock particles towards a substrate [31]. The shape and dimensions of the nozzle play a significant role in determining the impact speed of the particles as well [31], [32]. In most cases, manipulating process parameters has a direct effect on many outcomes such as adhesion probability, porosity, bulk density, tensile strength, hardness, and deposition efficiency [2], [5], [10], [16], [17], [20], [33]. Additional process parameters include the material used for the process powder and the substrate, as well as particle and substrate preheat temperature.

### 2.2.1 Critical Velocity

A threshold value called the "Critical Velocity" (CV) is the primary parameter used to predict interparticle bonding and adhesion. [1], [15], [21], [32], [34]. CV is the speed at which a given particle must reach at impact to illicit adhesion. CV is also material dependent, with harder materials requiring more kinetic energy to successfully adhere or bond [15], [35]. Figure 5 shows a comparison between different metals of 25 µm sized particles and their CV's. The uncertainty is plotted in black near the upper end of the range [36].

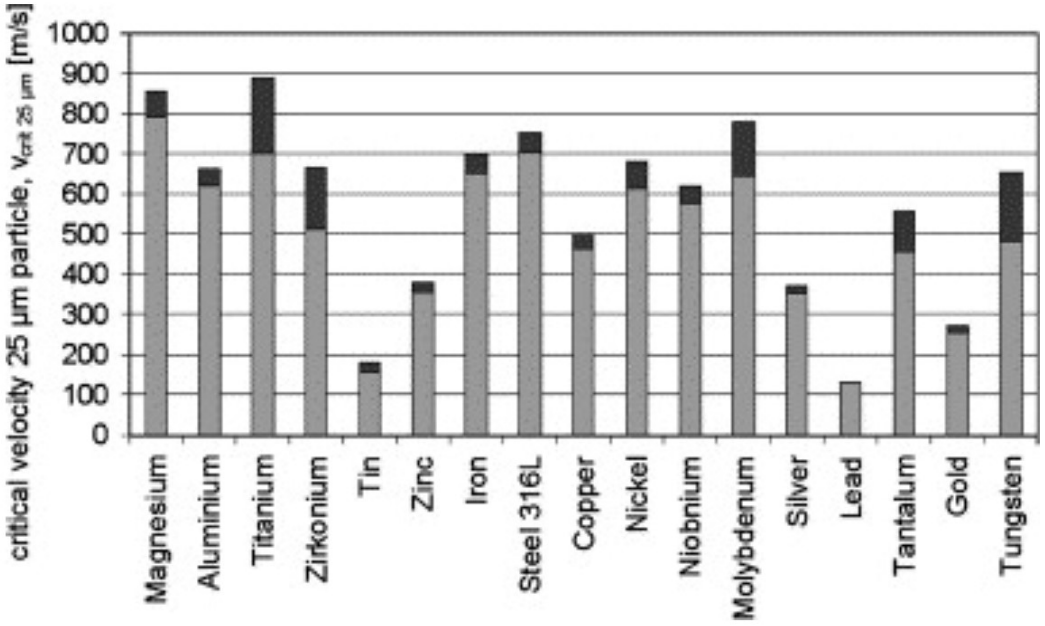


**Figure 5 Empirically determined critical velocities to illicit adhesion for several common metals using 25 µm sized particles. Dark gray region is range of uncertainty.** *[36]*

CV is best determined through experimentation and Assadi et al. outlines the process for empirically determining the CV for copper feedstock in a study that specifically investigates adhesion parameters of the CS process [20]. Particles of different sizes were accelerated using both helium and nitrogen gas heated to 320°C. Critical velocities were determined using laser doppler anemometry in conjunction with computational fluid dynamics (CFD). The CV was determined from identification of the largest, and subsequently slowest particle that successfully bonded with the substrate. This velocity value is the lowest possible value to produce adhesion, and therefore the CV. Results show two distinct critical velocities for two particle size ranges. A value of 570 m/s was obtained for 99.8% Cu particles ranging from 5 microns to 22 microns, and 670 m/s for 99.93% Cu particles below 45 microns [20]. The data

clearly demonstrates that larger particles require a greater velocity to successfully bond. Despite particles reaching this CV, adhesion may not occur for several reasons and an efficiency metric becomes useful for documenting working process parameters. Deposition Efficiency (DE) represents the fraction of the particles sprayed initially to the mass of powder that makes up the resulting bulk structure. DE can be calculated by dividing the change in weight of the feedstock by the final weight of the sprayed compact. This ratio can also be correlated to process parameters including velocity, powder feed rate, substrate area, and number of passes [15]. Figure 6 demonstrates correlation between mean particle velocity and DE with comparative results from model and experimental data [37].

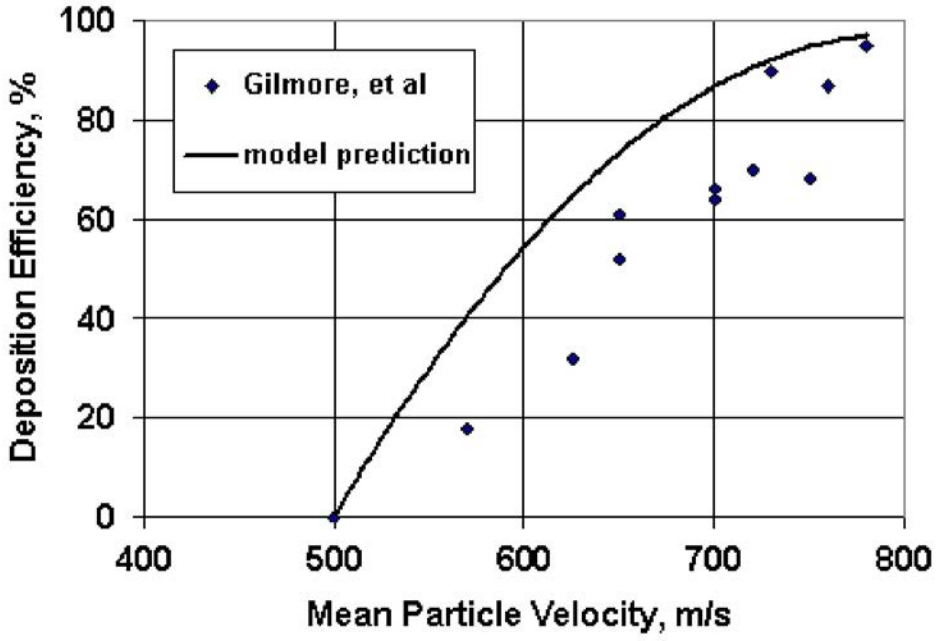


**Figure 6 Deposition efficiency as a function of mean particle velocity (Copper Feedstock) showing a comparison between model and experimental results.** *[37]*

The relationship between the material used for the substrate compared the powder affects the necessary CV as well. Figure 7 compares four substrate-feedstock combinations and their adhesion outcomes with soft feedstock paired with a soft substrate producing the best scenario for adhesion [16]. This bonding case is optimal due to particles needing sufficient plasticity for deformation as well as the substrate maintaining enough ductility to allow for penetration [16], [35].

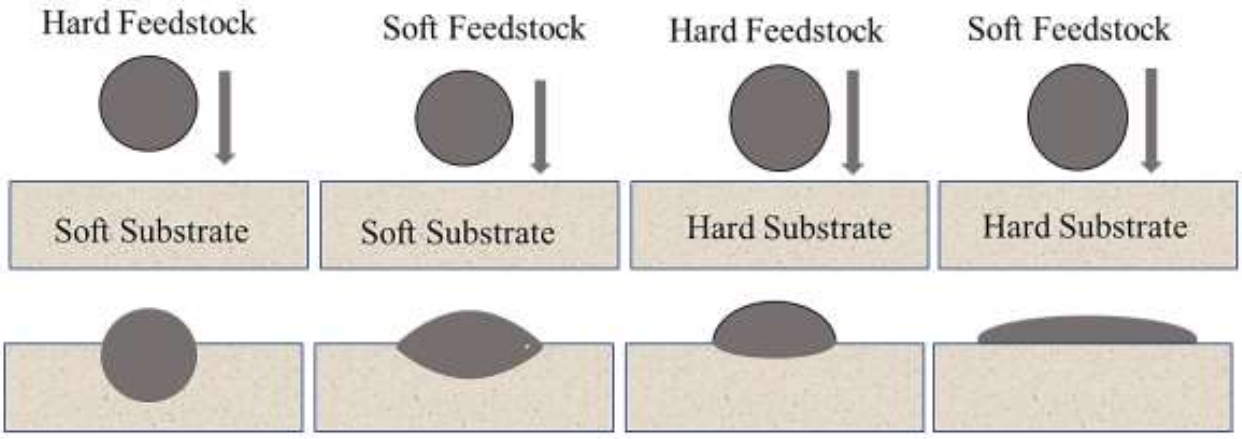


**Figure 7 Diagram comparing adhesion conditions of CS showing that hardness of feedstock in relation to the hardness of the substrate affects adhesion. Soft feedstock and a soft substrate produce the best scenario.** *[16]*

## 2.2.2 Process Gas

The process gas used for CS affects velocity which directly affects particle adhesion. Helium, nitrogen, and air are the three main process gasses used in CS with helium providing the highest DE [15]. Helium possesses the lowest molecular weight and therefore the greatest carrier velocity lending to its higher DE [15], [16]. Nitrogen is more commonly used due to cost

constraints associated with helium which limit its potential for industrial application [16]. However, ARL has developed a helium recovery system capable of 80% retention, helping to mitigate this cost barrier in industry [35]. Air, despite being the most readily available, is the least used acceleration gas due to increased oxidation risk of feedstock during heating and feedstock-gas entrainment.

Due to the cost associated with helium, there are benefits to optimizing process parameters while using nitrogen. Nitrogen is reported to be capable of similar DE when compared to helium through parameter optimization. For example, Wong et al. reports a higher DE with nitrogen was possible if a much higher inlet temperature was used [38]. However, a heating threshold exists where particles become prone to oxidation as well as nitridation [38]. Moreover, excessive inlet heating is also known to clog the nozzle when using low melting temperature metals.

### 2.2.3 Temperature

An additional process parameter that can be manipulated and optimized for CS is temperature. The temperature of both the process gas and feedstock particles prior to gas entrainment affect deposition. Increasing the temperature of the process gas significantly influences particle velocity, therefore impacting DE [32]. Empirical evidence from the literature shows that increasing gas temperature increases particle velocity [15], [16], [35], [38], [39]. An

example from Yin et al. shows that increased gas temperatures resulted in a greater acceleration of particles for both experimental and numerical simulations [39]. Particle heating in addition to increasing process gas temperature also reduced the necessary CV to illicit adhesion. Through thermomechanical softening, the feedstock material can deform more easily, promoting larger jet formation which increases the contact surface area after impact, thus improving DE overall [40], [41]. Figure 8 demonstrates an increase in coating thickness or DE, with higher pre-heat temperature.

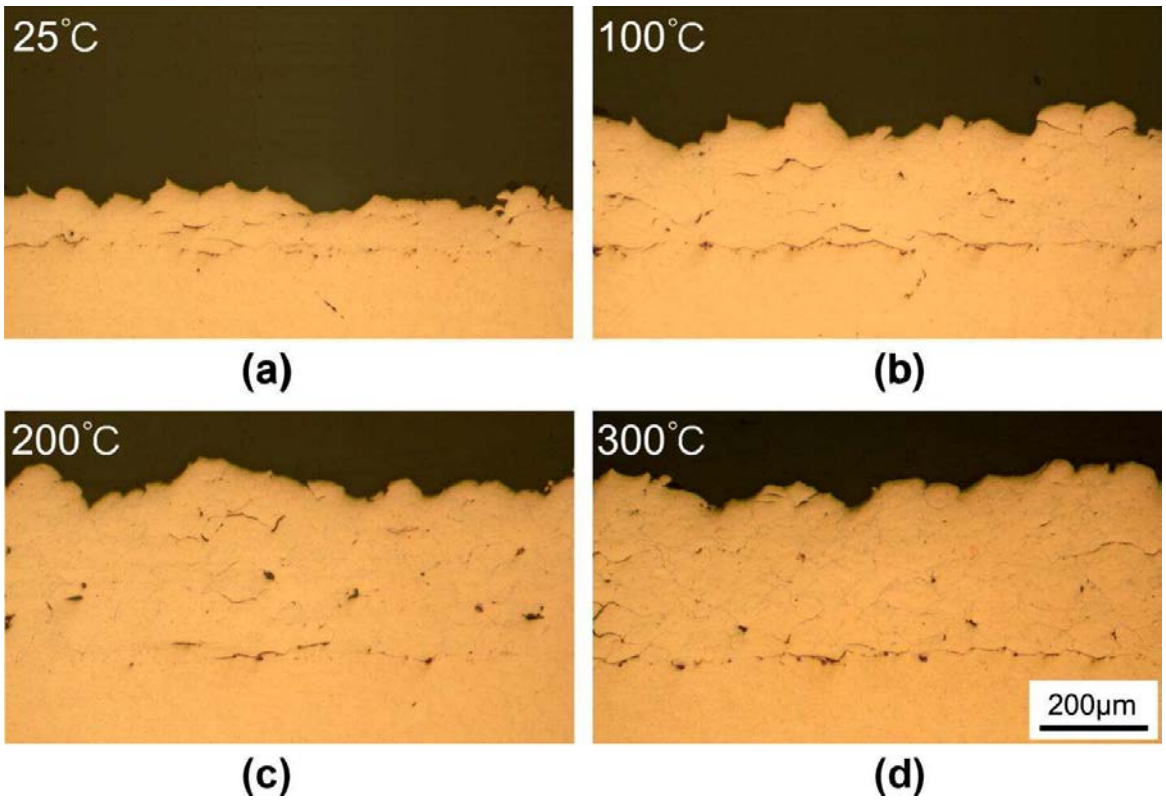


**Figure 8 Optical images of coating thickness of copper cold sprayed compacts compared to pre-heat temperature. Demonstrates that an increase in temperature increased coating thickness and deposition efficiency. (a.) 25°C. (b.) 100°C. (C.) 200°C. (d.) 300°C.** *[41]*

## 2.2.4 Process Powder

Metallic powder can be synthesized or generated through various means for the CS process. One of the more conventional methods for developing powder is through gas atomization (GA) and sieve collection [42]. The process produces particles with more round morphology and lower levels of impurities compared to other methods such milling [15]. A schematic for a GA system is shown in Figure 9 [43]

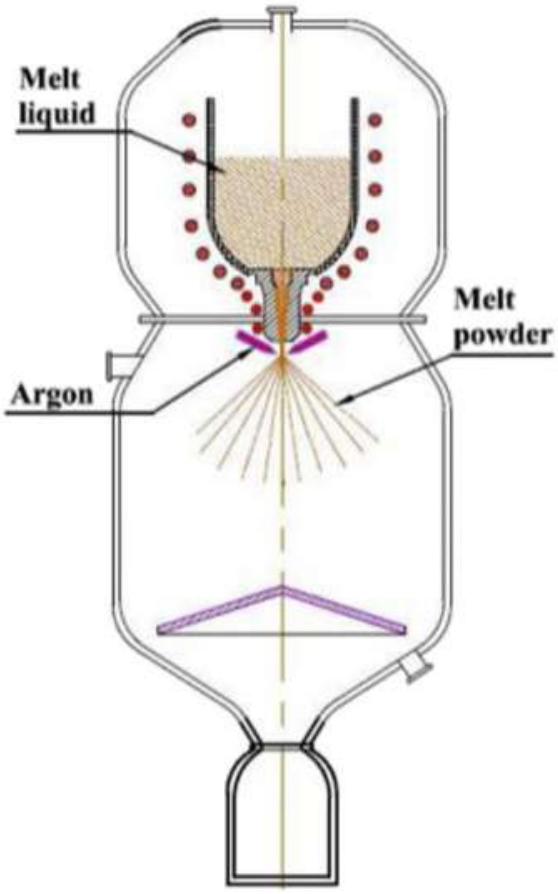


**Figure 9 Gas Atomization system for metallic powder preparation.** *[43]*

GA uses an inert gas that is injected into molten metal which separates the metal into individual droplets [15], [28]. An immediate increase in surface area allows for rapid cooling and particles fall into an atomization tower below while the sieve separates particles by size.

Particle morphology also affects DE. There are two distinct particle types that result from powder processing, spherical and aspherical shaped [28], [44]. Spherical particles assume less drag during flight and are preferred for their penetration capabilities into the substrate [15], [16], [44]. Spherical particles produce deep penetration, widespread jet formation, and homogenous adhesion, whereas aspherical particles do not penetrate sufficiently and must adhere by adapting to the surface topology of the substrate [16]. Particle size also influences deposition with smaller particles requiring a lower CV [16]. However, smaller particles are more subject to bow shockwaves. Large particles on the other hand better retain heat which is critical for plasticity and adhesion suggesting an optimal size lies somewhere in between [16], [28]. Figure 10 shows copper powder morphology produced by gas atomization for particles ranging from 15 to 38 μm in size.

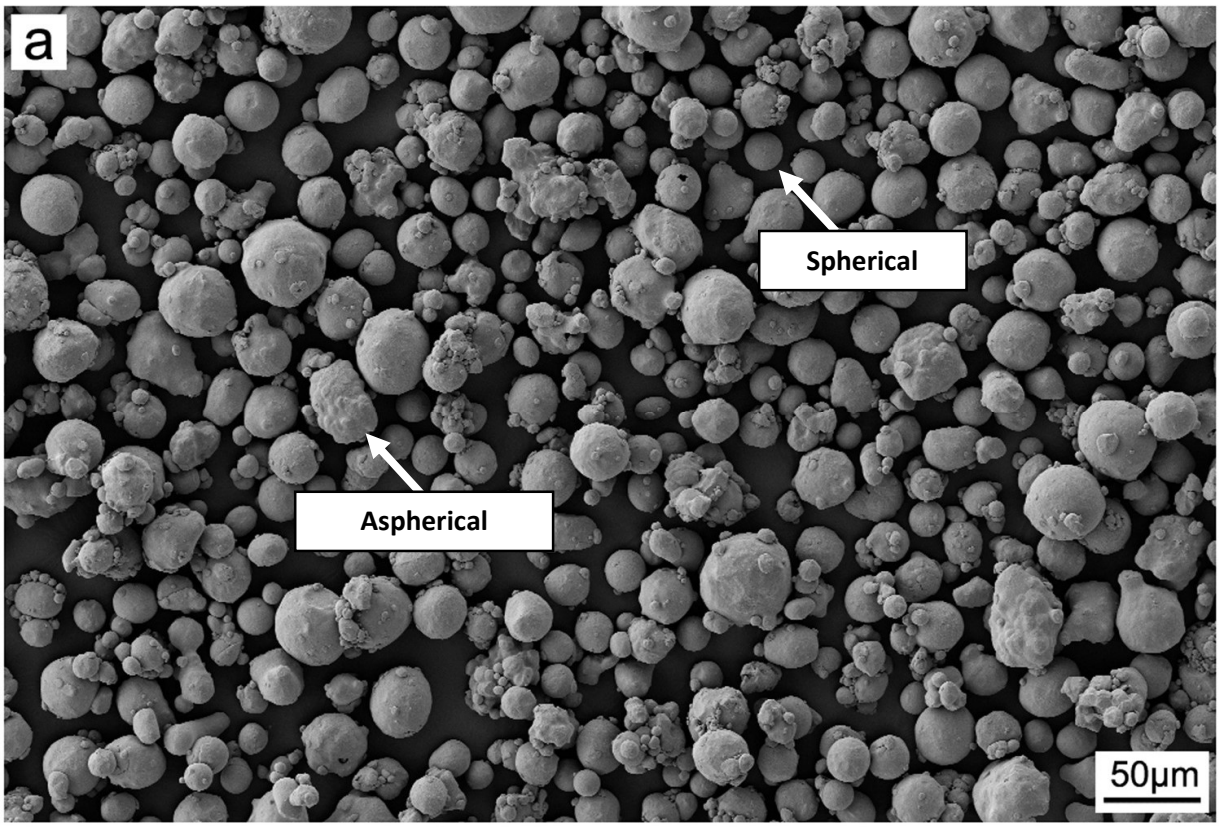


**Figure 10 Electron Microscope image showing copper feedstock morphology for 15 - 38 µm size particles produced by gas atomization. Arrows indicate spherical and aspherical shaped powder particles.** *[2]*

## 2.3 Interparticle Bonding

Investigation into the complex bonding process requires studying how singular particles interact through molecular dynamics. These studies outline individual particle bonding using computer simulations to analyze atomic and molecular movement. The system in question is given a set of parameters and particle interaction occurs over a small finite time window to allow for numerical computation [45]. Analysis of individual particle bonding for the CS process

is possible due to several factors including the geometric simplicity of spherical particles and the assumption of an adiabatic process [46]. Results can be extrapolated to provide an understanding of the particle-substrate adhesion phase as well as insight into the entire bonding process. Rahmati et al. presents a molecular dynamics study for copper particles ranging from 5μm to 45μm in diameter with an initial particle velocity of 1000 m/s [46]. The gas and substrate were heated to 300K providing thermal softening and decreased gas viscosity. Results demonstrate that three distinct phases emerge during adhesion and can be characterized by well-defined patterns of dislocations. Stage one starts within a few picoseconds of contact with the substrate where nucleation and glide dislocations initiate dislocation plasticity [46]. Following nucleation, phase two shows a characteristic dislocation forest formed in the lower half of the particle while the upper half remains uniform (Figure 11). Furthermore, work hardening begins to occur in the lower half of the particle at this stage.

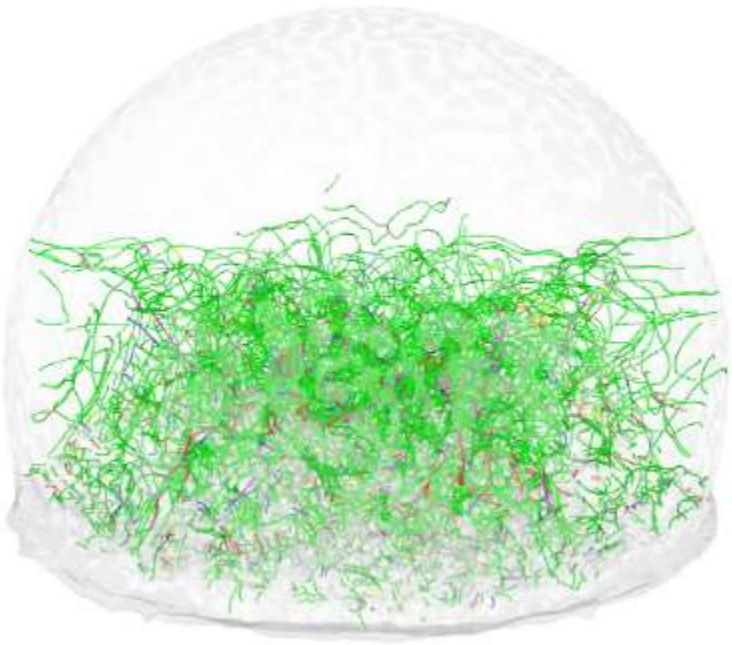

**Figure 11 Illustration of dislocation cloud forming in CS particle 10 ps after impact with uniform upper half.** *[46]*

Near the 15-picosecond mark, jetting zones form at the periphery of the particle where high forces cause severe levels of plastic deformation. Figure 12 illustrates these jetting zones which cannot be represented by a typical deformation scheme. A radial distribution function was applied to analyze these zones demonstrating a completely amorphous structure void of crystallinity. Moreover, these zones exhibit plastic flow in a quasi-liquid state and drive particle adhesion with local temperatures reaching as high as 1000K [46]. The last phase of particle adhesion is defined by a flattened particle with a total dislocation density of $10^{17} m^{-2}$ [46].

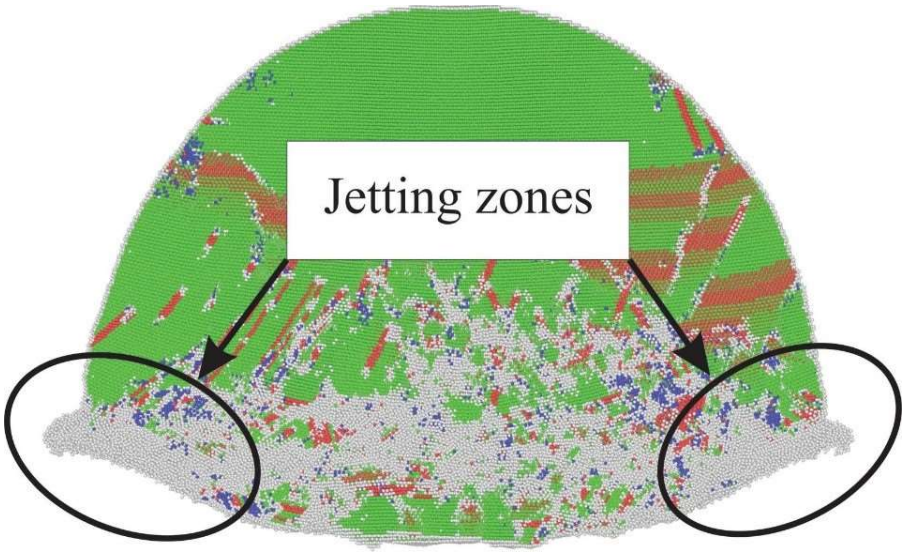


**Figure 12 Illustration of CS particle after contact with substrate showing jetting zones occurring at the perimeter of the particle-substrate interface.** *[46]*

While single particle interaction is useful for study, resultant properties of CS material do not always pair with their wrought counterparts. For example, Sundberg et al. discusses that single CS particle static nano hardness differed by 17% when comparted to a conventional CS coating – 191HVN vs 165HV – for single particle and bulk coating respectively [19]. Correlating this value to yield strength using Cahoon's relationship would yield erroneous information for a bulk structure. Although Rahmati et al. clearly outlines the stages of the bonding process for a single particle, an all-encompassing bonding theory has not yet been established for multi-particle bonding. It is however, widely accepted that Adiabatic Shear Instability (ASI) is the primary theory for CS bonding [2], [15], [16], [19], [20], [35]. According to the ASI theory, no heat is expelled during bonding except in the localized region near the particles-substrate interface and thus adiabatic. Second, initial particle impact disrupts oxidized layers enhancing surface

area contact [15]. Third, jet formation and induced plastic flow from thermal softening and high strain also increase interfacial contact in the peripheral region of the particle and promotes metallurgical bonding. Lastly, the initial impact forces and high pressure induced by supersonic particle collision also influences cohesion as some level of penetration is required. [47]. Overall, the bonding mechanism depends on several factors such as shear instability, jet formation, and impact velocity, and the literature indicates there is no conclusive theory to explain the bonding mechanism completely [16], [48].

## 2.4 Cold Rolling and The Relationship to Cold Spray

Cold rolling (CR) is a mechanical deformation process used to strengthen and manipulate properties of raw metal by way of strain hardening through repeated flattening using a series of large cylindrical rollers [49]. It can be used to produce materials with accurate dimensional tolerances and quality surface finish. A schematic of a CR process is shown in Figure 13 [50]. Figure 13 also shows a diagram of the structure produced by CR with microstructural representations for the rolling and transverse directions. Along the transverse direction elongated and lamellar structures can be seen which are common in materials subjected to monotonic deformation like rolling. The normal direction contacts the rollers, and the rolling direction follows the motion of the work piece [51].

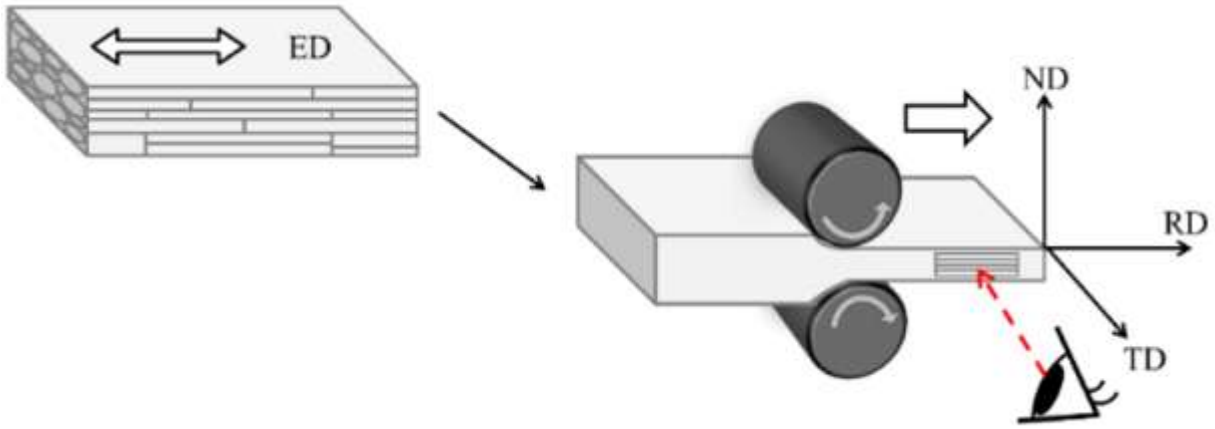


**Figure 13 Schematic of a Cold Rolling mill.** *[50]*

Properties from cold work are dependent on the percentage of deformation induced through strain hardening and can be represented by a ratio of initial and final cross-sectional area. CR specifically, uses a percent reduction in thickness to define percent cold work [49]. Percent cold work is intrinsically linked to yield and tensile strength, both increasing as deformation increases. However, ductility reduces in the process eventually resulting in brittle behavior providing an inherent material based cold work limit [49]. The strain hardening exponent "*n*" governs a material's response to cold work and is logarithmically proportional to the true stress and true strain. A larger *n* value indicates a greater degree of strain hardening is possible. During tensile testing, necking will occur when the *n* value is approximately equal to the true strain [49]. Table 1 shows a comparison of typical metals and their respective strain hardening exponent [49]. Copper notably possesses the highest capability of strain hardening offering an excellent representation for the extreme levels of cold work induced by high

reduction rolling and the CS process. High reduction rolling produces a similar level of microhardness as CS and the greater the percentage reduction the higher the microhardness. CS specimens can exhibit microhardness equivalent to 90% reduction rolling depending on process parameters and material. Literature and empirical evidence surrounding CR are useful comparative tools for the CS process as they both produce similar levels of deformation. Moreover, CR is a well characterized system and provides the foundational understanding for the Hall Petch relationship.

**Table 1 Comparison of typical metals and their respective strain hardening exponent.** *[49]*

| Metal | Crystal Structure | *n* |
|---|---|---|
| Titanium | HCP | 0.05 |
| Annealed alloy steel | BCC | 0.15 |
| Quenched and tempered medium-carbon steel | BCC | 0.10 |
| Molybdenum | BCC | 0.13 |
| Copper | FCC | 0.54 |
| Cu-30% Zn | FCC | 0.50 |
| Austenitic stainless steel | FCC | 0.52 |

## 2.5 Microstructure of Cold Spray

The microstructure produced by CS contains both microscopic and nanoscopic grains resulting from SPD and flow-like behavior in jetting zones near interparticle boundaries [22]. These boundary regions show SPD and high dislocation density due to large impact forces and thermal softening during jetting [2]. Moreover, work hardening, and grain refinement also occur

in these regions leading to higher levels of microhardness [2]. The overall microstructure features a heterogenous grain distribution characterized by these distinct particle-particle impingement zones and large grain size regimes stemming from center particle flattening called "pancaking" [4], [35]. A third zone emerges as a combination of the two which exhibits a size above the ultra-fine grain (UFG) threshold but below any meaningful representation of a large intraparticle grain. Thus, showing the difficulty associated with characterizing the microstructure.

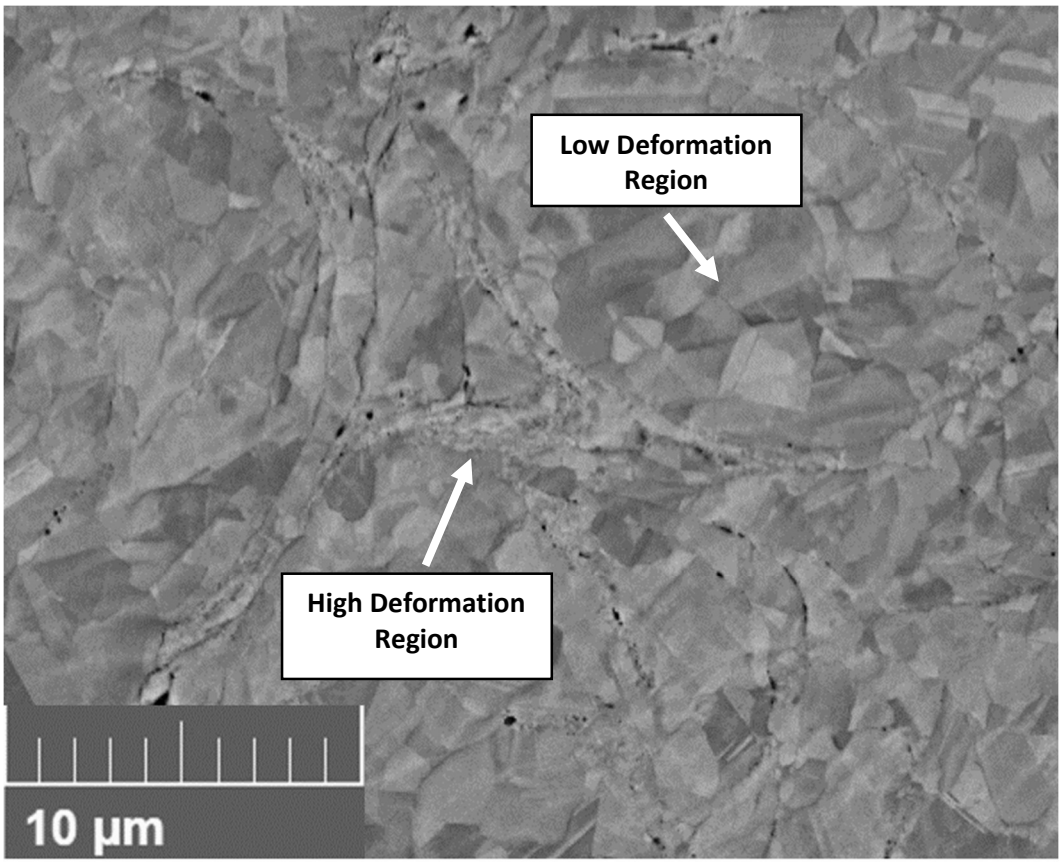


**Figure 14 Characteristic deformation regimes resulting from cold sprayed copper. Arrows indicate high deformation and low deformation regions (BSE).**

Figure 14 shows a copper CS specimen microstructure. Highlighted are the High Deformation Regions (HDR) and Low Deformation Regions (LDR) *[35]*. It can be clearly seen that the most deformation occurs near the edges of the particles where strong impact forces create jetting, and limited deformation occurs in the regions further from these jetting zones. For microstructural characterization, CS imaging is typically separated into two orientations, transverse, and spray direction. The transverse orientation represents planes whose viewing direction is orthogonal to the spray direction, and the spray orientation follows the line of sight of the impacting particles. When observed in the transverse direction the microstructure tends to exhibit elongated and flatted grains (Figure 15b & 15c), while the spray direction lends itself to equiaxed grains (Figure 15a). However, Yin et al. reports annealing treatment erodes the stark contrast between these independent configurations as illustrated by Figure 15 d-e *[2]*

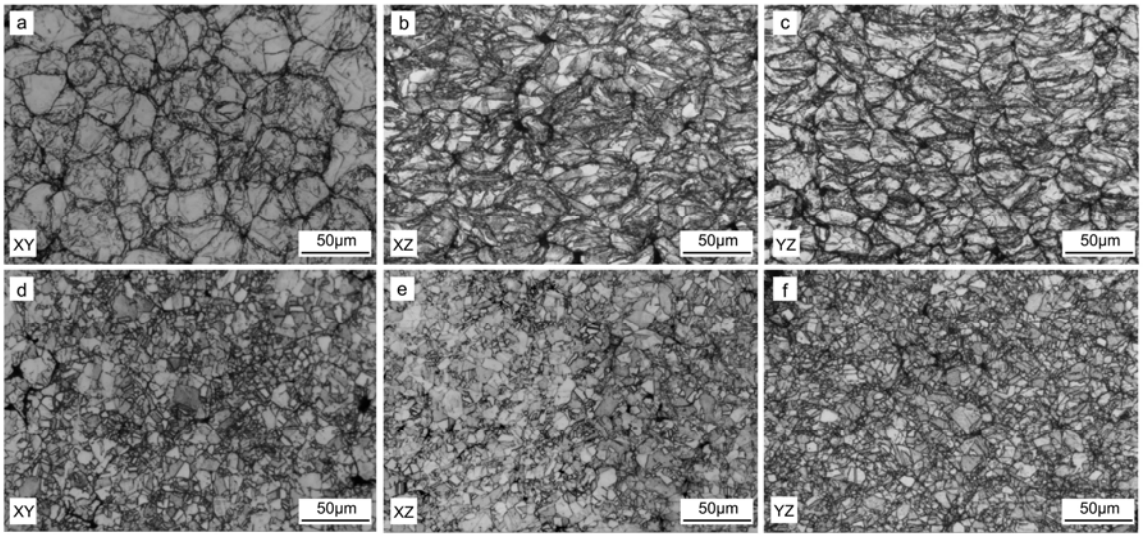


**Figure 15 Micrographs of Copper CS deposits following bidirectional spray patters. Top row (a,b,c), As-Sprayed CS deposits a: Spray Direction, b&c Transverse Direction. Bottom Row (d,e,f), Annealed CS Deposits d: Spray direction, e&f: Transverse Direction.** *[2]*

### 2.5.1 Hall-Petch Relationship to Cold Spray

The nanoscale microstructure produced by the CS process also brings into question the Hall-Petch relationship. It is known that nanostructured materials in general have higher yield strengths compared to coarse grained metals, and higher strength often results in consequentially reduced ductility [52]. The Hall-Petch relationship shows that as grain size becomes smaller in polycrystalline metals the yield strength increases by way of dislocation inhibition [53]. The Hall Petch relationship obeys the following equation (2.1), where $\sigma_y$ is the yield strength, *d* is the average grain diameter, and $\sigma_0$ and K are material constants.

$$\sigma_y = \sigma_y + Kd^{-1/2} \tag{2.1}$$

Strength increases in copper of over 400% have been achieved when reducing grain size to 20 nm [52]. However, there is a threshold in which the effect no longer follows the trend. At grain sizes below 20 nm metals can exhibit an inverse Hall-Petch response, softening and losing strength. This softening occurs due to deformation modes reducing to only grain boundary rotation, sliding or creep. Mode reduction is caused by grains no longer responding to internal deformation at such reduced size. CS microstructure, often possessing grains both well below and above this threshold, offers an interesting case for study. Exploring beneficial properties from both ends of the spectrum would increase the application options for CS products and research into manipulation of parameters such that ductility and strength may be optimized near this Hall-Petch threshold would prove valuable [52].

## 2.6 Mechanical Property Evaluation

The resultant properties of CS materials stem from the adhesion mechanism, and highly work hardened microstructure. Macroscopic properties such as yield strength determine the viability of CS deposits in coatings, repair, and bulk part production [5], [15]. For bulk structures produced by CS, as sprayed components typically exhibit lower yield strength when compared to their wrought counterpart with consequentially higher hardness [54], [55]. Pores, and inconsistent bonding create defects leading to undesirable as-sprayed properties overall. Annealing has been shown to restore ductility, reduce hardness and relieve residual stresses [15], [54]. In some cases, annealing can drive precipitation of strengthening phases increasing the ultimate tensile strength (UTS) of the material [15]. Microhardness testing is a valuable characterization technique that can provide bulk property information where direct measurement is not possible. Microhardness also allows for relatively noninvasive mechanical property evaluation and is useful for verifying production parts. UTS can be determined through Cahoon's equation (2.2) which relates microhardness (H) and strain hardening coefficient (n), to tensile strength (TS), [56].

$$TS = \left(\frac{H}{2.9}\right)\left(\frac{n}{0.217}\right)^{n} \tag{2.2}$$

A Vickers Microhardness test uses a pyramid shaped diamond indenter a to deform the surface of a material [57]. The indenter is typically held for a period of 10 to 15 seconds with a standard force value ranging from 1-120kgf. The length of the diagonals depends on the

indenting force and the strain hardening exponent [57]. An average microhardness is determined by sampling several areas throughout a test coupon and measuring the indent size with a microscope [58]. CS deposits present challenges to the underlying assumption of microhardness due to wide inhomogeneity between grain size on a scale smaller than the size of a typical indent. The visible inhomogeneity of CS microstructure correlates to the distribution of microhardness levels often reported [2], [35]. Regions near the particle edge experience SPD and therefore on average have higher microhardness due to increased dislocation density, strain hardening, and decreased grain size [2]. Conversely, lower deformation zones with larger grains typically result in lower hardness.

Differentiating these different deformation regimes is of interest as sampling is often limited by the size of the indenter and an aggregate of more than one region is captured [59]. Figure 16 illustrates this complication showing several nano-scaled grains captured in one Vickers indentation mark on a CS 6061 Aluminum sample.

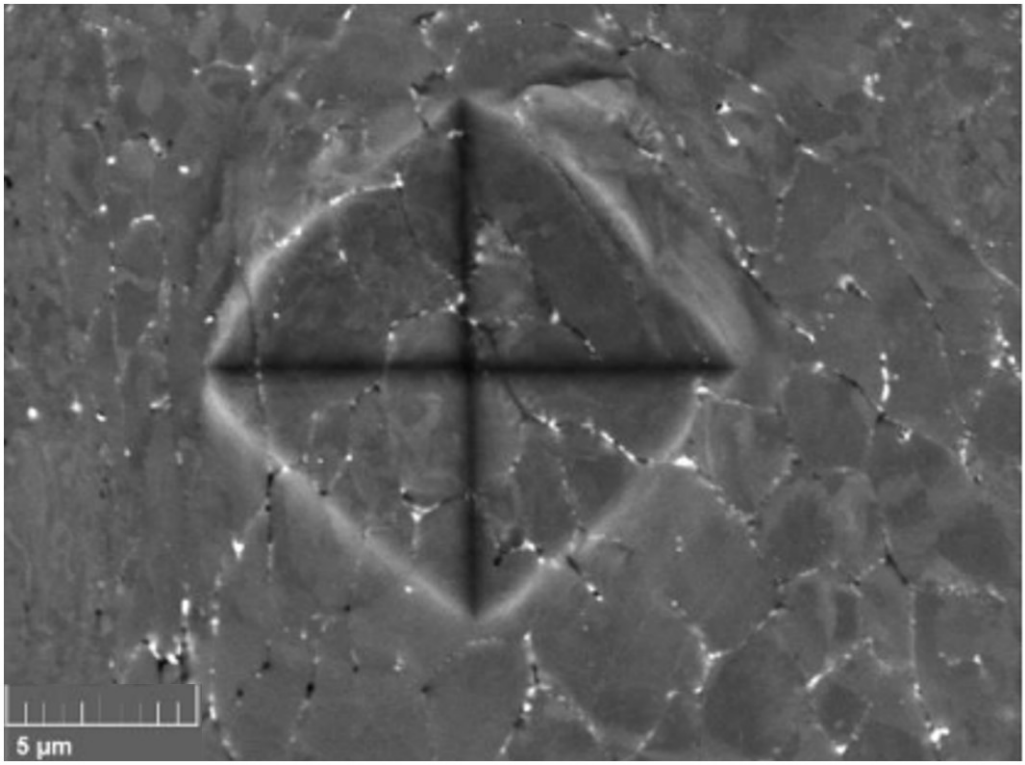


**Figure 16 Micrograph of Vickers microhardness indent on CS Aluminum material showing multiple nano-scaled grains captured within indent region.**

## 2.7 Microscopy and Microstructural Characterization

A possible method of investigating these aggregate regions in CS material is using EBSD. EBSD is a technique used to gather detailed information about grain size and orientation in a material. First, a sample is mounted at a 70° tilt from the microscope stage and the EBSD detector is inserted close to the specimen. The tilt improves the signal to noise ratio resulting better pattern contrast and faster scan time. A material is then selected from a data base with stored pattern information. The beam scans point by point across the surface of the sample and

Kikuchi band diffraction patterns are indexed from coherently scattered electrons [60]. The intensity and width of the Kikuchi bands are related to the interplanar atomic spacing, and the bands correlate to families of crystallographic planes. The diffracted electrons containing valid information are limited to only few nanometers deep lending to the high-quality surface finish required for EBSD. The resolution of EBSD is dictated by the step size of the point scanning and various sizes can be chosen, with smaller size resulting in more detailed images but a longer scan time. EBSD pole figure maps can be created from these stored diffraction patterns and a legend shows the orientation of each crystal captured on the image. EBSD scans could be conducted prior to indentation and used to more accurately correlate grain refinement and orientation to microhardness. An EBSD schematic is shown in Figure 17 with major components labeled.

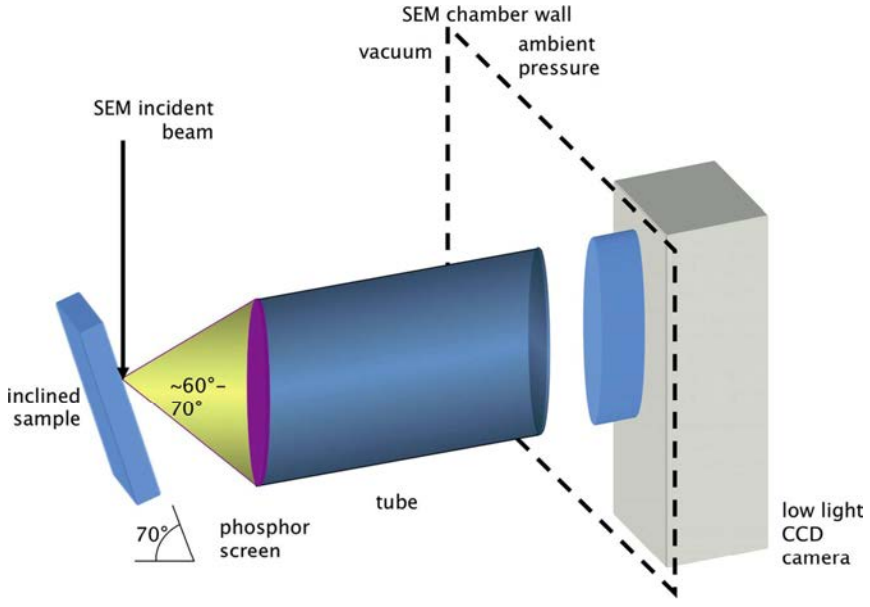


**Figure 17 Electron Back Scattered Diffraction schematic with major components labeled.** *[60]*

## 2.8 Scanning Probe Microscopy

An additional method for investigating these aggregate regimes is SPM Mapping. An SPM leverages Van der Waals interactions between a sharp probe (<10 nm) located on the end of a cantilever and the surface of a sample. The cantilever deflects during operation and reflects a laser into a series of photodiodes [61]. These diodes measure the striking position of the laser and calculate the force on the probe tip. Information about the samples surface is generated using an internal feedback loop. A schematic for an SPM is shown in Figure 18 with the important features of the instrument labeled. There are several different modes a SPM can use to determine various information about a specimen. SPM "Tapping" is a dynamic mode where the probe is excited near a fixed resonant frequency and yields detailed sample topography [61]. The amplitude in which the tip oscillates provides feedback to the system which generates the image. The main advantage for tapping is that it avoids damaging the sample surface and outputs high resolution images [62]. A second feature of the instrument is a "Contact Mode" where the probe contacts the surface of the sample, generates an image and an additional 3D nano-mechanical analysis can be conducted following image collection. Physical properties can be measured by generating a force curve at various points on the sample which produces a map of the surface. The map illustrates regions of the sample that are harder or softer with respect to one another denoted by the level of shading in each pixel. Figure 19 is an example 3D nano map taken on a Shimadzu SPM 9700HT. Mapping the region prior to indentation may provide insight into these mixed deformation areas [63].

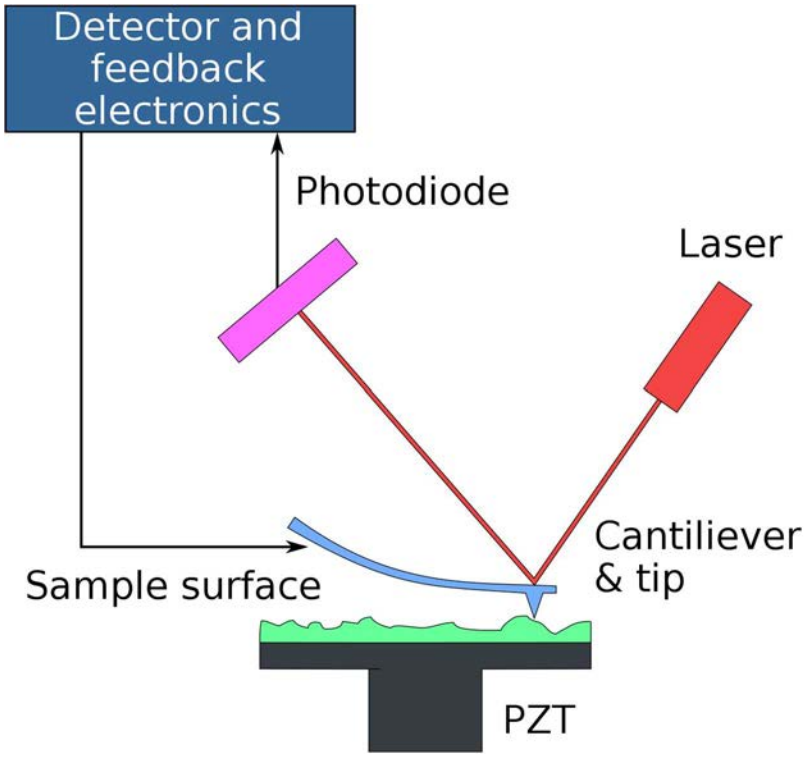


**Figure 18 Atomic Force Microscope schematic with major components labeled.** *[62]*

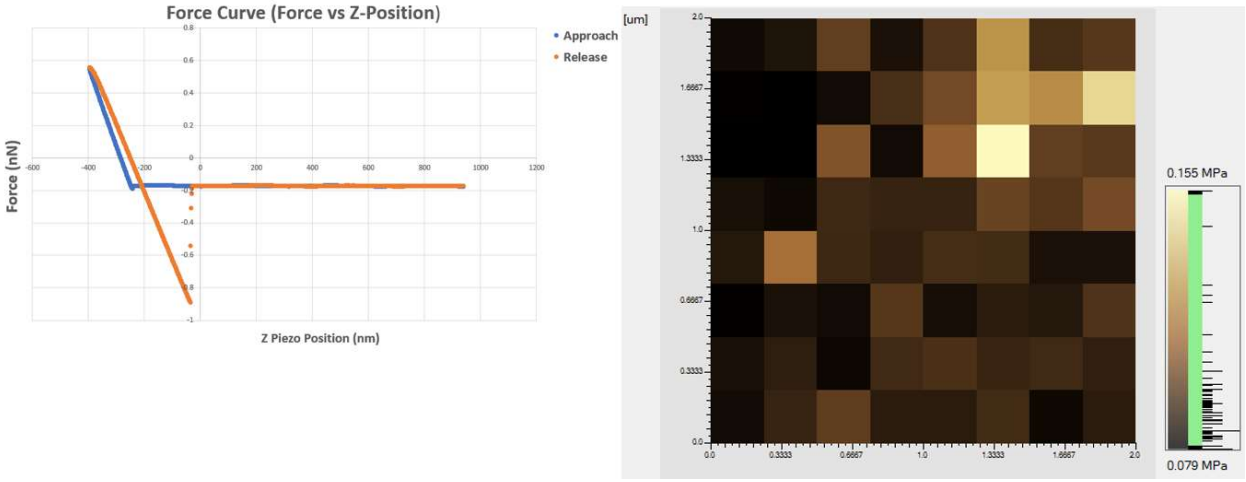


**Figure 19 Force curve and nano 3D map of copper surface taken on Shimadzu 9700HT SPM.**

# Chapter 3: Experimental Methods

## 3.0 Methodology and Experimental Process

The goal for the experiment was to characterize and indent the microstructure of the copper material using four separate imaging methods that could each be interpreted separately and then correlated. The overall experimentation process is illustrated in the flow diagram shown in Figure 20. Each section of the diagram is coded with a specific color that corresponds to an additional diagram depicting a subsequent process. The effort was divided into two main categories, imaging, and property assessment.

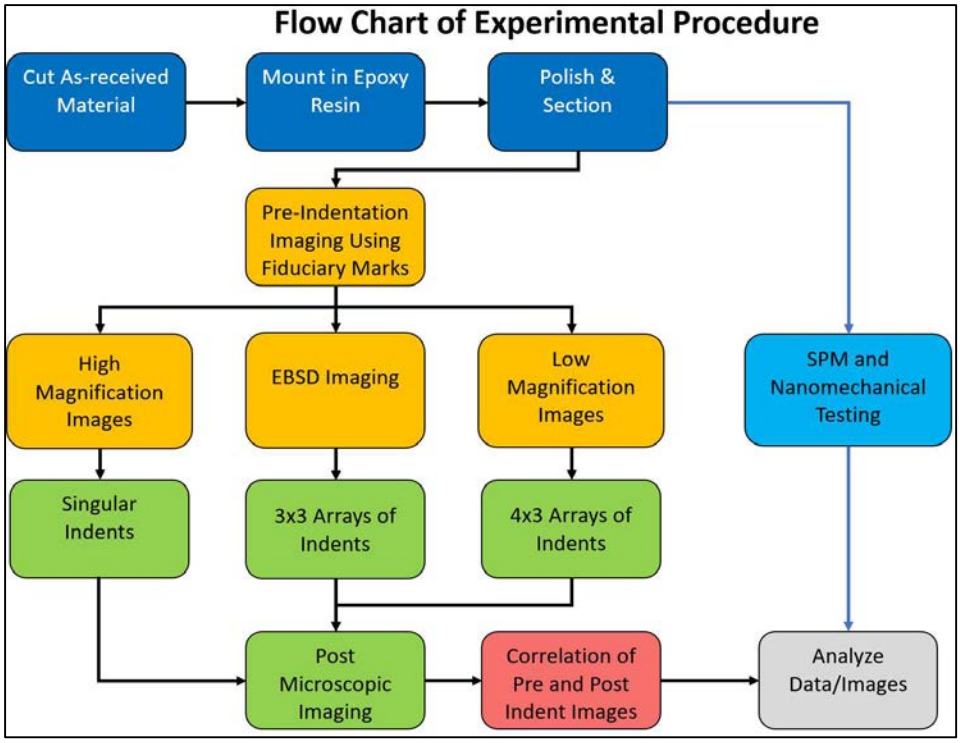


**Figure 20 Flow chart of experimental process. Each section is color coded to indicate a separate procedure with a subsequent methodological flow chart.**

The first data set began with collecting SEM images at high magnification in BSE/SE modes. Data set two reduced magnification to allow for more indents in a single image but used EBSD scanning for better analysis. Data set three used BSE and SE imaging as well, but at further reduced magnification to create a larger data set. The last method used was SPM imaging to gather topographical information and nanomechanical maps of the sample surface. The SPM procedure, which is colored in light blue on the flow diagram in Figure 19 was conducted separately from the image-indent process. This procedure can be referenced in section 3.5. Figure 21 show the process of indent and image collection.

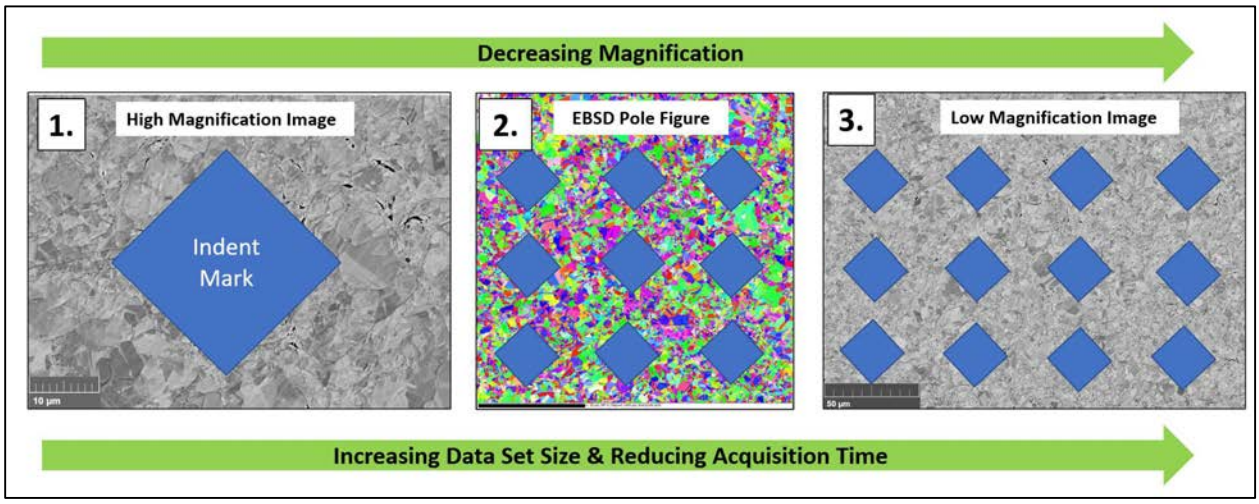


**Figure 21 Illustrates the process of image and hardness data acquisition. (1.) Individual indents using high magnification pre-indent images for analysis. (2.) 9 indents using pre-indent EBSD inverse pole figures. (3.) 12 indents using low magnification pre-indent images.**

The purpose for the order of the image collection process was to start with the most time consuming, but accurate characterization method, then trade image fidelity for reduced acquisition time and data set size. The first data set started with 10 indents characterized at high magnification for each sample. Data set two then characterized a 3x3 array of microhardness indents using EBSD. The third data set used a larger 4x3 array totaling 12 indents, but with lower magnification SE and BSE micrographs. The information gained from the high magnification images was used to extract information for each subsequent process. This process allowed for both accurate microstructural characterization at each level of magnification, as well as enough data to be collected to draw any statistical significance. Furthermore, this method was developed to consider acquisition efficiency, since characterizing each indent with high magnification and EBSD would certainly be preferable, but the time necessary to do so would have been unreasonable. Table 2 lists each sample type, the number of indents, its corresponding imaging technique, and total indents per sample.

**Table 2 Image and Indent collection table.**

| Sample Type | High Mag Images | EBSD Images | Low Mag Images | Total |
|---|---|---|---|---|
| Cold Spray-Spray | 10 Indents | 4x3 Array | 3x3 Array | 31 |
| Cold Spray-Transverse | 10 Indents | 4x3 Array | 3x3 Array | 31 |
| Pressed Powder | 10 Indents | N/A | N/A | 10 |

### 3.0.1 Materials

The materials used for this study were manufactured by Penn State Applied Research Laboratory and provided to the University of North Florida. There were two sample categories for used for comparison; a CS compact generated for the experimental group, and a pressed powder specimen created for the control group. Both specimens were made using the same spherical copper powder which averaged 13.2 μm in diameter. The purpose for these groups was to compare the inhomogeneous and highly work hardened CS microstructure to an annealed material with homogeneous microstructure and uniform mechanical properties. The pressed powder material was generated by hot isostatic press and a 52x52x13 mm plate was created. The CS specimens were created using Helium as the process gas at temperature of 90°C and a pressure of 2.1 MPa. Additionally, a powder feed rate of 8 g/min and a velocity of 731 m/s was used, creating CS compacts measuring 25 mm thick. Figure 22 (a.) shows both the spray and pressed powder sample in the as-received condition with scale bars for size reference.

## 3.1 Metallographic Specimen Preparation

The steps of the sample preparation process are shown in the flow chart in Figure 22.

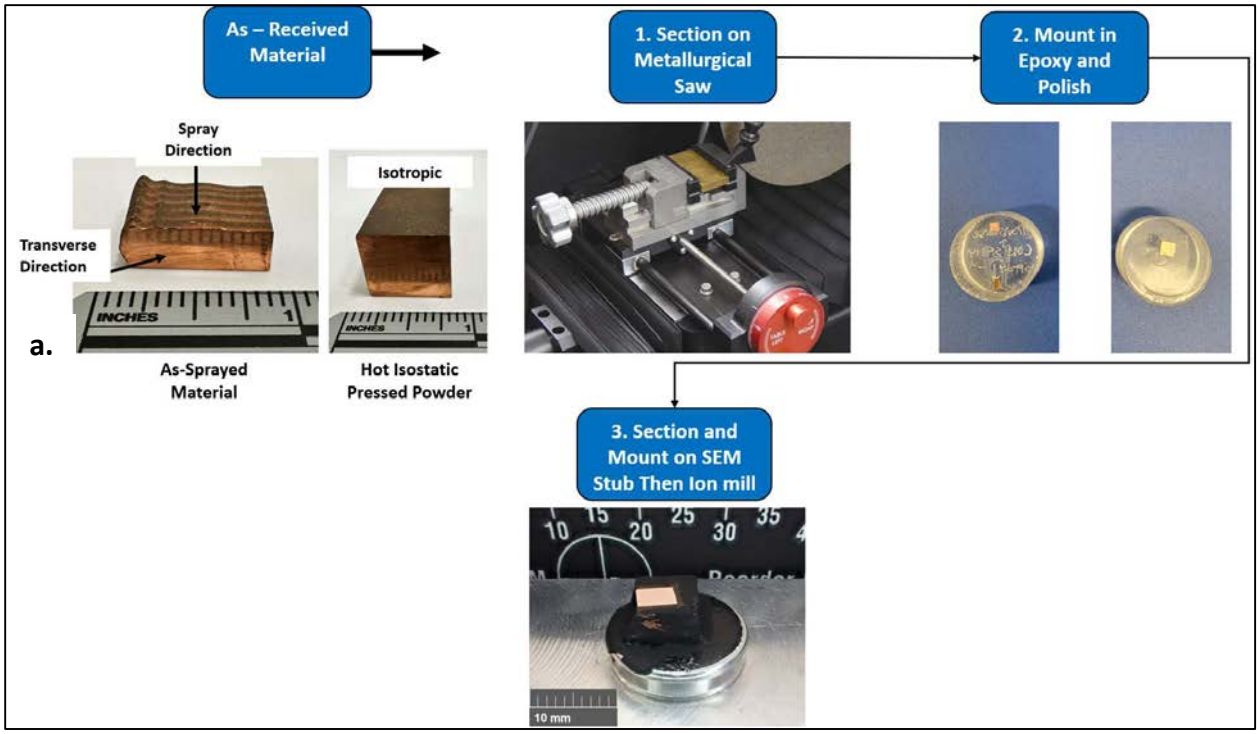


**Figure 22 Flow chart showing (a.) as-received material, and (1-3) Metallographic preparation process.**

Each sample was sectioned and mounted in a two-part thermoplastic epoxy resin and cured overnight in a vacuum chamber. Mechanical polishing was performed using an Allied High-Tech MetPrep III automatic polisher and silicon carbide grinding paper. Table 3 lists the detailed steps including force, time, and grit used during the grinding procedure. Following mechanical polishing, each specimen was cut down to fit on 12.7mm SEM stubs necessary for ion milling and SPM analysis. A Leica Ion mill was used as the final polishing step. Copper's

ductility required the use of ion milling to ensure enough damage from mechanical polishing was removed to achieve a surface finish capable of EBSD and SPM data collection. Each sample was milled for 1.5 hours at 7Kv, 2.2A, a 3-degree tilt, and a 360° rotation. An example of a final polished and mounted specimen is shown in Figure 23.

**Table 3 Mechanical polishing procedure for copper specimens used in the experiment.**

| Step (Grit Size) | Lubricant | Time / Force (N) | Polishing Solution |
|---|---|---|---|
| 400 Grit | Water | 2 min/ 4 | None |
| 600 Grit | Water | 2 min/ 4 | None |
| 800 Grit | Water | 2 min/ 4 | None |
| 1200 Grit | Water | 2 min/ 4 | None |
| 3 µm | Allied Red Lube | 4 min/ 8 | Diamond Suspension |
| 1 µm | Allied Red Lube | 4 min/ 4 | Diamond Suspension |

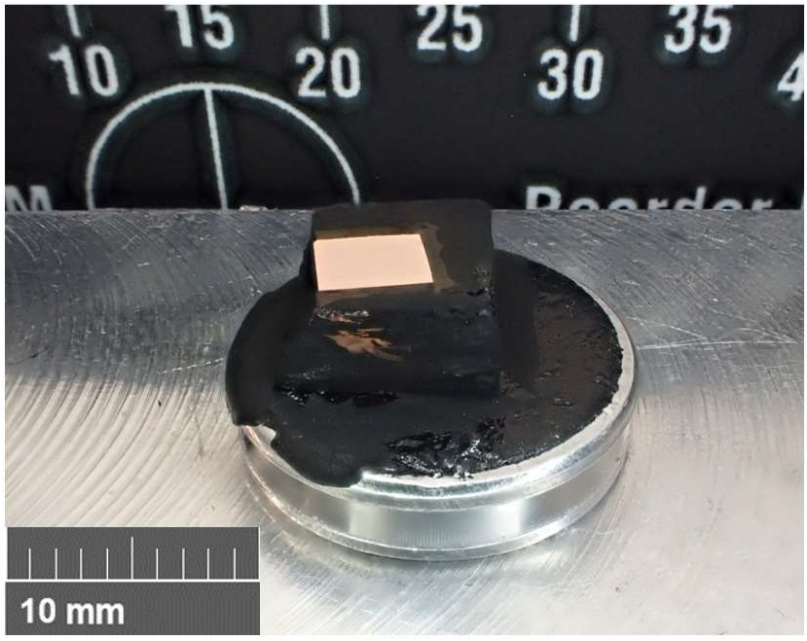


**Figure 23 Example of specimen on 12.7 mm SEM stub post ion mill – (Cold spray transverse direction sample shown).**

## 3.2 Scanning Electron Microscopy and Electron Back Scattered Diffraction Image Collection

Micrographs and EBSD were collected to first characterize the copper microstructure. A Tescan MIRA 3 field emission SEM and Tescan Amber SEM, each equipped with an Oxford EBSD detector were used for collection. A SEM uses a focused beam of electrons scanned over the surface of a material and a computer analyzes the signal produced by these interactions to generate an image. An SEM can be outfitted with several different detectors. Since electrons interact with samples at various depths and energy levels, characteristic scattering can be filtered to produce specific images. A Secondary Electron (SE) detector or "Everhart Thornley" detector is an imaging mode for SEMs and leverages surface interactions with the sample. The SE mode produces detailed topographical images of a material surface. A Backscattered Electron (BSE) detector makes use of high-elastic scattering where electrons return directly towards the incident beam. BSE images contain information based on relative planar density. For each sample, a microstructural image was collected in both SE mode and BSE mode to take advantage of the benefits from both detectors. Additionally, a EBSD scan was performed for each sample to analyze grain size and grain distribution using band contrast images and inverse pole figures.

## 3.3 Pre-Indented Image Collection

The flow chart depicting the image collection process for all indentation micrographs is shown in Figure 24. This process was followed for all three image types including high magnification, EBSD, and low magnification micrographs. The measurement tool in the Tescan software was used to create a select area image for indentation. A measurement from a fiducial mark was taken, and the center of the region was imaged. The distances from the measurement tool were used to pinpoint the region that was imaged on the SEM, allowing for indents to be accurately placed with the Vickers microhardness tester.

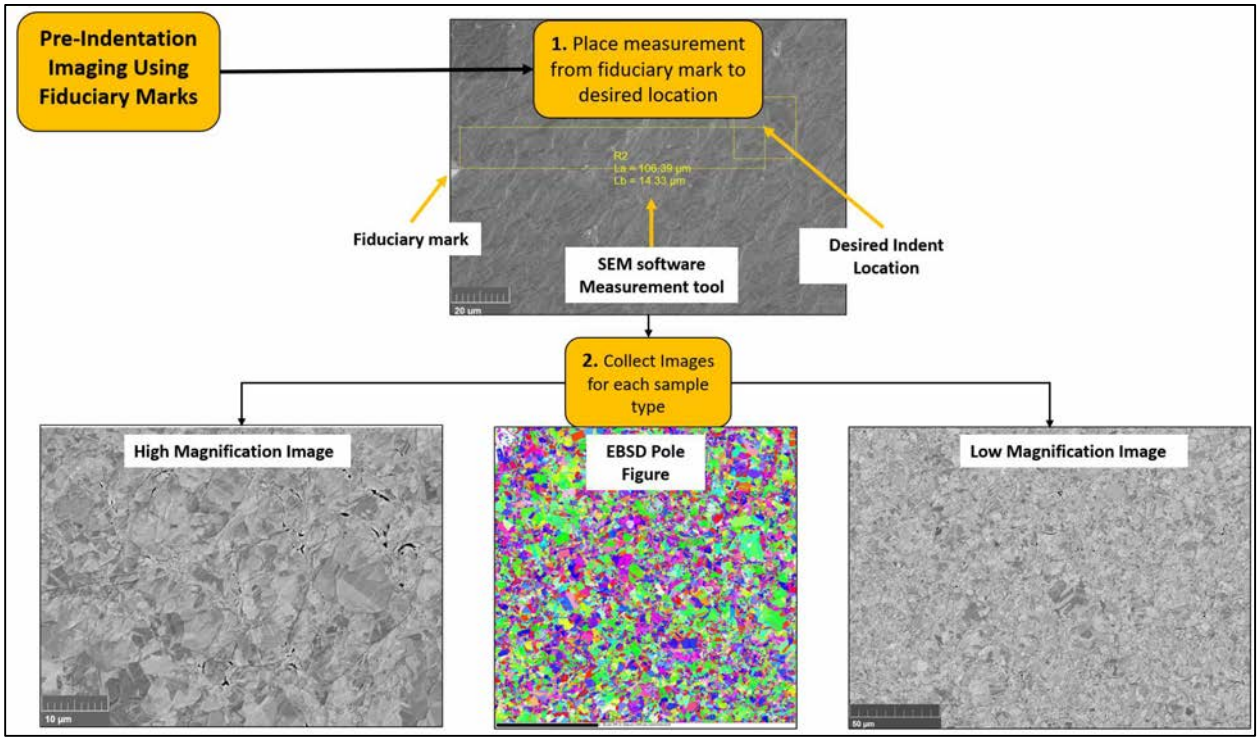


**Figure 24 Pre-indentation micrograph collection process.**

### 3.3.1 High Magnification Individual Pre-Indent Imaging

Following the diagram outlined in Figure 24, 10 images of the pressed powder, CS spray direction, and CS transverse direction samples were collected in both SE and BSE mode. A sufficient magnification was needed to properly analyze grain refinement, but low enough to allow for enough room for error when aligning the sample on the microhardness indenter with its low magnification 40x optical lens. After several test images a FOV of 60 µm was chosen. Figure 25 shows a CS spray direction micrograph taken with a 60 µm FOV in BSE mode.

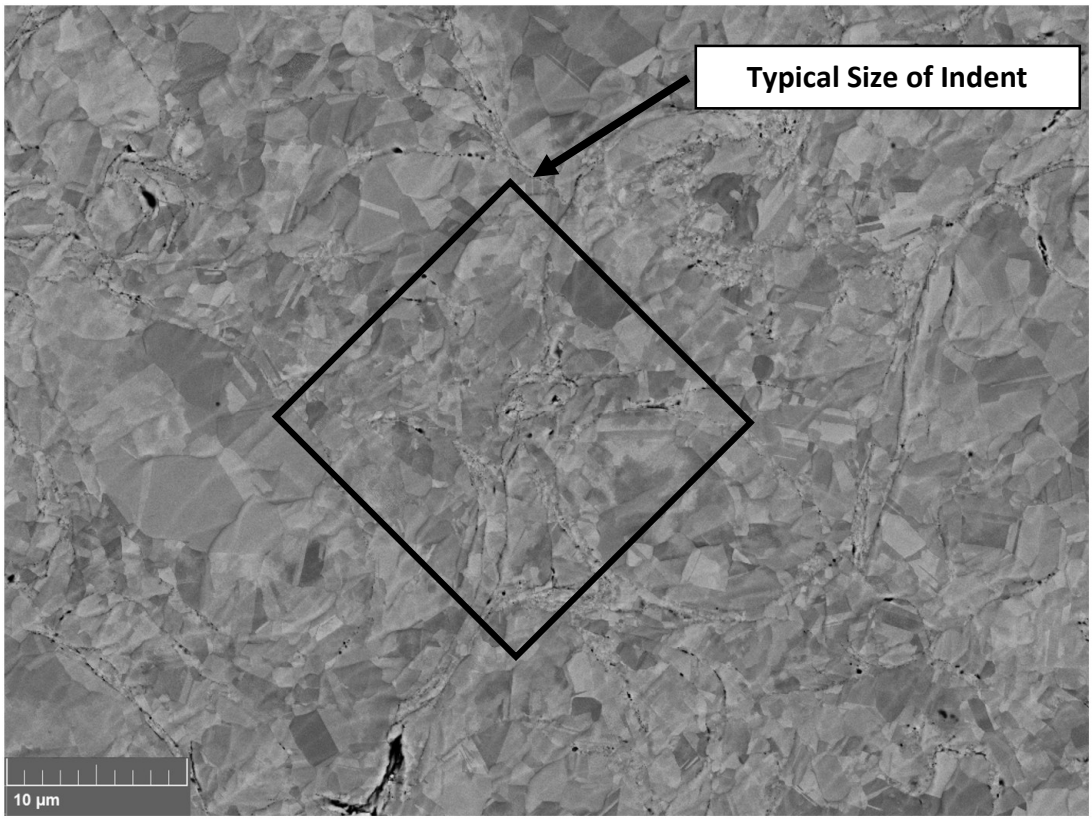


**Figure 25 High resolution pre-indentation image taken in BSE. CS spray direction shown. Arrow indicates the typical size of a single indent - 22x22µm.**

## 3.3.2 Electron Back Scattered Diffraction Pre-Indent Imaging

A pre-indent EBSD scan was performed for each CS specimen with a 175 µm FOV. This size was used to capture an array of nine indentation marks but leave room for error during indentation alignment. The same method from Figure 24 was employed to create a select area for microhardness tests. An example of a pre-indented EBSD pole figure is shown in Figure 26 with an arrow indicating the size of a typical indent mark (22x22 µm).

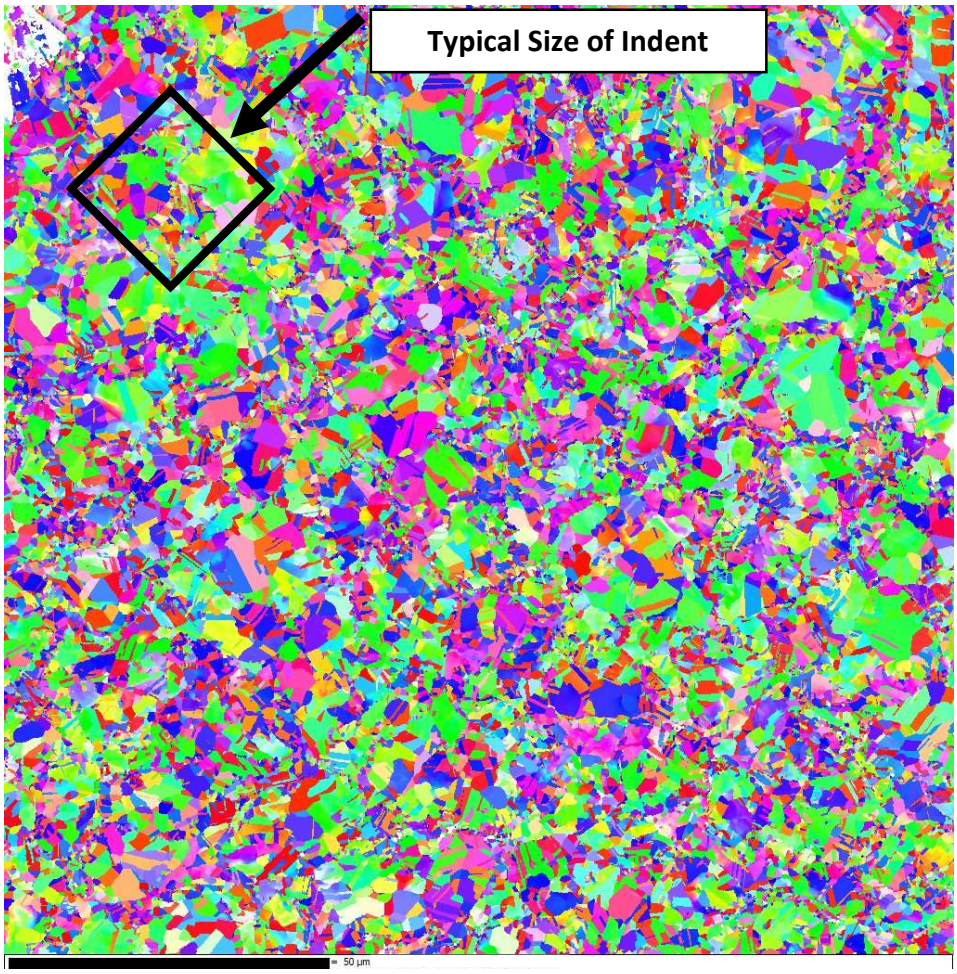


**Figure 26 Example showing pre-indented EBSD pole figure with 175 µm field of view of CS specimen in Spray direction. Arrow indicates the typical size of a single indent - 22x22 µm.**

### 3.3.3 Low Magnification Secondary and Backscattered Electron Pre-Indent Imaging

The last pre-indented image collection method used was BSE and SE imaging modes to collect micrographs in a lower magnification to allow for a larger data set. 185 µm FOV images were collected allowing room for an array of 12 indentation marks. Figure 27 shows a BSE micrograph of pre-indented microstructure with annotation of single indent size with respect to the FOV.

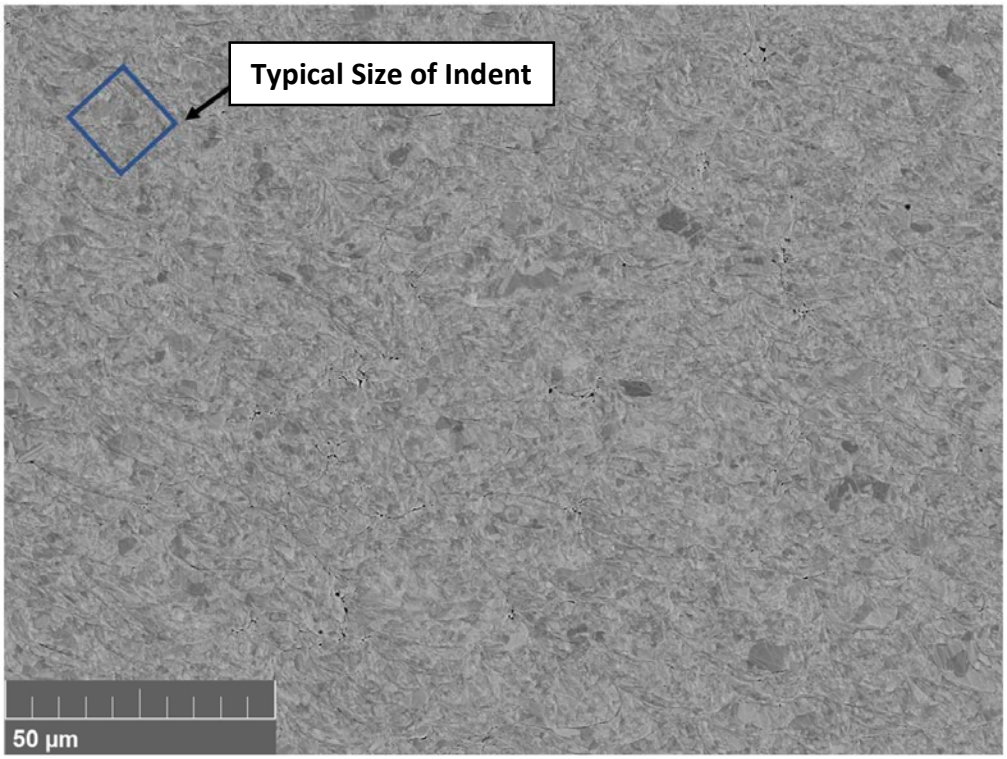


**Figure 27 Backscattered electron micrograph of pre-indented microstructure (185 µm field of view). Arrow indicates typical size of a single indent - 22x22 µm.**

## 3.4 Physical Measurements: Microhardness

Figure 28 illustrates the indentation process for aligning samples on the microhardness tester using the identifier image collection process referenced in Figure 24. All microhardness tests were taken using a Shimadzu HMV-G microhardness tester with a Vickers indenter. The Vickers indenter is used for ductile metal as opposed to the Knoop indenter which is reserved for harder and more brittle materials. Each sample was indented using 245.2mN force and held for a period of 10 seconds. The hold time allows the material to deform completely in the selected region before a measurement is taken. It should be noted that additional indents besides the initial 10 were not taken for the pressed powder specimen since the material was used for control due to its large homogenous grain structure, and the results showed a low enough standard deviation that it was deemed not necessary.

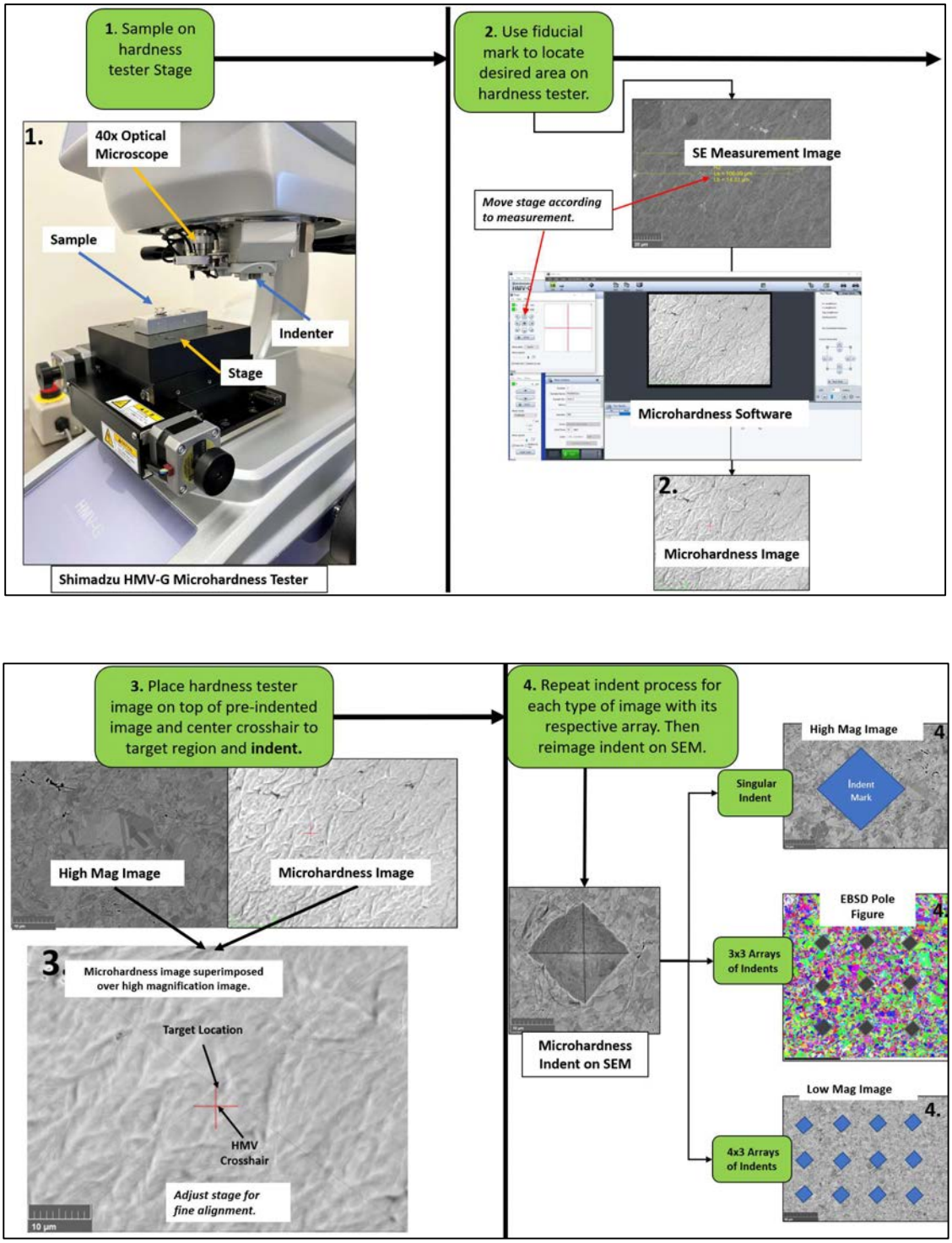


**Figure 28 Target indent location identification flow chart using HMV-G Microhardness tester.**

## 3.4.1 Process for Correlating Pre and Post Indent Images

Figure 29 illustrates the process of superimposing the post-indented images over the pre-indented micrographs. This process was used for all imaging techniques including high magnification, EBSD, and low magnification arrays. PowerPoint was used to combine both pre and post-indent images into one figure. The post-indentation image was first placed over the pre-indented micrograph and the transparency was adjusted to allow for the pre-indented imaged to be seen underneath. Microstructural features were lined up, and an outline was applied around the perimeter of the indent. The remaining microstructure within the outline was used for analysis to calculate the area fraction of HDR captured within the indent.

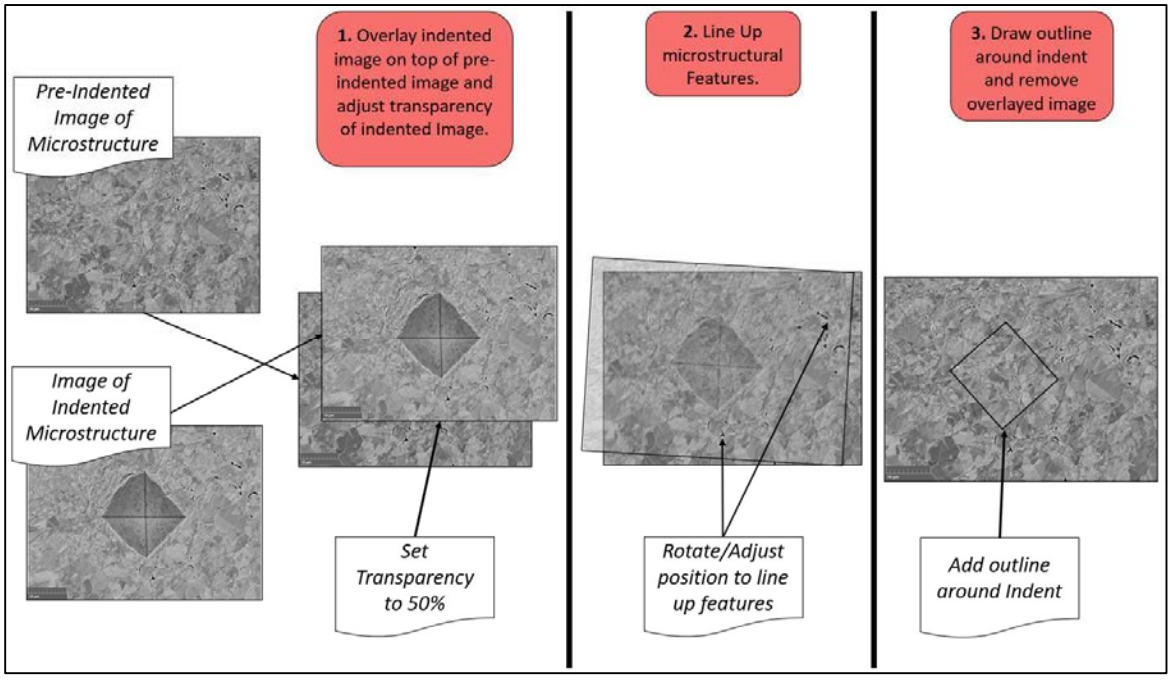


**Figure 29 Flow chart showing process for superimposing post-indented image over pre-indented micrograph.**

## 3.5 Scanning Probe Microscopy

All SPM imaging and atomic force measurements were performed using a Shimadzu SPM 9700HT. Each specimen was transferred from SEM stubs to SPM aluminum disks and the 125 µm stage was used to allow for a sufficient scanning window across each sample. Topographical images of the samples were first generated in dynamic mode using tapping to avoid interference with the polished surface while optimizing the parameters necessary for quality imaging. Images were collected in tapping mode to extract surface characteristics about the material. The contact probe was then used to create force curves and nanomechanical maps of the material. Two nanomechanical maps were collected on both transverse and spray direction CS samples for comparison. Each map contained an HDR and LDR with 2x2 µm windows and 8x8 pixel density for a total of 4 maps.

## 3.6 Area Fraction Analysis Process Using Image-J

To assess percentage of HDR captured withing the indent region, Image-J software was used. Image-J is a processing program where micrographs can be manipulated and analyzed using a variety of different tools. Figure 30 shows the process of area fraction analysis for a high magnification CS spray direction indent. The process begins with setting the scale of the image with reference to the number of pixels. Next, the total area of the indent is measured using the indent outline created previously. Third, the polygon selection tool is drawn around the HDRs

and finally, a percentage is calculated by dividing the area of highly deformed grains by the total area of the indent. It should be noted that this method is subjective, and the region captured within the outline is only an estimation. Porosity and regions where particles that failed to adhere were also avoided during outlining. This process was repeated for all CS images.

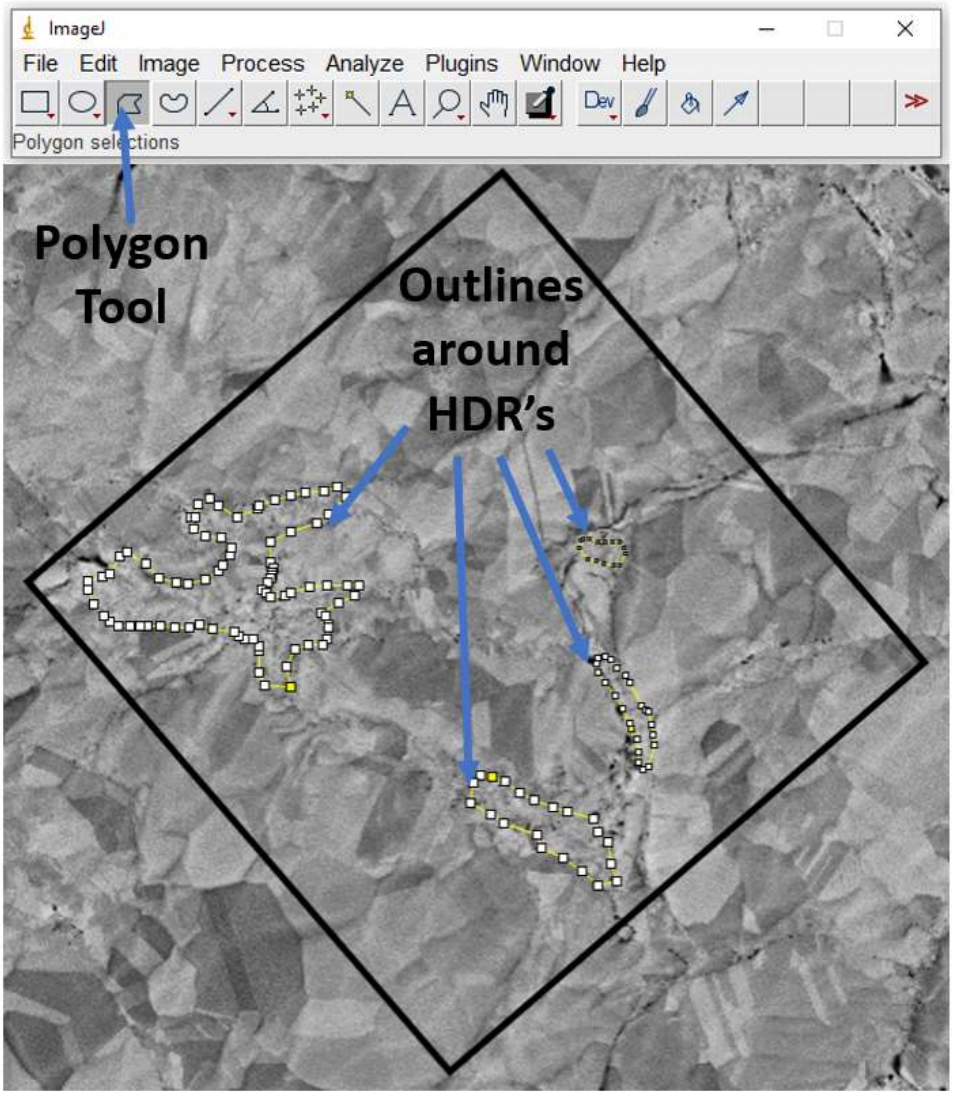


**Figure 30 Image-J analysis software with cropped high magnification indent outline. Arrow indicates the polygon selection tool and regions of highly deformed grains outlined by the tool.**

# Chapter 4: Results and Discussion

## 4.0 Results Introduction

The results are presented in the following order. First, an assessment of the results and issues associated with the polishing procedure. Second, characterization of the microstructure of each sample type including pressed power, CS spray direction and CS transverse Direction. Then the remaining section are divided into the type of experiment conducted. The 3 types of experiments were the High magnification images, EBSD, and Low magnification images, each with their respective indent pattern. The purpose of this order was to initiate the data analysis with the most accurate assessment of grain size compared to microhardness by analyzing the high magnification series of indents first. Then, decrease magnification slightly but still employ a more powerful characterization technique using EBSD. Lastly, then use the low magnification images to assess area fraction with the largest data set. The last method explored for microstructural characterization was imaging and nanomechanical testing using a SPM.

### 4.0.1 Polishing Procedure Discussion

Many of the resources available for mechanical polishing use methods established for industrial metals which allow for a wider tolerance in surface finish. Polishing severely deformed high purity (99.92%) copper to a finish capable of resolving sub-micron grains with EBSD required a much more nuanced approach. Removing the strain imparted by grinding

while avoiding smearing and particle pullout was a major point of contention. Typically, a vibratory polishing step is used to gently smooth the surface to a final mirror finish, but chemical etching proved to be a problem. The nature of vibratory polishing requires the metal to bathe in a polishing solution for hours at a time. Typical final prep solutions contain colloidal silica or a combination of silica and aluminum. These solutions resulted in either an insufficient polish or significant grain boundary etching rendering the sample useless for mechanical testing. Several methods were attempted to achieve the high-quality finish needed for EBSD and the result required use of an ion mill for a final polishing method. Although a more conservative procedure than prescribed by the manufacturer was used, a reduction in hardness was still seen after non-ion milled specimens were tested with the microhardness tester. The reduction in hardness was most significant in the sprayed direction of the CS material with approximately 25% reduction. However, since this reduction in hardness was consistent through all specimens surveyed a correlative assessment was still possible with the images and hardness data generated.

A second issue stemmed from the required use of the ion-mill for final polishing. Since the instrument requires samples to fit on 12.7mm SEM stub an additional source of possible error arose during the indentation process. After removing mounted samples from their epoxy pucks, the gravity induced flatness on the opposite site of the puck established during the cure was lost. Since the HMV-G requires a flat specimen to generate quality indents a method for leveling the specimens for indentation was also necessary. This leveling procedure was done by hand using tape to elevate the sides of the sample out of focus on the 40x HMV-G Lens. Since

each indent array was not taken during at the same time, the sample was re-leveled each time a new indent or array was taken. This re-leveling left room for uncertainty as it was impossible to ensure the same degree of flatness was established each time the sample was placed on the indenter stage.

## 4.1 Microstructure of Cold Sprayed Material

Figure 31 shows the spray direction CS sample in SE mode. Several aspects about the microstructure can be seen in the image. First, a clear circular outline can be seen from a splat particle with distinct jetting regions containing highly deformed grain structure. Second, several areas within particle boundaries show low deformation characterized by “Pancaking”. Figure 32 shows the same sample in BSE mode with twinning and lack of adhesion indicated by arrows.

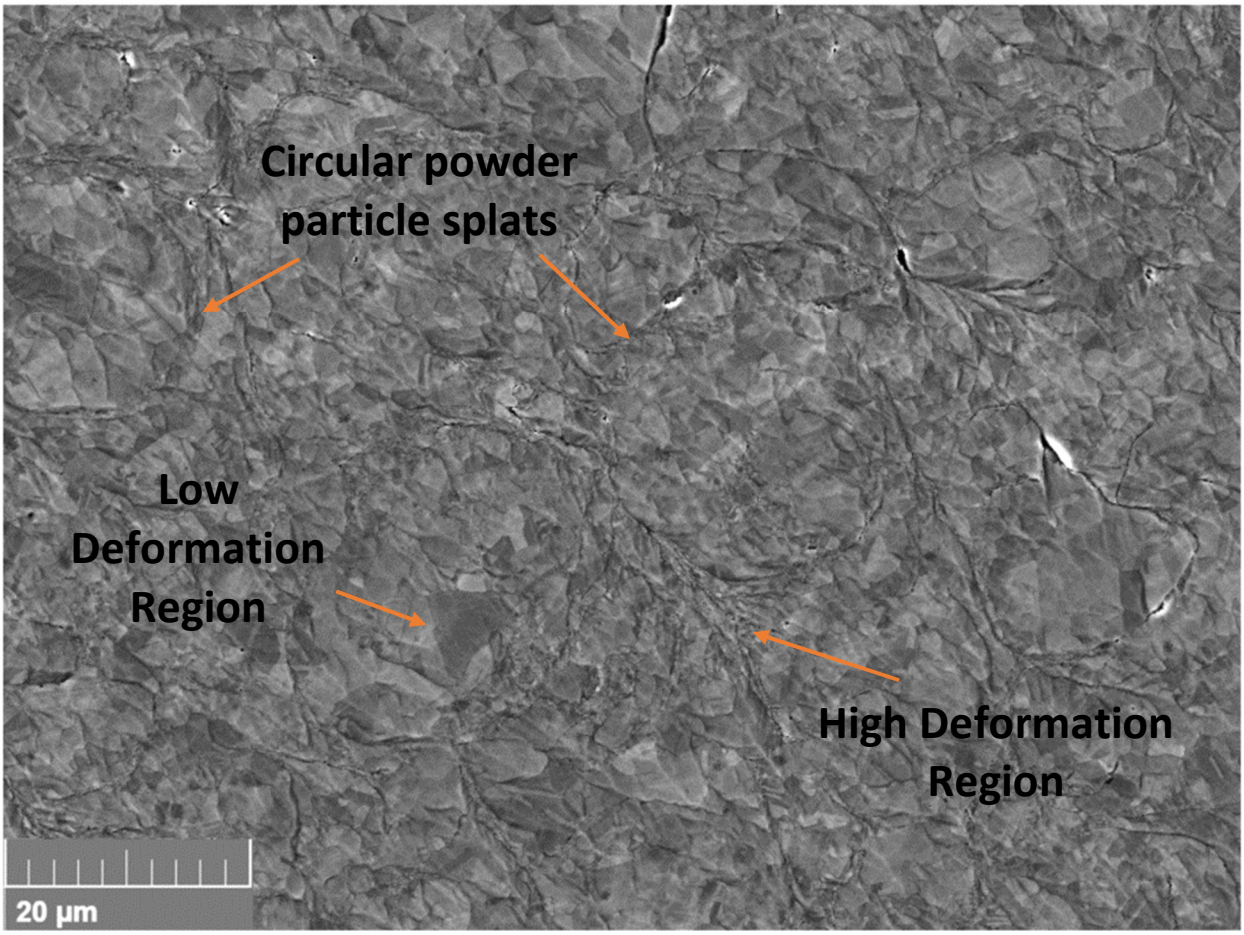


**Figure 31 SE micrograph of CS material oriented in the spray direction. Arrows indicate the characteristic high and low deformation regions. Also indicated are two particles that retained their circular shape after splat.**

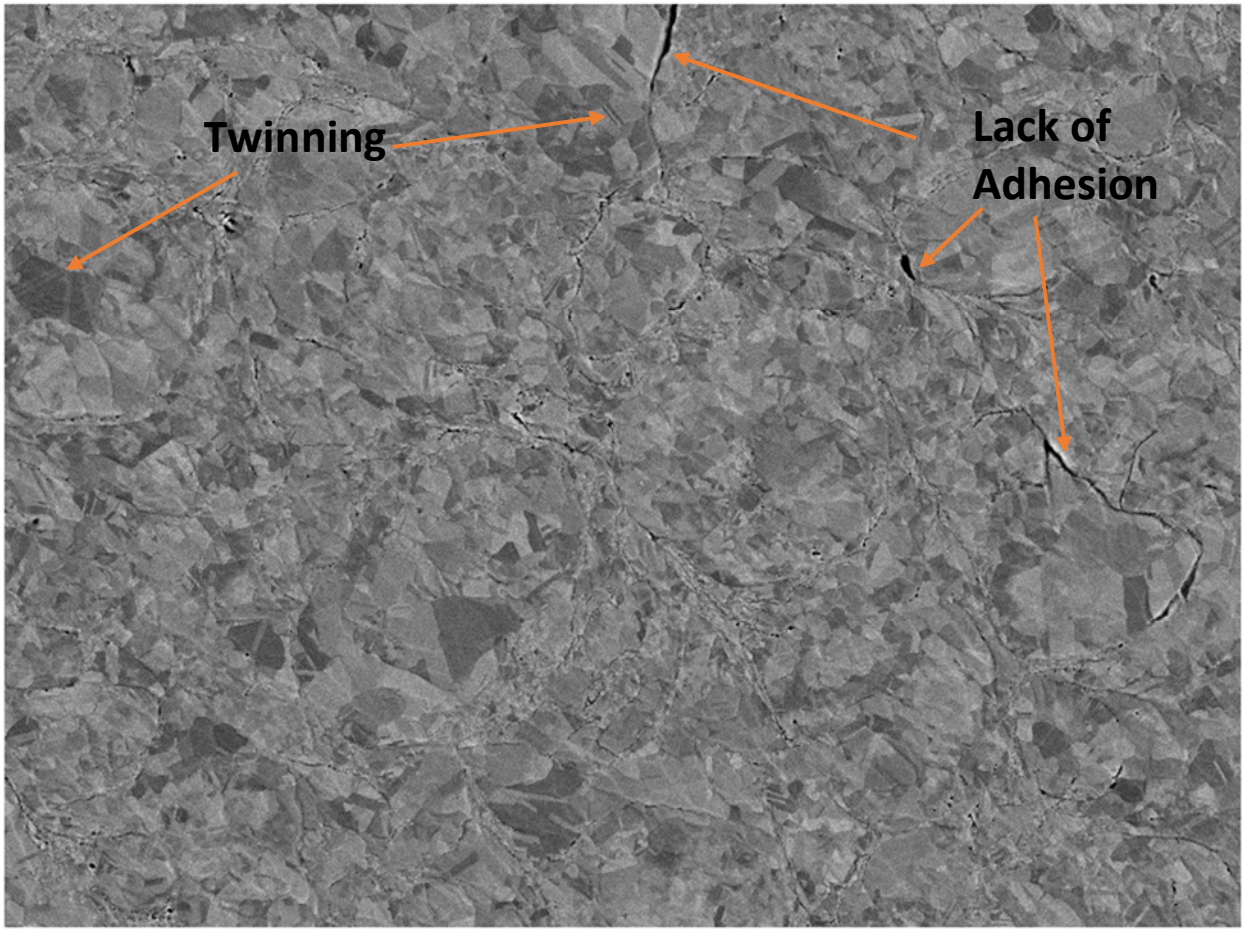


**Figure 32 BSE micrograph of CS material in the spray direction. Arrows indicate regions during deposition where particles did not completely adhere as well as twinned grains spread throughout the microstructure.**

Figures 33 and 34 show micrographs of the same copper CS deposits taken in the transverse direction or orthogonal to the spray direction. From this view several other characteristics about the material can be seen. The layering of particles as the bulk structure builds upon itself is evident, as well as several highly deformed regions exhibiting micron and nanometer grain size.

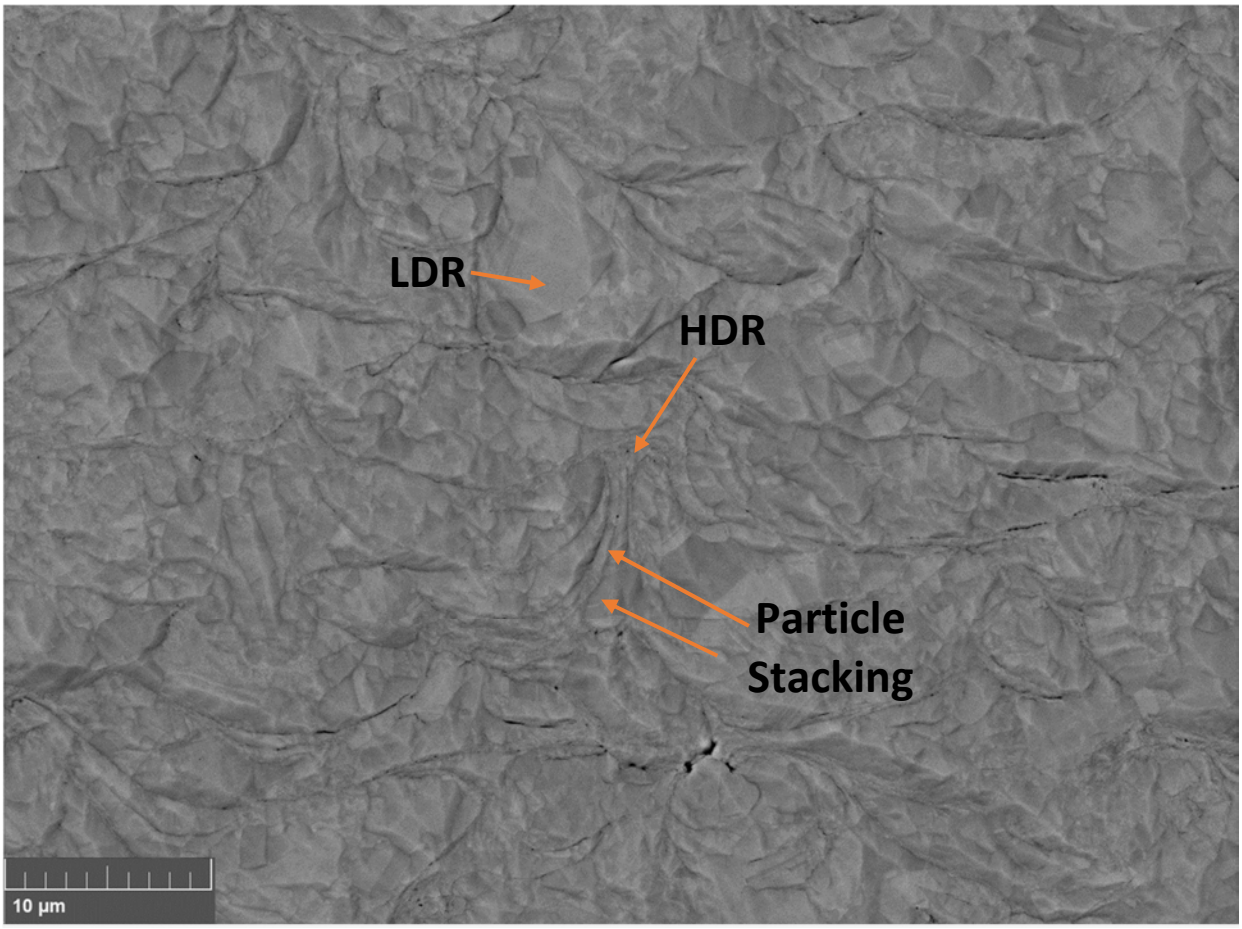


**Figure 33 SE micrograph of CS material in transverse direction. Arrows indicate particle stacking regions as well as low deformation and high deformation regions.**

Figure 34 also highlights a region outside of any obvious HDR but exhibits a structure that appears to be a bent crystal also called a “Tie Dye” Region. The region is relatively large compared to the size the particles which measure roughly 10-20 µm in diameter. A possible explanation for this microstructure is due to the immense plastic strain imparted during the CS process. Several particles stacking with high impact forces may lead to these bent crystal

regions and high localized temperatures may have caused some dynamic recrystallization during deposition as well.

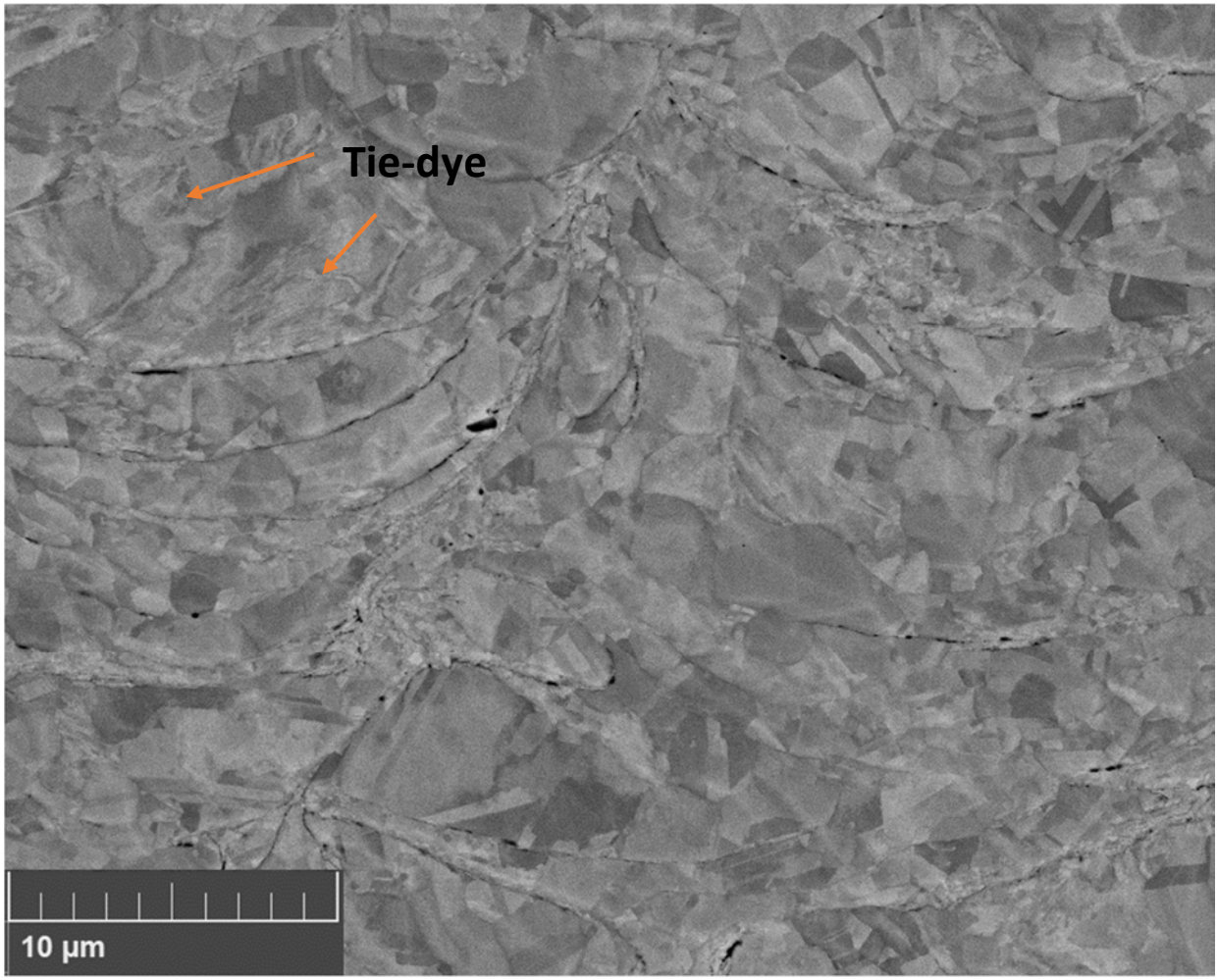


**Figure 34 BSE micrograph of CS material shown in transverse direction. Arrows indicate tie-dye region.**

Figure 35 is a high magnification BSE image depicting the same type of tie-dye region. The abrupt change in microstructure from the right side of the image to the left is also apparent. Several grains of uniform size are distinctly separate from the tie-dye zone.

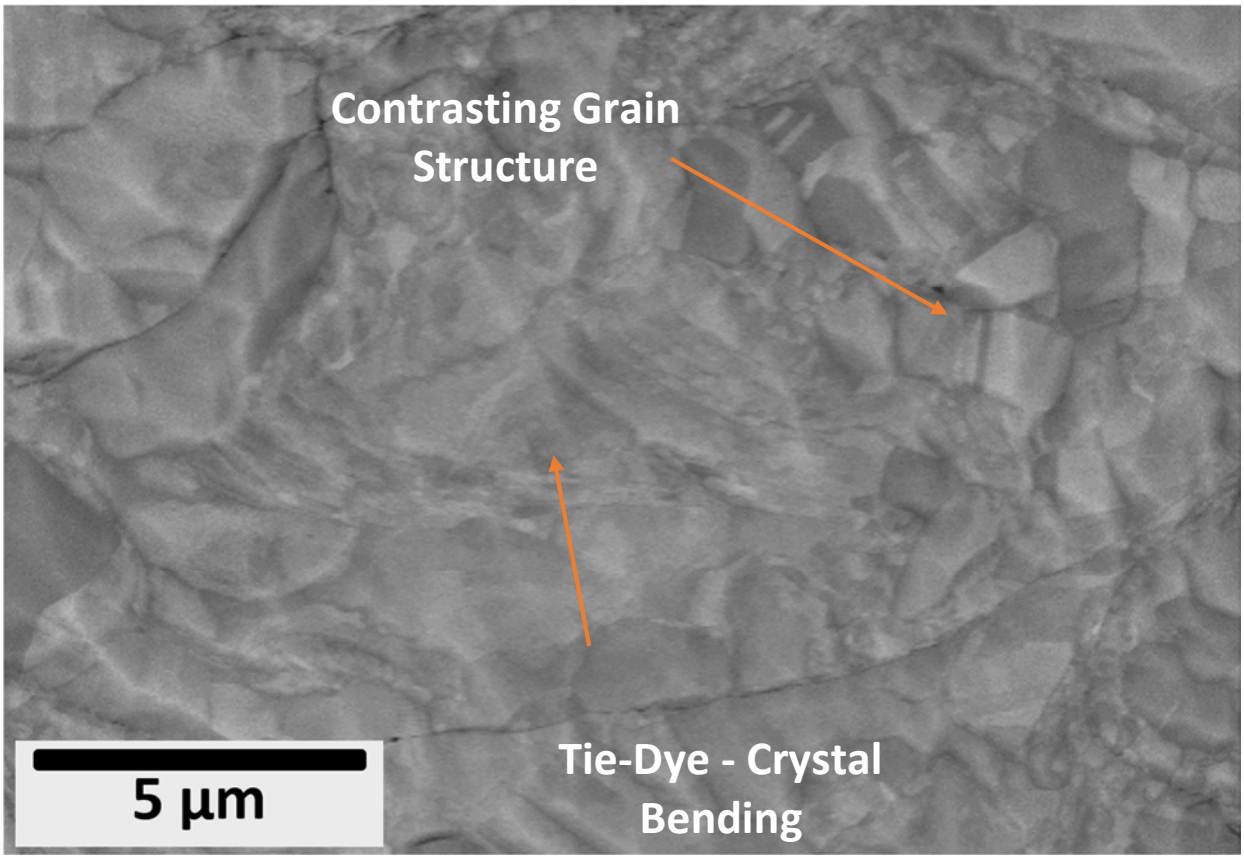


**Figure 35 BSE micrograph of CS material with arrows indicating tie-dye region next to contrasting grain structure – (transverse direction).**

## 4.1 Characterization of Pressed Powder Material

SEM micrographs of the pressed powder material in BSE and SE mode are shown in Figure 36 and Figure 37 respectively. In Figure 36 several features of the microstructure are apparent. Firstly, multiple large grains are present with some reaching 100 µm in diameter. Secondly, the microstructure is relatively homogeneous and twinned grains are also present

throughout the microstructure appearing within large (<100 µm) grains. Porosity can be seen resulting from the hot isostatic pressing process.

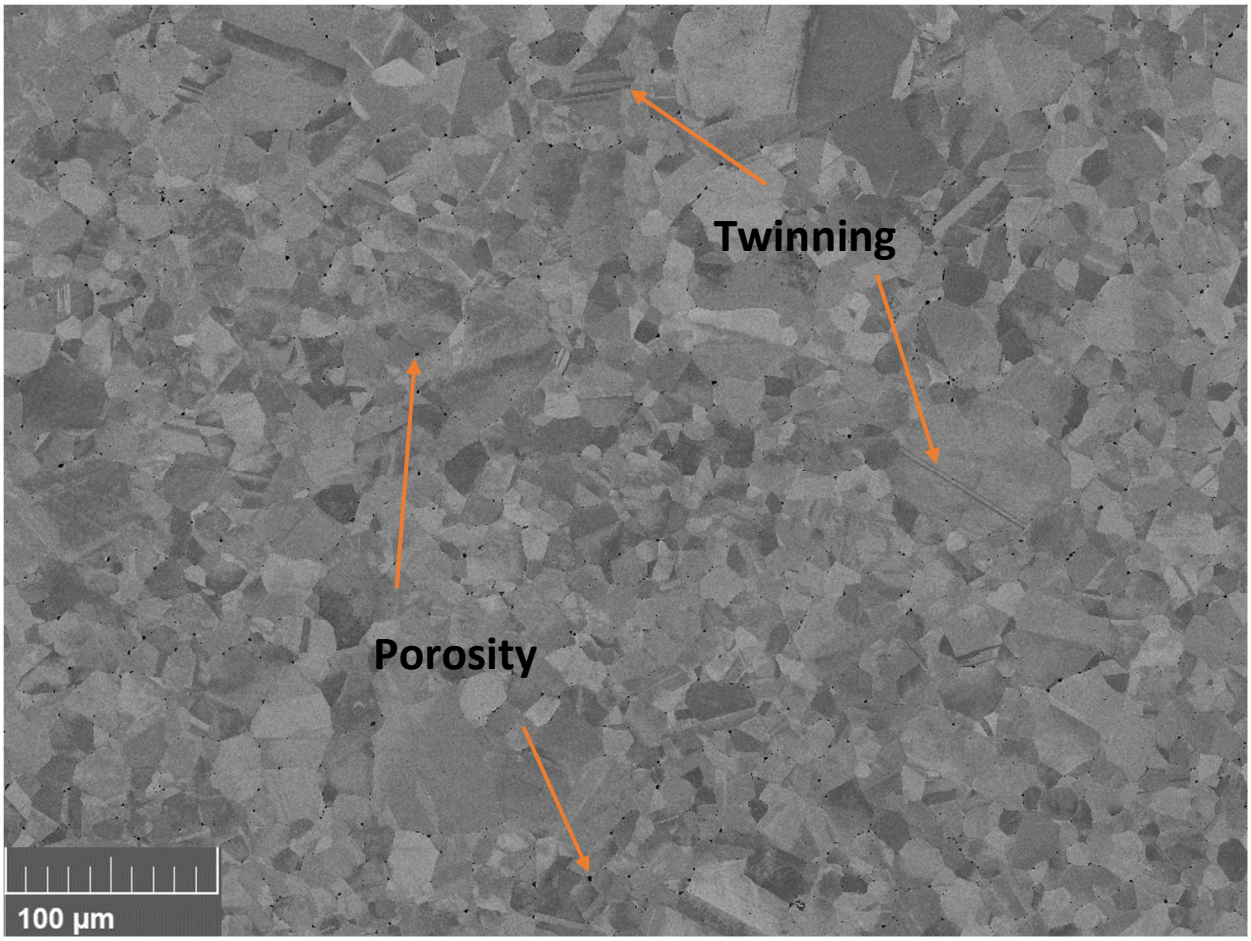


**Figure 36 BSE micrograph of powder pressed specimen. Arrows indicate porosity as well as twinned grains throughout the microstructure**.

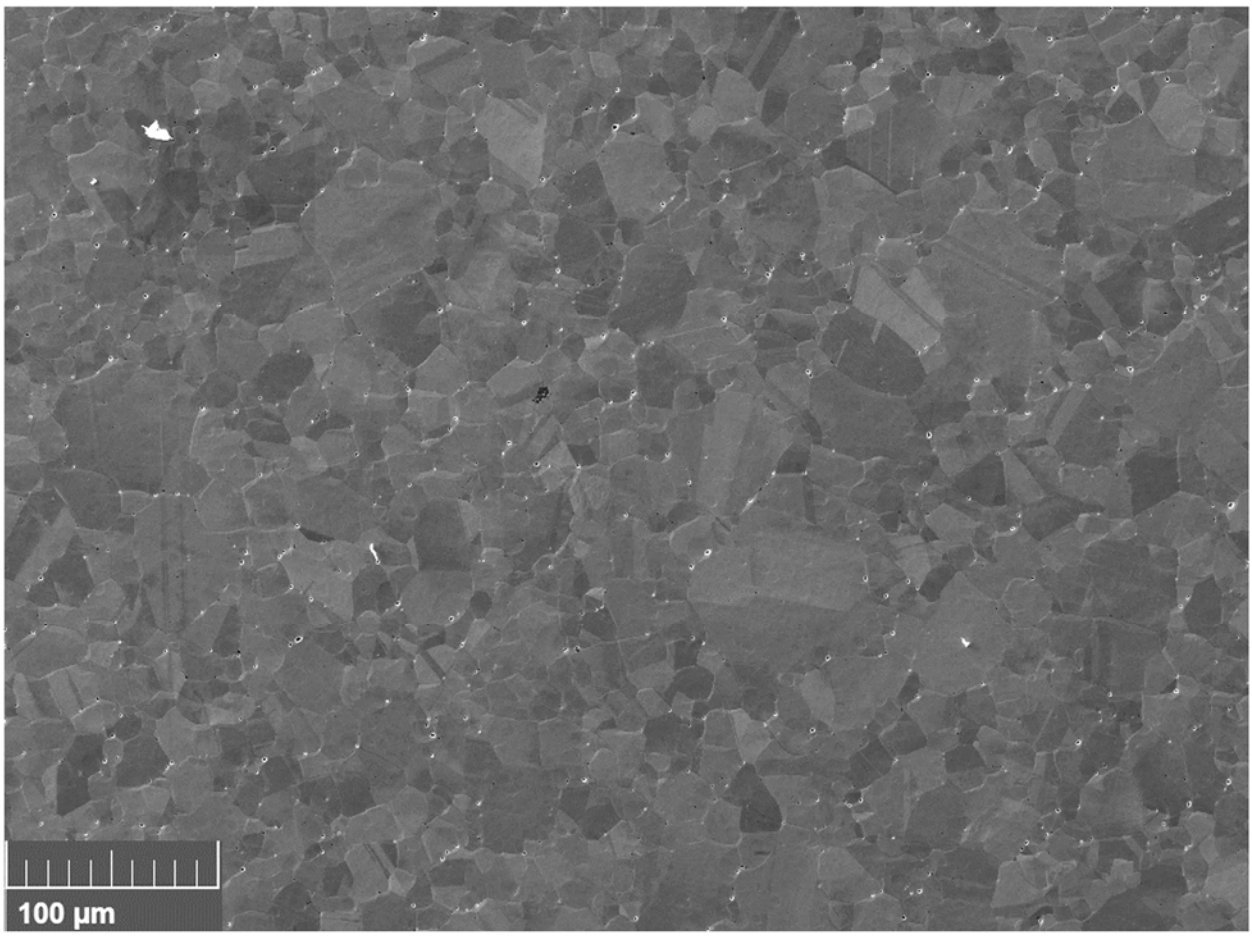


**Figure 37 SE micrograph of pressed powder showing less topography than the sprayed material.**

Figure 37 illustrates the lesser degree of topography of the pressed powder when compared to the sprayed material. Both specimens were prepared using the same polishing procedure, but the surface topography more apparent in the sprayed material. This may stem from differential milling rates of the sprayed microstructure when ion milled or preferential mechanical polishing due to the inhomogeneous sprayed microstructure.

## 4.2 EBSD Results and Analysis – Cold Spray

EBSD characterization was performed using both Tescan MIRA and Tescan AMBER SEMs. Figure 38 shows a band contrast and inverse pole map for a mixed deformation region on a transverse direction CS sample. Multiple interparticle regions exhibiting high deformation can be seen. Additionally, intragranular strain represented by color gradients have also been labeled. These tie-dye gradient regions are indicative of bent crystals as the Kikuchi index rotates along the length of these regions rather than changing crystallographic direction entirely. These high strain regions are not present in the pressed powder maps and therefore likely stem from the immense strain imparted during the CS process. Figure 39 shows band contrast and EBSD pole figures for the CS sample in the spray orientation. Both figures exhibit similar levels of deformation in the HDR, however, the HDR's also do not appear to be dominated by any orientation. There also does not appear as many tie-dye regions in the spray direction pole figure either. Impact forces causing deep penetration and particle stacking may be the result of these bent crystals in the transverse orientation, whereas the spray direction HDR's are dominated by jetting.

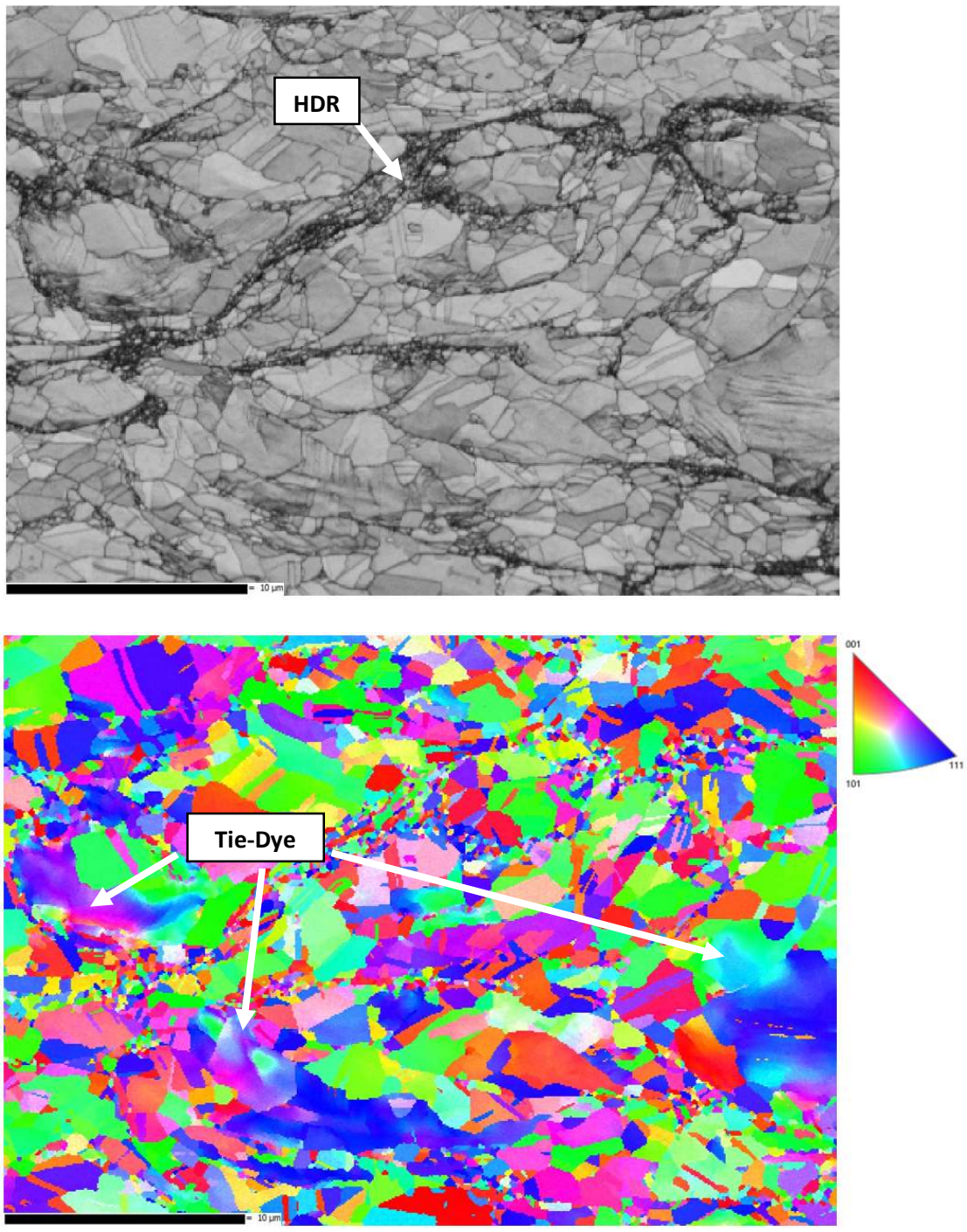


**Figure 38 CS sample oriented in the transverse direction. (Top) Band contrast image with high deformation region highlighted. (Bottom) Inverse pole figure in Z-direction - Arrows indicates tie-dye regions.**

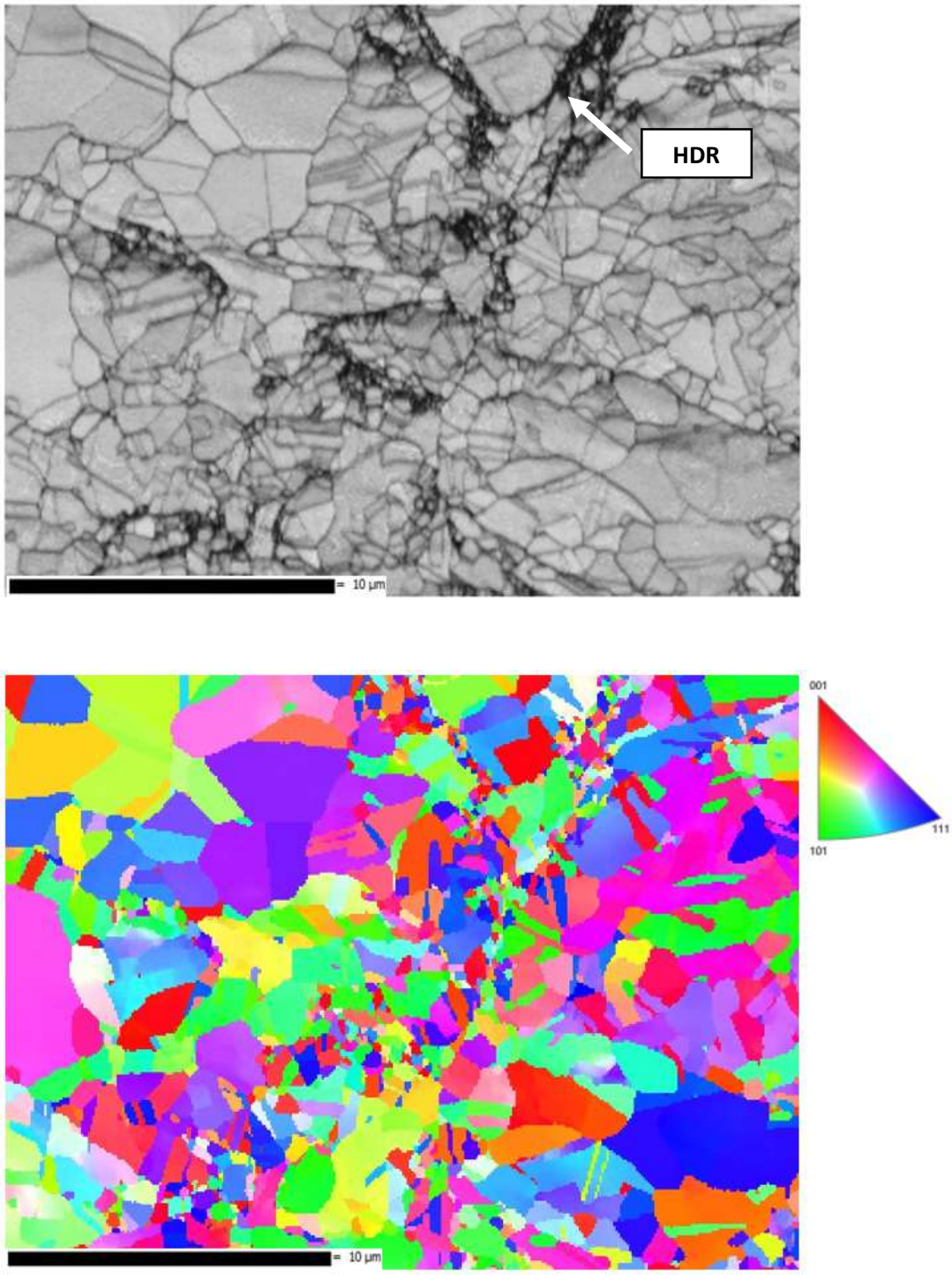


**Figure 39 CS sample oriented in the spray direction. (Top) Band contrast image with arrow indicating high deformation region. (Bottom) Inverse pole figure in Z-direction.**

## 4.3 EBSD Results and Analysis – Pressed Powder

Characterization of the pressed powder microstructure specimen is shown in Figure 40 with band contrast image and inverse pole figure oriented in the Z-direction. The figure exhibits typical copper microstructure with large grains <25 µm and twinning making it ideal for a control group specimen.

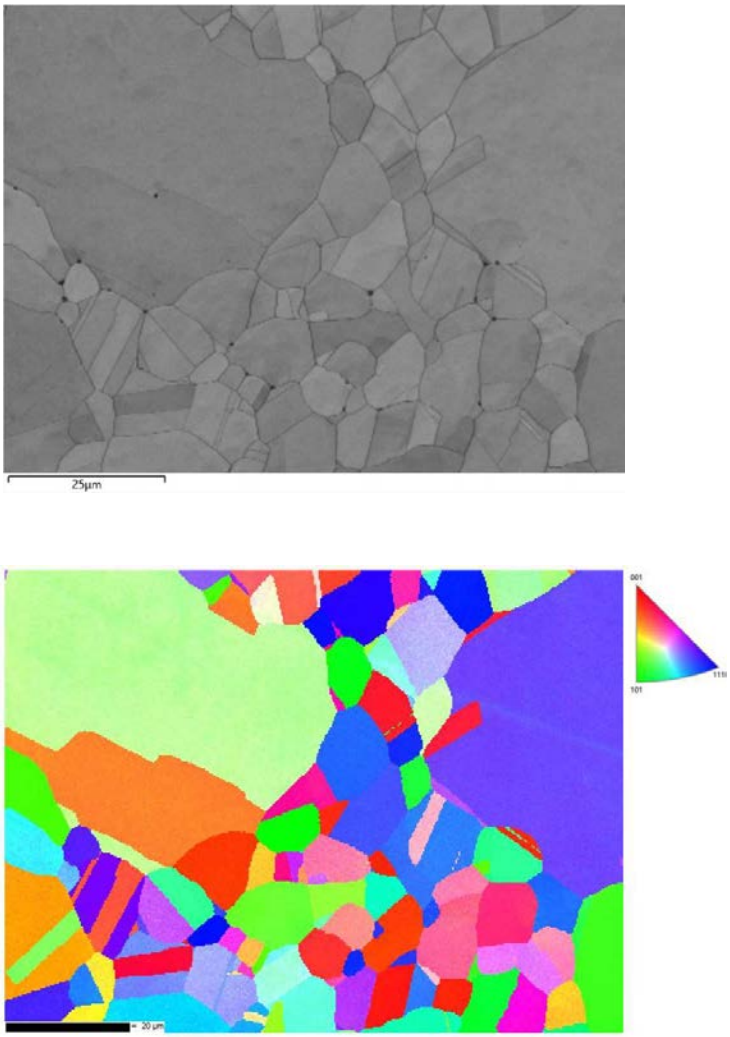


**Figure 40 EBSD figures for pressed powder. (Top) Band Contrast. (Bottom) Inverse Pole Figure in Z-Direction.**

## 4.4 High Magnification Images and Indentation of Cold Spray Material

The high magnification images and associated indents were each analyzed in Image-J and area fraction assessment data was calculated. In this section, only the highest indent and lowest microhardness value indent are shown for each CS specimen. The remaining indent micrographs are shown in the appendix. Figure 41 is a CS spray direction sample with a hardness outline over the original microstructure as described previously in Figure 29. Upon initial observation it's clear the higher microhardness value indent contains a larger fraction of highly deformed grains within the indent region. Using Image-J analysis software the area fraction of the HDR compared to the area of the entire indent was calculated. The Vickers microhardness value for indent #9 was calculated as 90.1 HV and the area fraction of high deformation grains was 7.46%. Figure 42 shows the lowest indent of the 10-indent spray direction high magnification array with a Vickers hardness value of 78.5HV and an area fraction of HDR of 2.05%. In Figure 42 the large grain located in the center of the LDR encompasses about 21% of the indent. There is also a large stacking fault connected to the grain with similar size grains around it which may influence microhardness.

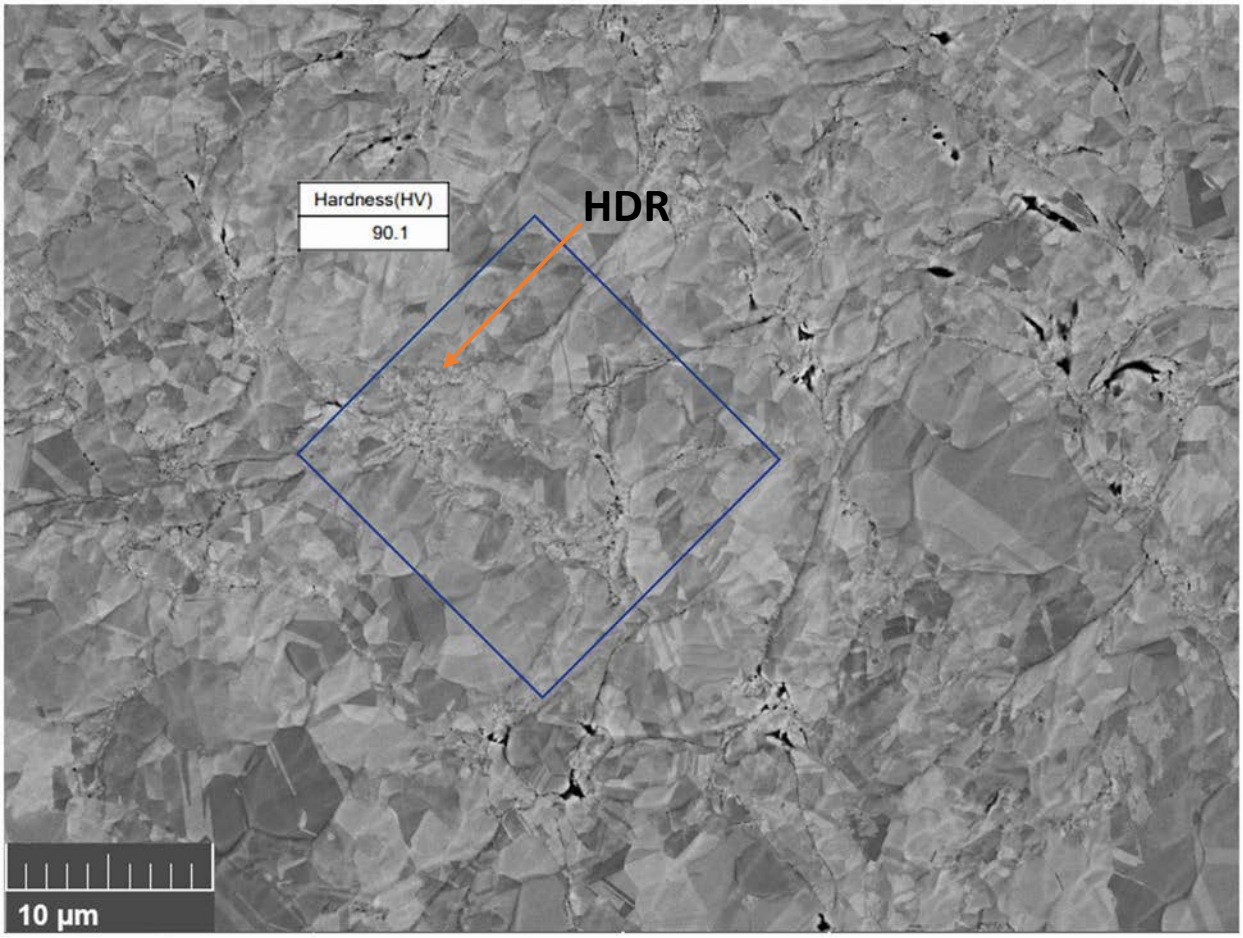


**Figure 41 Indent #8 shown in BSE from the high magnification images with outline of indent over pre-indented microstructure (Spray Direction CS) - Arrow indicates high deformation region.**

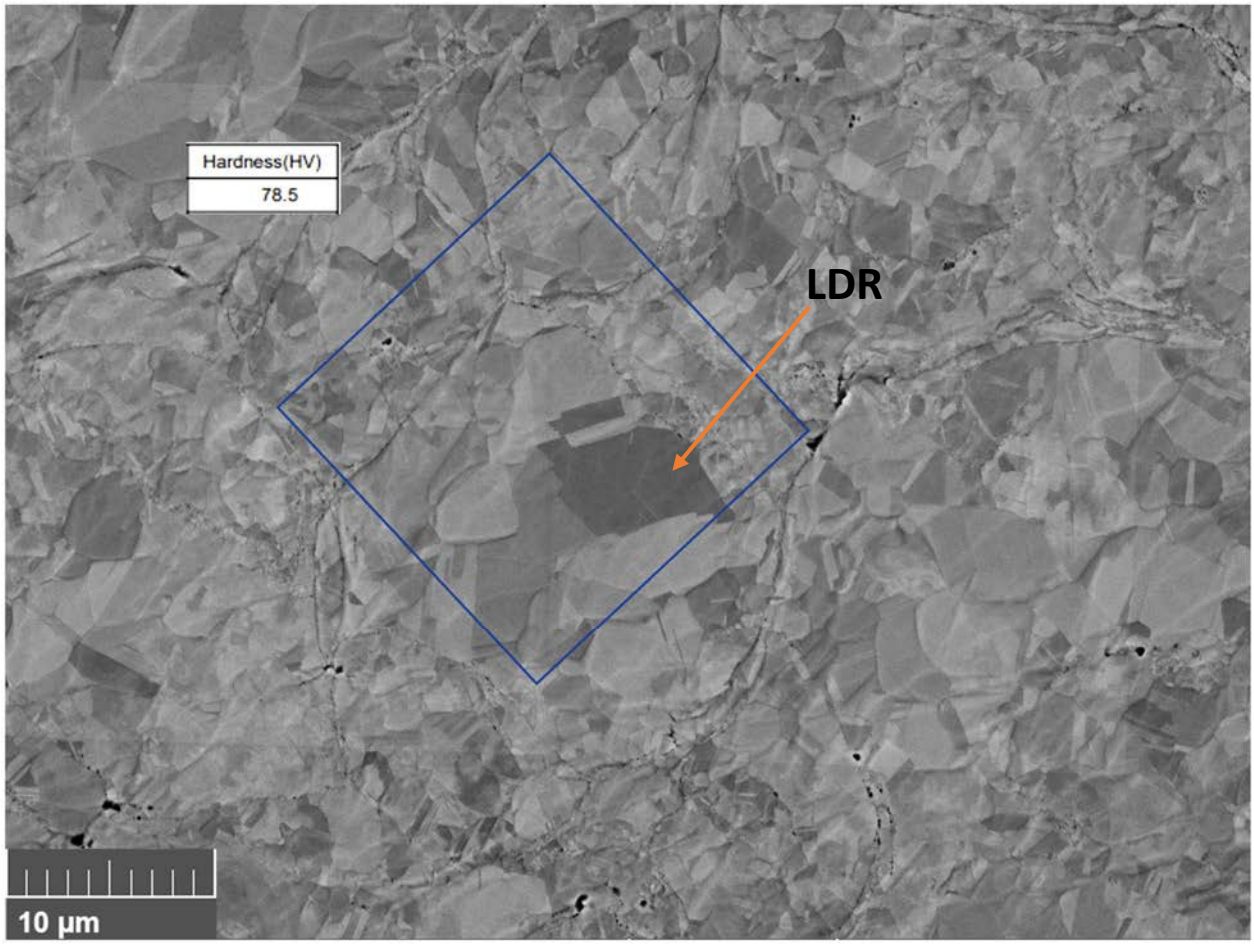


**Figure 42 Indent #2 shown in BSE from the high magnification images with outline of indent over pre-indented microstructure (Spray Direction CS) – Arrow indicates low deformation region.**

Figure 43 illustrates a direct comparison between the high (a.) and low (b.) microhardness value CS spray direction indents. Both indents appear to have the same misshapen perimeter with a larger portion of the deformation emanating from the left side of the indent. This may be a result of sample misalignment during indentation. Furthermore, larger grains appear to be present in the lower valued indent post-indentation indicating the depth portion unseen in the pre-indent images may contain a larger fraction LDR as well.

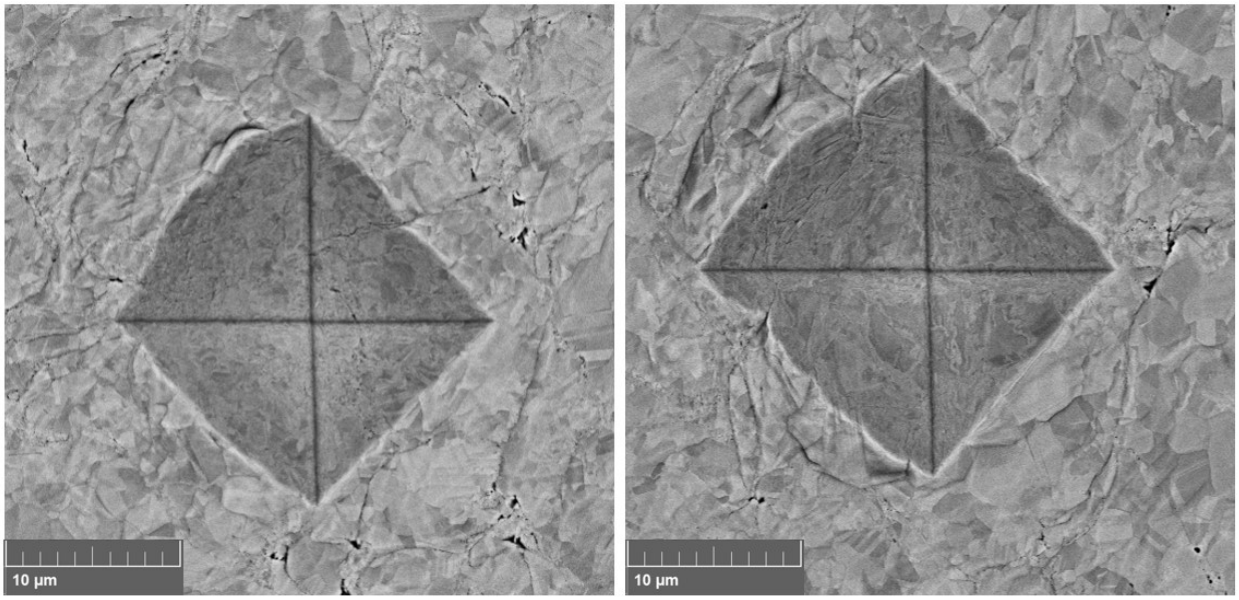


**Figure 43 (a.) High and (b.) Low, HV values for 10 high magnification image and indent series on spray direction CS Specimens - Images taken in BSE.**

Figure 44 is the highest microhardness value (Indent #2) of the transverse CS high magnification micrographs with a value of 110HV. Conversely, Figure 45 shows the lowest of the transverse individual indents (96.5HV) for the high magnification figure comparison. The area fraction assessment for Indent #2 vs Indent #9 is 7.30% and 6.75% Respectively. Figure 46 shows a side-by-side comparison between these two indents and the arrow indicates an area that poorly adhered in the upper right quadrant of indent #9. This lack of adhesion could be a result of not reaching the necessary CV or other missed process parameters and may explain the difference in microhardness between the indents despite the small difference in HDR area fraction.

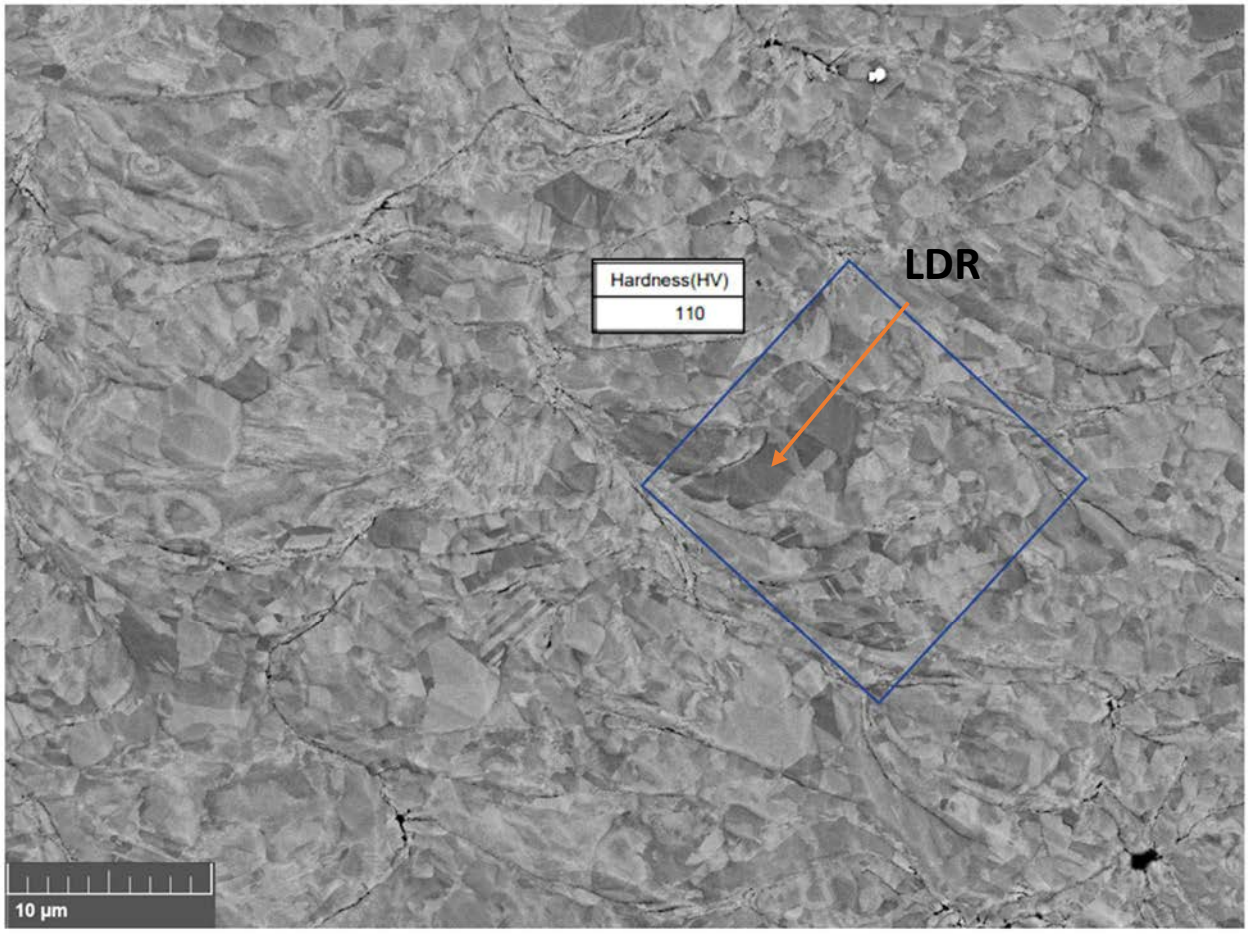


**Figure 44 Indent #2 shown in BSE from the High magnification images with outline of indent over pre-indented microstructure (Transverse Direction CS) - Arrow indicates low deformation region.**

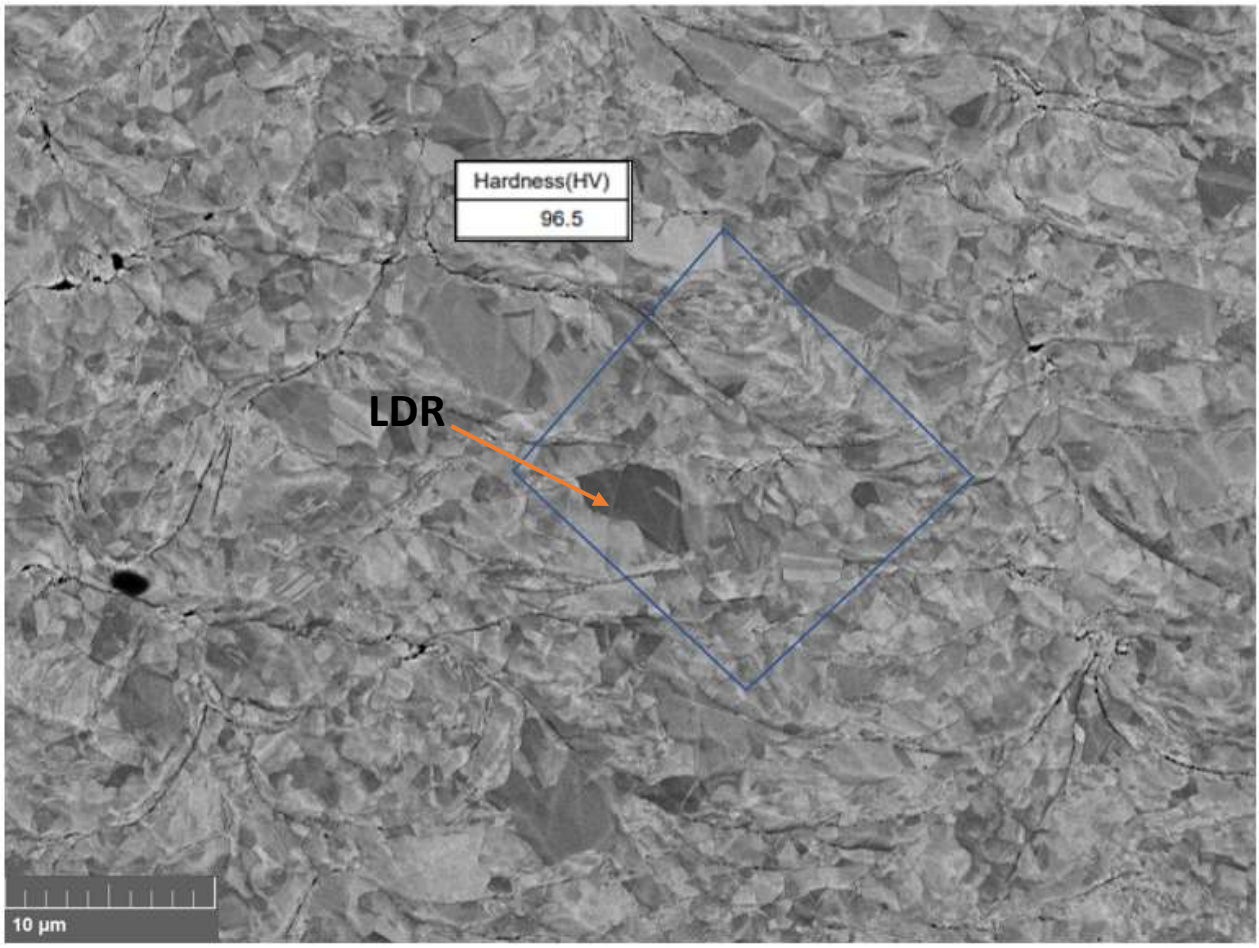


**Figure 45 Indent #9 shown in BSE from the high magnification images with outline of indent over pre-indented microstructure (Transverse Direction CS) - Arrow indicates low deformation region.**

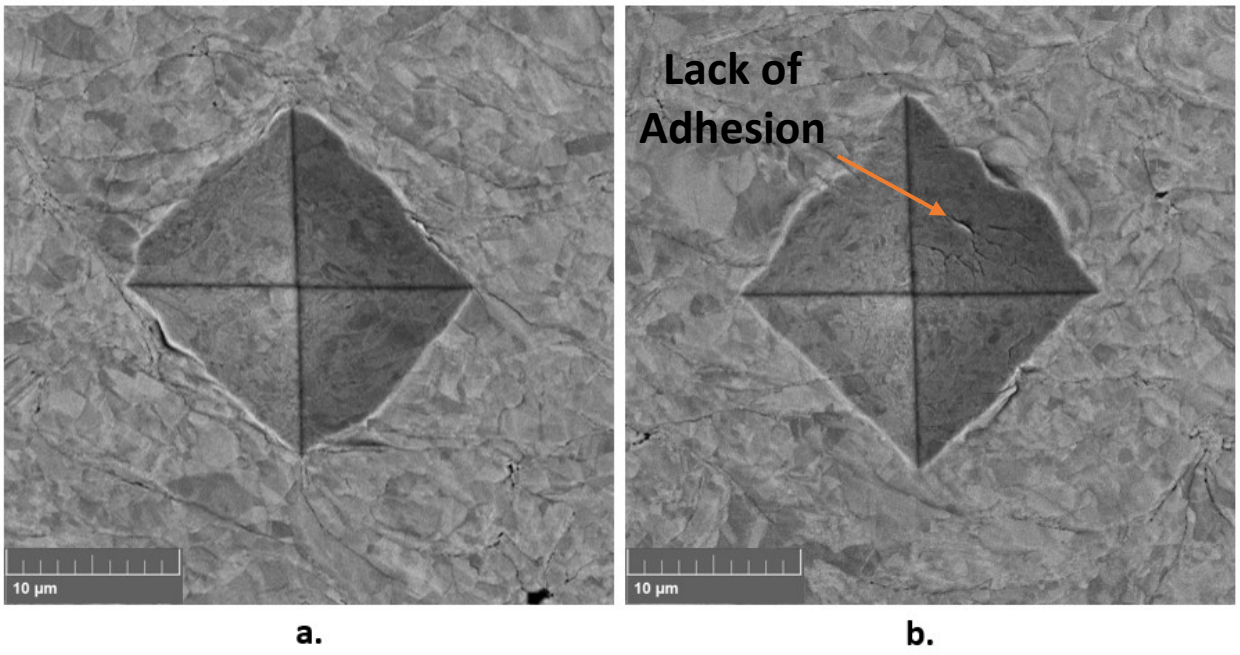


**Figure 46 (a.) High and (b.) Low, HV values for 10 high magnification image and indent series on Transverse Direction CS Specimens. Arrow indicates lack of adhesion on figure (b.) Images taken in BSE.**

## 4.4.1 High Magnification Images and Indentation of Pressed Powder

Indent test regions in the pressed powder material consisted of two micrographs taken prior to indenting. The grain sizes in the pressed powder microstructure were uniform and large enough that multiple indents could be captured in one pre and post image, improving process efficiency. Figures 47 and 48 shows indents 1-10 superimposed over the original image. The hardness data shows low variability no particular microstructural features correlated to level of microhardness. For this reason, it was deemed that no further indentation was necessary for the pressed powder specimen.

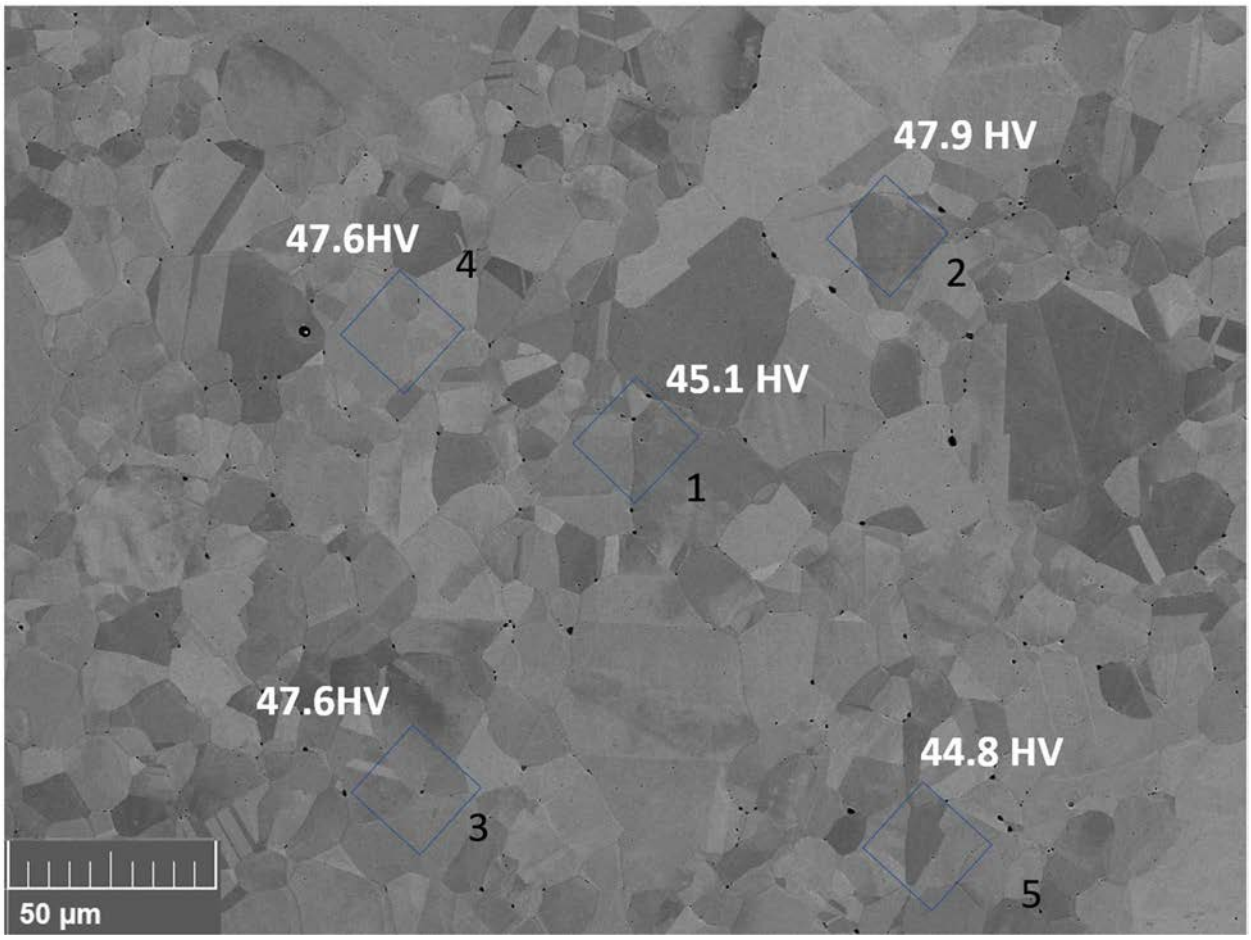


**Figure 47 Indents 1-5 from the high magnification images with outlines of indents over pre-indented microstructure (pressed powder). Image taken in BSE.**

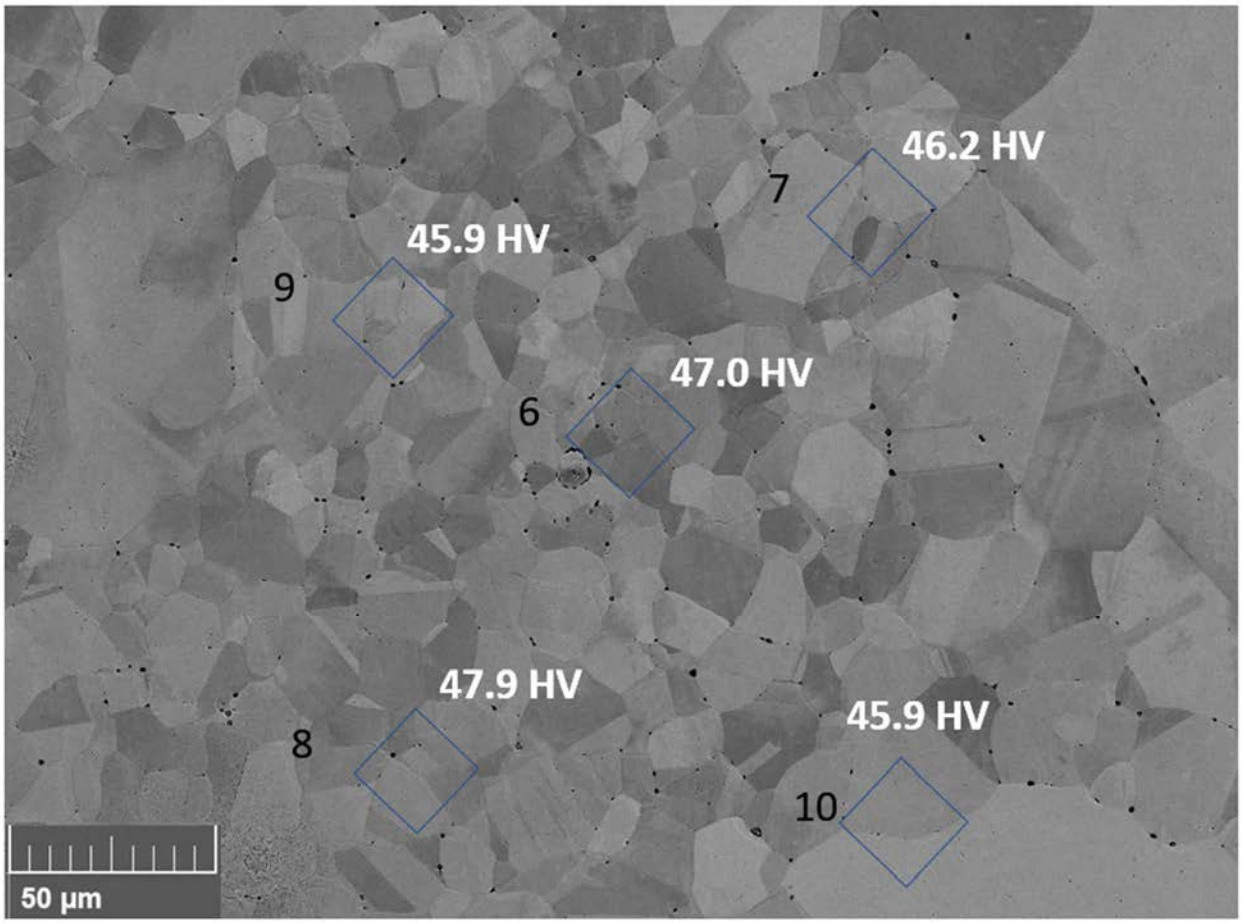


**Figure 48 Indents 6-10 from the high magnification images with outlines of indents over pre-indented microstructure (pressed powder). Image taken in BSE.**

## 4.5 Spray Direction and Transverse Direction Cold Spray EBSD and Indentation Arrays

Figures 49 and 50 are CS spray direction 3x3 indent array outlines over EBSD band contrast and inverse pole figures respectively. It's important to note that the same microhardness array is overlayed on both figures. Each indent is labeled with their associated hardness values and numbered 1 through 9. From a visual assessment of both images a general trend can be seen that indent regions with more HDR's tend to result in higher values of hardness. For example, when visually comparing the highest valued indent in the array (#2 - 91.7 HV) and the lowest valued indent (#1 - 80.4), its clear indent #2 has a higher fraction of HDR captured within the indent region. This HDR on indent #2 is indicated with arrows in Figure 44 and represents the largest single HDR captured within a single indent in this array. It's also important to note that while the entire HDR in indent #2 did not fall within the indent, the effect of the highly deformed grains may still have played a role in inhibiting dislocation motion during intending, thus resulting in higher hardness. Grain orientation does not appear to have as much of an affect as level of deformation. When observing the inverse pole figure in Figure 50 no crystallographic direction appeared to correlate with the level of microhardness. Each indent captured appears to contain a relatively even distribution of directions except for indent #7 and indent #6 containing a large proportion of 101 oriented grains. However, the widely different hardness values and lack of general trend suggests that orientation does not play a role in level of microhardness.

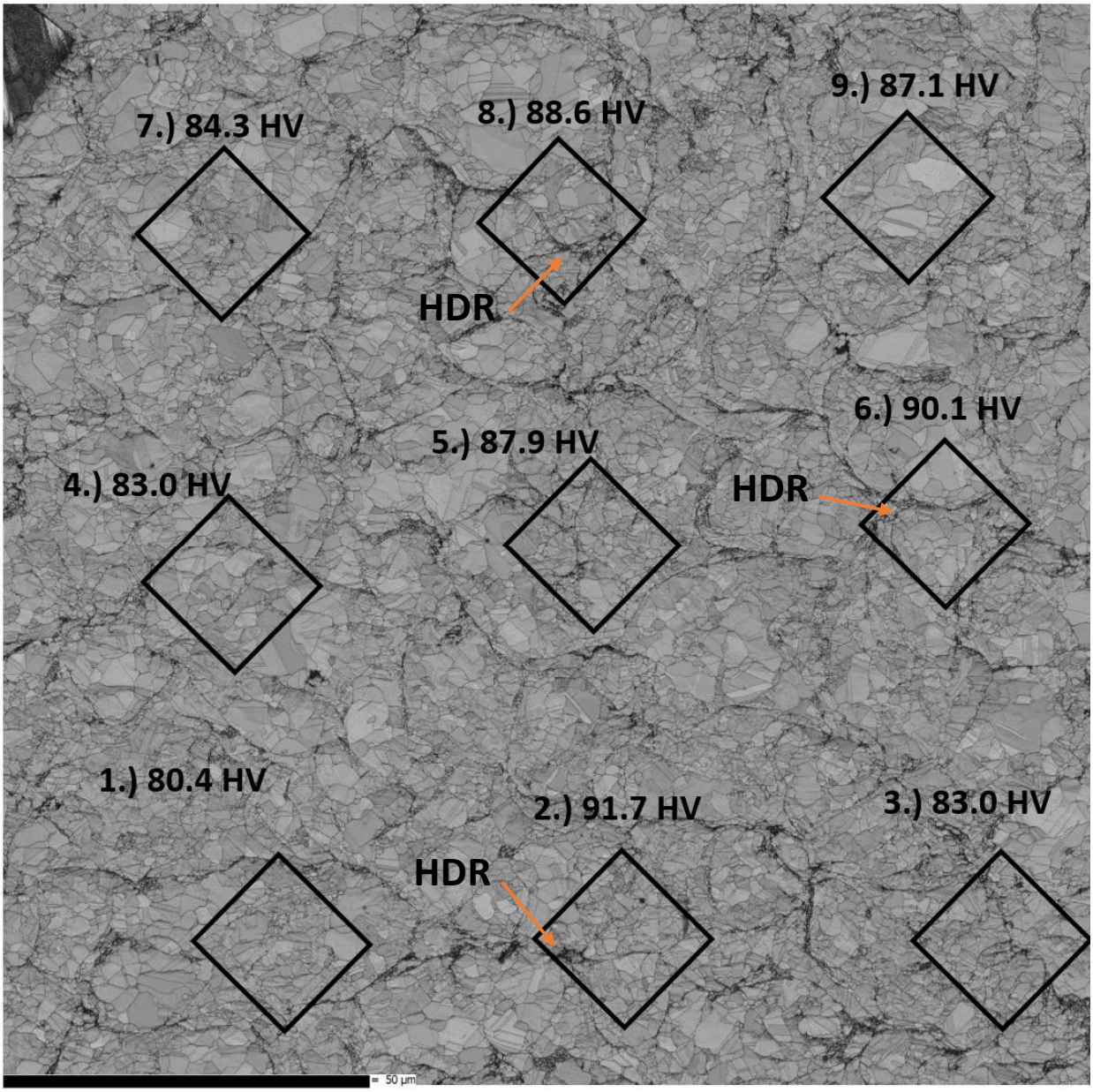


**Figure 49 Band contrast EBSD figure showing CS spray direction. Outlines of each Vickers microhardness indent and their associated microhardness values are indicated. Arrows indicate HDRs captured within the 3 indents with the highest microhardness values in the array.**

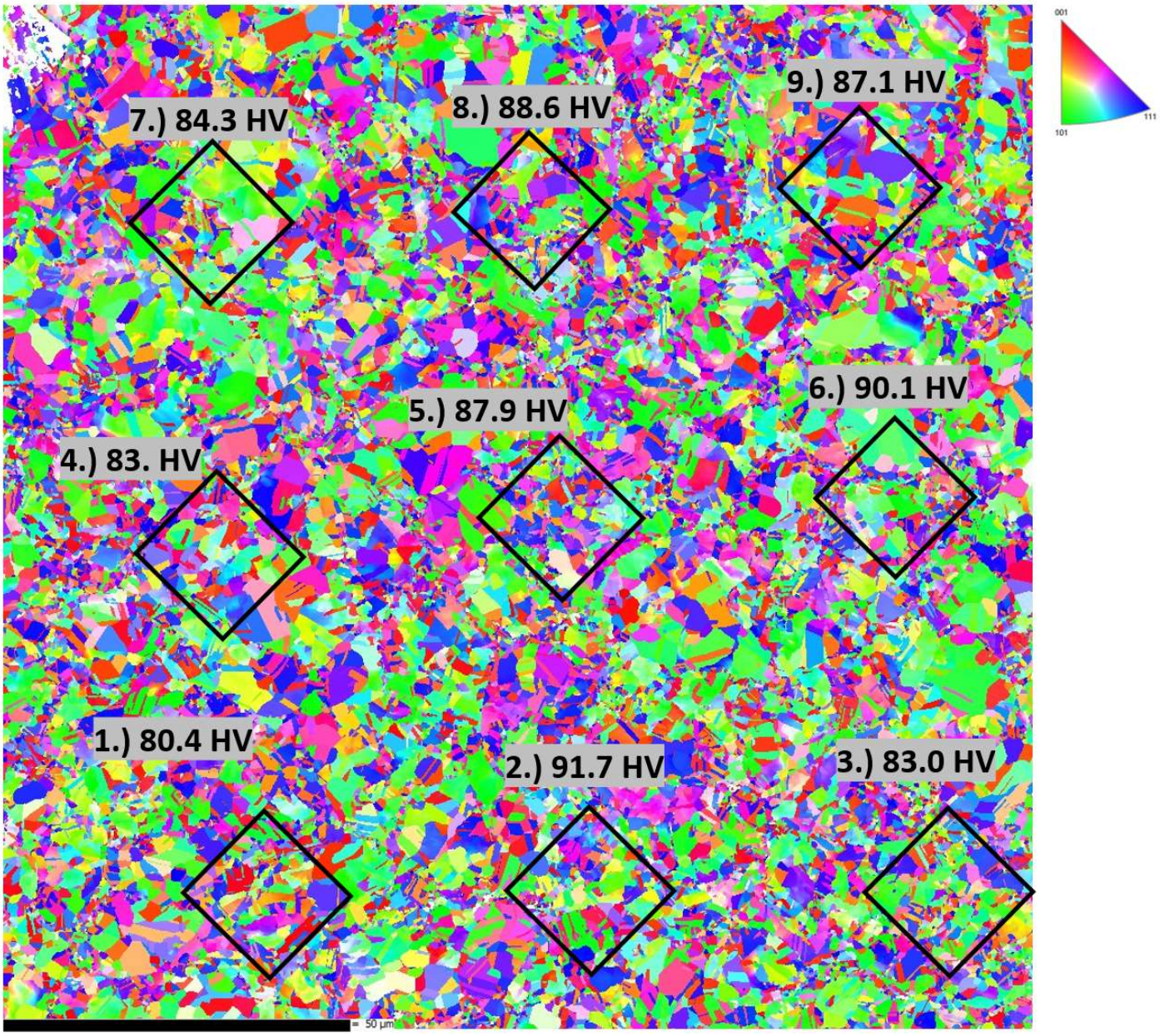


**Figure 50 Inverse pole figure in Z-direction showing CS spray direction specimen. Outlines of each Vickers microhardness indent and their associated microhardness values are indicated.**

An EBSD scan and 3x3 indentation array was also performed on a CS sample oriented in the transverse direction. Figures 51 and 52 show the CS transverse direction 3x3 indent array outlines over EBSD band contrast and inverse pole figures respectively. A visual assessment of these figures yields different results than the spray direction sample. Firstly, grain size appears to be more evenly distributed in the transverse orientation than the sprayed direction and the overall microstructure also appears to contain smaller grains on average as well. When comparing the highest microhardness indent to the lowest (#1 vs #9) there does not appear to be any significant differences in fraction of highly deformed grains captured within the region. Furthermore, comparing the next highest and next lowest indent (#5 vs #8) shows a slightly inverse trend. With the lower valued indent containing more HDR than the higher microhardness value indent. Grain orientation in the transverse direction was also taken into consideration. The pole figure in Figure 52 shows a greater level of homogeneity in the distribution of crystallographic directions than the spray direction specimen. For this reason, correlating grain orientation to microhardness was even more difficult in the transverse direction and no concrete assessments could be made. Lastly the microhardness values in the transverse EBSD data set were overall higher than the spray direction with less variance. This reduction in variance and increase in microhardness appears to be correlated to the even distribution of grain size and overall smaller grain structure.

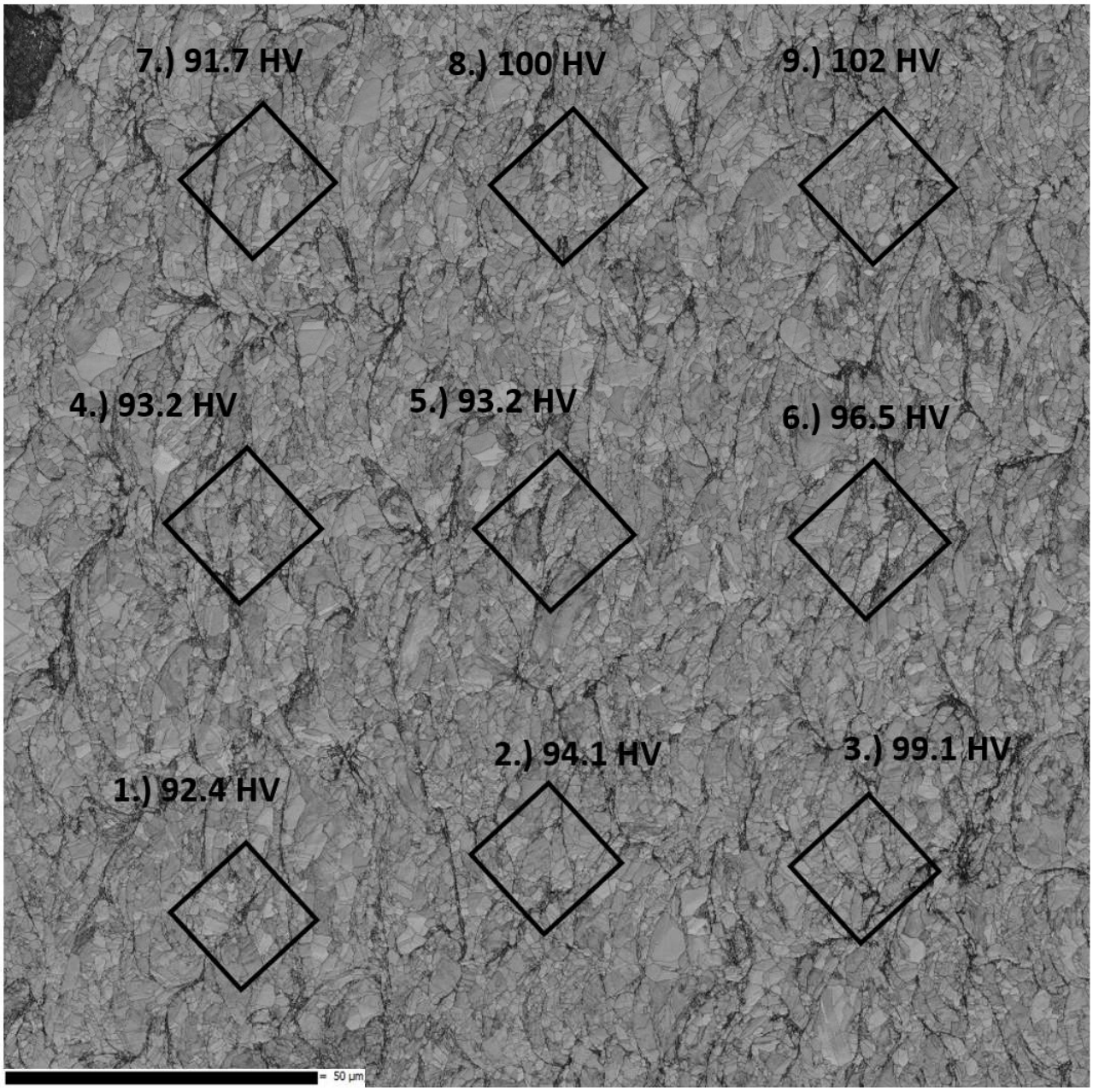


**Figure 51 Band contrast EBSD figure of CS transverse direction specimen with outlines of 3x3 indent array and their associated Vickers microhardness values.**

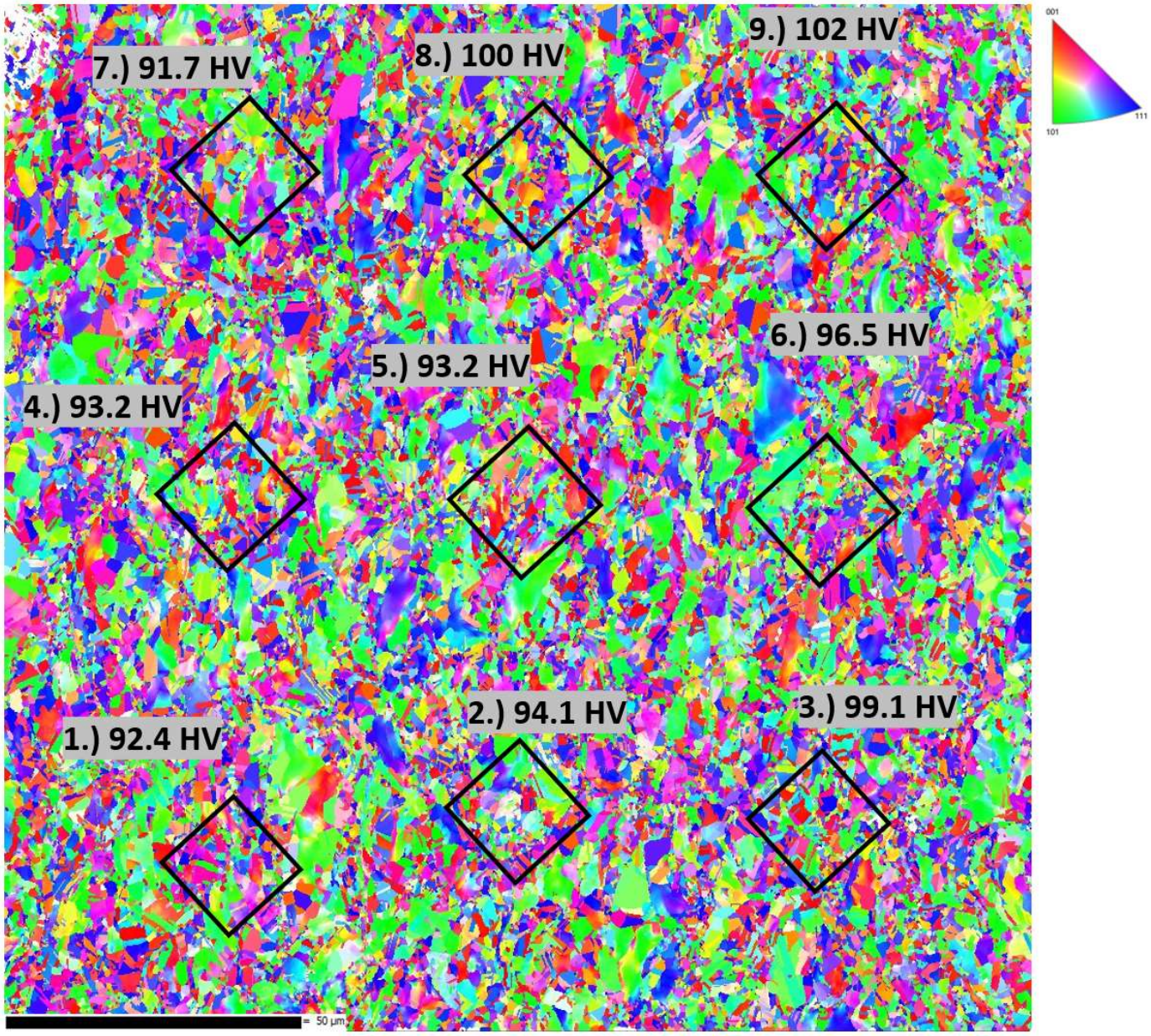


**Figure 52 Inverse pole figure in Z-direction of CS transverse direction specimen with indent outlines of 3x3 array and their associated Vickers microhardness values.**

## 4.6 Low Magnification Images and Indent Arrays

Figures 53 and 54 are the low magnification 12 indent arrays taken on CS spray and transverse direction specimens respectively. The patterns in the microstructure identified in the individual indent images as well as the EBSD images allowed for inferences to be made about the underlying microstructure captured within each indent outline. The characterization process at high magnification supports the validity of the Image-J analysis performed on these micrographs. A percentage for area fraction was also assigned to each indent and the associated data for these arrays are listed in Tables 9 and 10. When visually comparing the highest value of microhardness (Indent #9) to the lowest value (Indent #7) the trend is further established. Indent #7 contains mostly LDR's with nearly half the region encompassing only a few grains. Indent #9 resulted in a value of 89.4 HV and shows significant evidence of HDR.

The CS transverse direction low magnification array shown in Figure 54 resulted in less variability in microhardness than the spray direction with a standard deviation of 2.9 and 4.01. However, a correlation between hardness and grain size was less apparent in the transverse direction since most indent regions contained a variety grain sizes with no clear outliers. This is supported by the previous characterization at lower magnification.

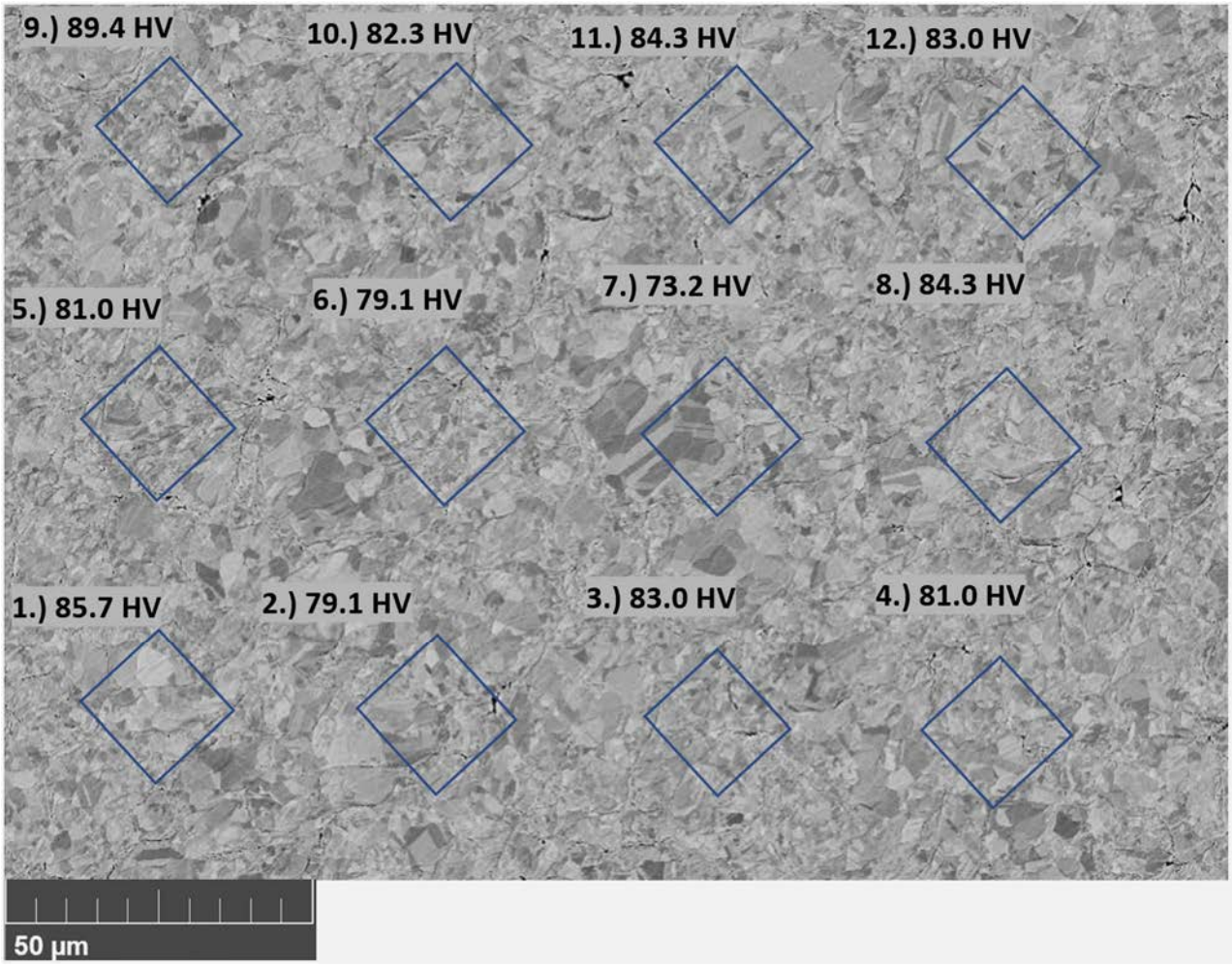


**Figure 53 BSE Micrograph of 12 microhardness indent outlines for CS spray direction specimen. Each outline is numbered with their associated microhardness value.**

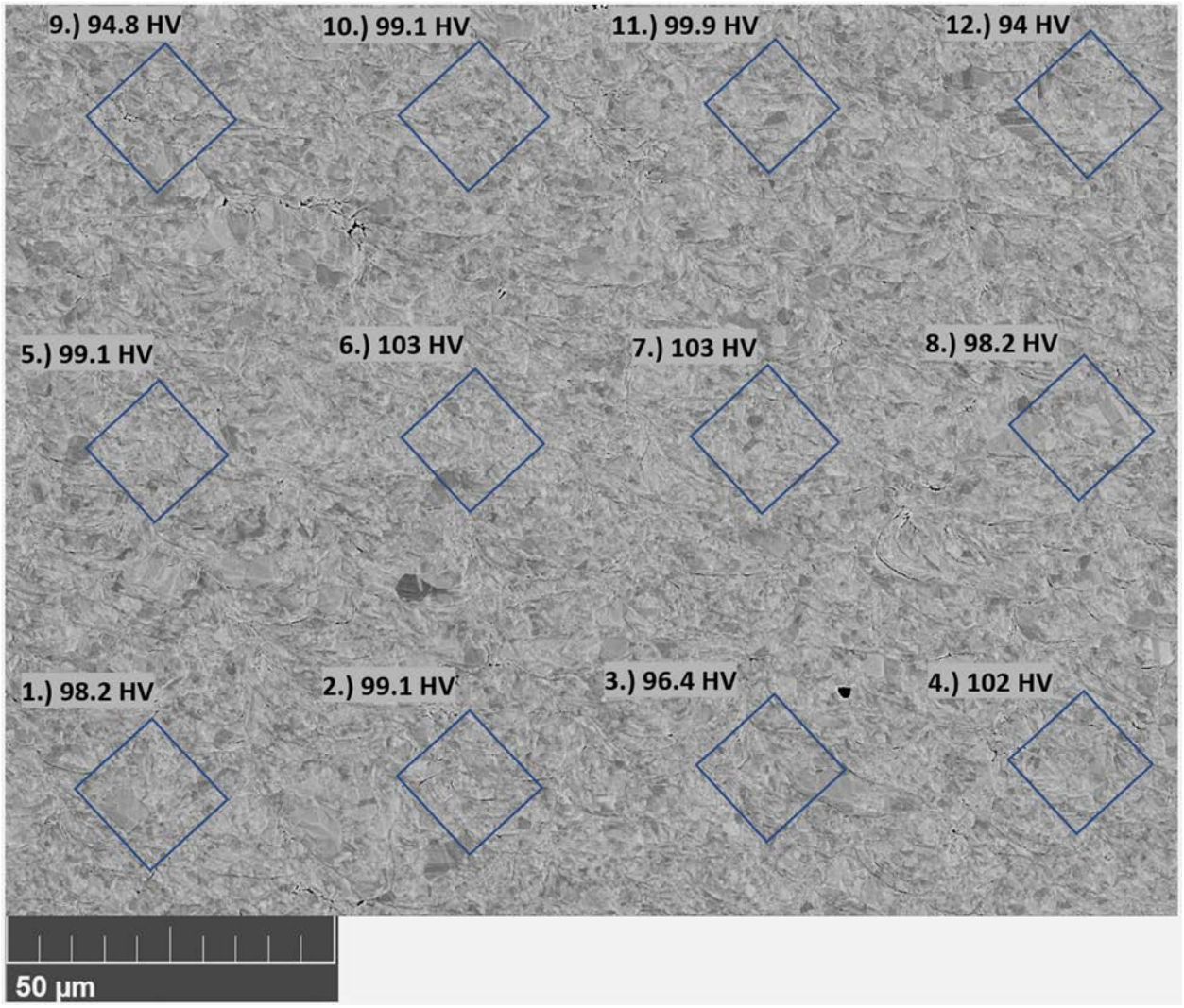


**Figure 54 BSE Micrograph of 12 microhardness indent outlines for CS transverse direction specimen. Each outline is numbered with their associated microhardness value.**

## 4.7 Hardness and Area Fraction Results

The following are microhardness values and statistical data associated with the various arrays collected for the experiment. The data is shown in separate tables first, then combined into graphs shown in Figure 55. All indentation data collected during the experiment is shown in the appendix which includes values conducted on CR material that were not used for this statistical analysis due to errors with the indentation or polishing process. The fraction of HDR in each indent mark region was measured using Image-J and reported as percentage of the entire indent region. The information gathered from the high magnification images was used as a predictive tool to assess the deformation captured within the larger arrays due to the low detail in the large array image. The pressed powder indent images were not measured for area fraction results as the grain size was uniform, and the hardness values showed the lowest variability in the data. The indent number for each table corresponds to the number on each respective figure.

## 4.7.1 Associated Microhardness Data for High Magnification Images

The data in Tables 4-6 are microhardness values associated with the high magnification micrographs.

**Table 4 Associated Vickers microhardness data for CS Spray direction high magnification images.**

| Indent Number | Vickers Hardness Value | Area Fraction % | Statistics | |
|---|---|---|---|---|
| **1** | 82.3 | 4.39 | **Average** | 82.8 |
| **2** | 78.5 | 2.46 | | |
| **3** | 83 | 5.48 | **High** | 90.1 |
| **4** | 78.5 | 2.05 | | |
| **5** | 87.9 | 6.13 | **Low** | 78.5 |
| **6** | 82.3 | 4.91 | | |
| **7** | 80.4 | 3.68 | **Standard Deviation** | 3.77 |
| **8** | 90.1 | 7.46 | | |
| **9** | 81 | 3.41 | **Variation Coefficient** | 4.55 |
| **10** | 84.3 | 5.56 | | |

**Table 5 Associated Vickers microhardness data for CS Transverse direction high magnification images.**

| Indent Number | Vickers Hardness Value | Area Fraction % | Statistics | |
|---|---|---|---|---|
| **1** | 103 | 8.46 | **Average** | 102.4 |
| **2** | 110 | 7.30 | | |
| **3** | 105 | 8.12 | **High** | 110 |
| **4** | 100 | 5.13 | | |
| **5** | 108 | 9.94 | **Low** | 96.5 |
| **6** | 104 | 10.98 | | |
| **7** | 102 | 4.47 | **Standard Deviation** | 4.50 |
| **8** | 97.4 | 6.56 | | |
| **9** | 96.5 | 6.57 | **Variation Coefficient** | 4.40 |
| **10** | 98.2 | 4.92 | | |

**Table 6 Associated Vickers microhardness data for Pressed powder high magnification images.**

| Indent Number | Vickers Hardness Value | Statistics | |
|---|---|---|---|
| **1** | 45.1 | **Average** | 46.5 |
| **2** | 47.9 | | |
| **3** | 47.6 | **High** | 47.9 |
| **4** | 47 | | |
| **5** | 44.8 | **Low** | 45.1 |
| **6** | 47 | | |
| **7** | 46.2 | **Standard Deviation** | 1.12 |
| **8** | 47.9 | | |
| **9** | 45.9 | **Variation Coefficient** | 2.41 |
| **10** | 45.9 | | |

## 4.7.2 Associated Microhardness Data for EBSD Images

Tables 7 and 8 contain the microhardness data associated with the arrays placed on the regions scanned by EBSD.

**Table 7 Associated Vickers microhardness data for CS Spray direction EBSD images.**

| Indent Number | Vickers Hardness Value | Area Fraction % | Statistics | |
|---|---|---|---|---|
| **1** | 80.4 | 1.64 | **Average** | 86.2 |
| **2** | 91.7 | 7.03 | | |
| **3** | 83 | 4.97 | **High** | 91.7 |
| **4** | 83 | 4.87 | | |
| **5** | 87.9 | 5.58 | **Low** | 80.4 |
| **6** | 90.1 | 6.45 | | |
| **7** | 84.3 | 5.56 | **Standard Deviation** | 3.75 |
| **8** | 88.6 | 6.02 | | |
| **9** | 87.1 | 5.58 | **Variation Coefficient** | 4.35 |

**Table 8 Associated Vickers microhardness data for CS Transverse direction EBSD images.**

| Indent Number Figure | Vickers Hardness Value | Area Fraction % | Statistics | |
|---|---|---|---|---|
| **1** | 94.2 | 4.87 | **Average** | 96.0 |
| **2** | 94.1 | 4.12 | | |
| **3** | 99.1 | 4.83 | **High** | 102 |
| **4** | 93.2 | 4.87 | | |
| **5** | 93.2 | 6.40 | **Low** | 91.7 |
| **6** | 96.5 | 7.77 | | |
| **7** | 91.7 | 4.79 | **Standard Deviation** | 3.59 |
| **8** | 100 | 5.11 | | |
| **9** | 102 | 4.44 | **Variation Coefficient** | 3.74 |

## 4.7.3 Associated Microhardness Data for Low Magnification Images

Tables 9 and 10 are the microhardness data associated with 4x3 indent arrays assessed with low magnification micrographs.

**Table 9 Associated Vickers microhardness data for CS Spray direction low magnification images.**

| Indent Number | Vickers Hardness Value | % HDR | Statistics | |
|---|---|---|---|---|
| **1** | 85.7 | 5.42 | **Average** | 82.11 |
| **2** | 79.1 | 2.20 | | |
| **3** | 83 | 3.80 | **High** | 89.4 |
| **4** | 81 | 3.80 | | |
| **5** | 81 | 4.14 | **Low** | 73.2 |
| **6** | 79.1 | 3.18 | | |
| **7** | 73.2 | 1.33 | **Standard Deviation** | 4.01 |
| **8** | 84.3 | 4.88 | | |
| **9** | 89.4 | 6.43 | **Variation Coefficient** | 4.89 |
| **10** | 82.3 | 4.35 | | |
| **11** | 84.3 | 5.78 | | |
| **12** | 83 | 4.14 | | |

**Table 10 Associated Vickers microhardness data for CS Transverse direction low magnification images.**

| Indent Number | Vickers Hardness Value | % HDR | Statistics | |
|---|---|---|---|---|
| **1** | 98.2 | 4.56 | **Average** | 98.9 |
| **2** | 99.1 | 4.88 | | |
| **3** | 96.4 | 6.72 | **High** | 103 |
| **4** | 102 | 7.65 | | |
| **5** | 99.1 | 5.69 | **Low** | 94 |
| **6** | 103 | 7.39 | | |
| **7** | 103 | 9.00 | **Standard Deviation** | 2.90 |
| **8** | 98.2 | 7.81 | | |
| **9** | 94.8 | 6.76 | **Variation Coefficient** | 2.93 |
| **10** | 99.1 | 6.90 | | |
| **11** | 99.9 | 5.35 | | |
| **12** | 94 | 5.00 | | |

## 4.7.4 Combined Microhardness Data.

Table 11 shows the overall microhardness data for all indentation conducted for the study with associated statistics. The average for CS spray direction, CS transverse direction, and pressed powder, were 83.54, 98.9, and 46.53 respectively. The data demonstrates the spray direction samples overall showed the most variability in microhardness as well as overall lower values than its transverse direction counterpart. Additionally, the powder pressed specimen demonstrated the least variability and lowest microhardness overall.

**Table 11 Microhardness data totals and statistics.**

| Specimen Type | Average | High | Low | Standard Deviation | Variance |
|---|---|---|---|---|---|
| Cold Spray Spray-Direction | 83.54 | 91.7 | 78.5 | 4.13 | 4.95 |
| Cold Spray Transverse-Direction | 98.9 | 110 | 93.2 | 2.90 | 2.93 |
| Pressed Powder | 46.53 | 47 | 45.1 | 1.12 | 2.41 |

Graphed in Figure 55 are the comparisons between Vickers Microhardness and the area fraction of HDR's encapsulated within each indent mark. The pressed powder specimen was not considered for area fraction analysis. Graph (a.) shows all three imaging techniques for the spray direction CS specimen, and Graph (b.) shows the same comparison but for the transverse direction CS specimen. Graph (a.) clearly demonstrates a linear trend with hardness increasing as HDR increases, while graph (b.) does not show any correlation between area fraction of HDR and microhardness.

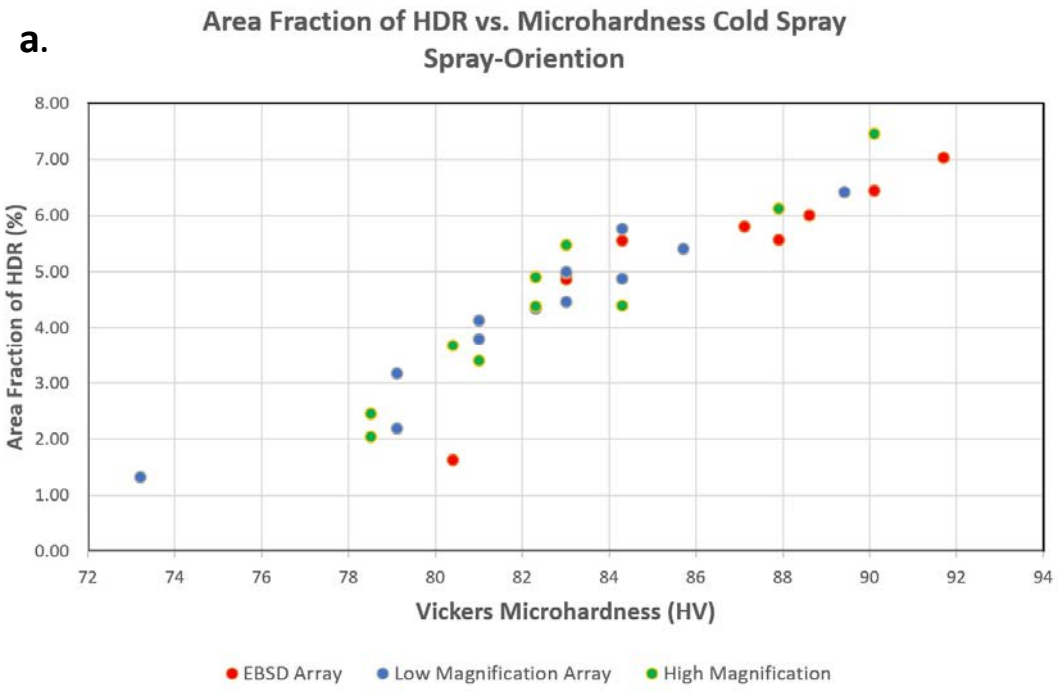


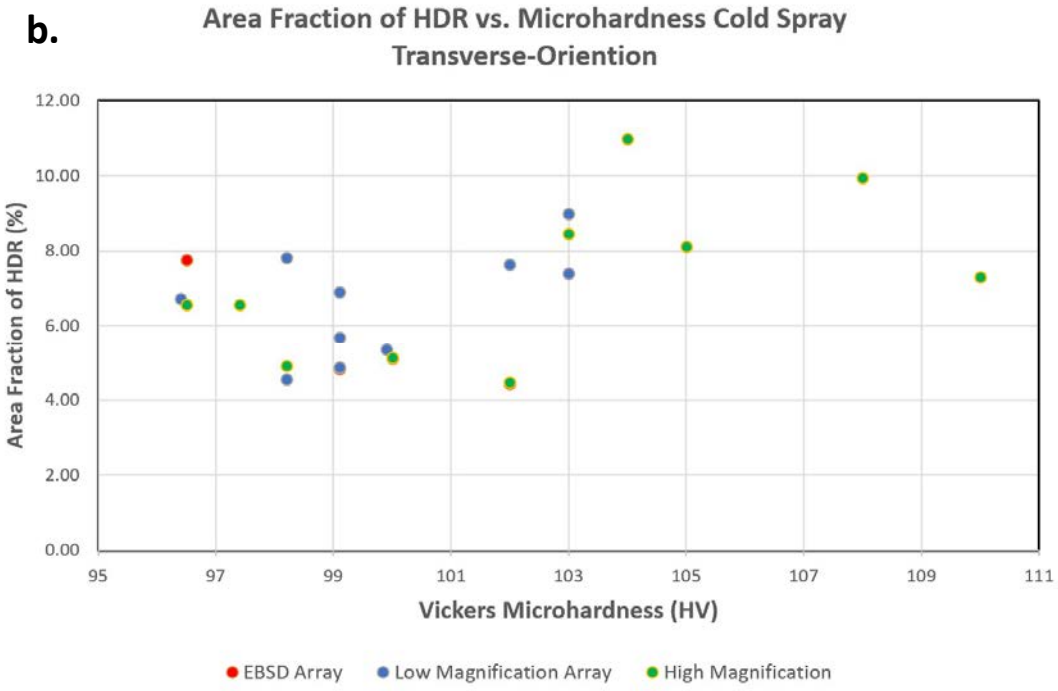


**Figure 55 Graph comparing Vickers microhardness to percentage of high deformation captured within the indent region. (a.) CS Spray Direction. (b.) CS Transverse Direction.**

### 4.7.5 Considering the Volume of an Indent

To understand why the spray direction contains both a higher variability in microhardness as well as lower average microhardness, a visualization of the microstructure depicting the volume captured within in the indent region is helpful. Using the known Vickers indenter angle of 136° and mean indent diagonal width of 22.5 µm, an average depth of 4 µm was calculated. Figure 56 is an illustration of a transverse direction micrograph with the side profile of a potential indent shown. The indent in this case would be placed on the spray direction surface of the material. The arrows indicate the preferential particle stacking that is often exhibited in the transverse direction micrographs, leading to a possible explanation of the lower hardness reported in the spray direction. This particle stacking creates isolated regions of low deformation as the center of the particles exhibit the least grain refinement due to lack of jetting. It also creates isolated regions of high deformation, but these encompass a smaller total area. Indents placed in the spray direction that enter the center of particles will likely encounter more center particle regions below and thus a lower volume fraction of HDR. Indents placed in between stacked particle boundaries may continue to encounter some level of HDR as the indent penetrates further but retain a majority of LDR in the volume of the indent region lending to the lower microhardness in the spray direction. This explanation is further reinforced by considering the reverse of this scenario. The transverse direction indentation data exhibited lower variability and higher hardness overall. This data is supported by the transverse direction surface containing more regions of HDR as well as no effect from the shown preferential particle stacking.

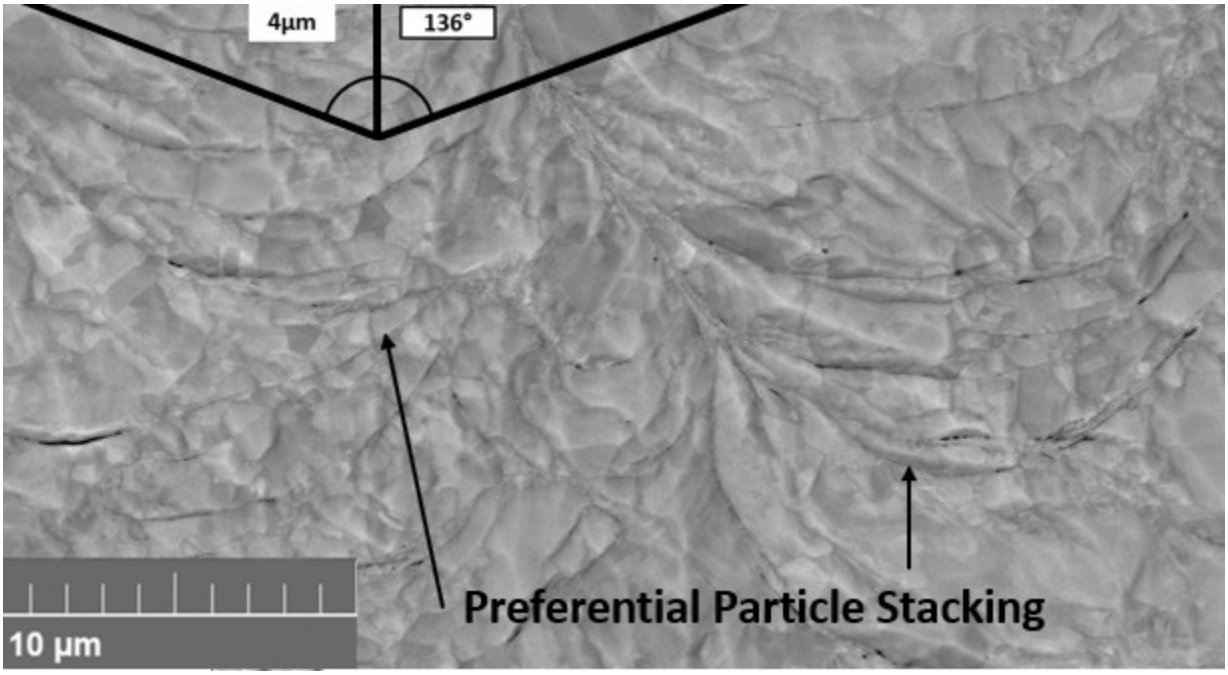


**Figure 56 Transverse direction CS BSE micrograph with cross sectional visualization of potential indent placed on the spray direction surface. Arrows indicate the preferential powder particle stacking seen in the transverse direction sample.**

## 4.8 Scanning Probe Microscopy

Figures 57 and 58 show deflection images generated in tapping for CS Spray orientation and CS Transverse orientation samples respectively. Both figures also show an isometric view of the sample surface better illustrating the topography of the samples. The largest height variance across the length of the spray sample was 2.26 µm and the largest for the CS transverse direction specimen was 1.44 µm. It is clear however, the height difference across the sample is mainly due to the sample not lying flat on the SPM disk rather than a feature of the microstructure. This is clear because the color gradient – which indicates the difference in

height – changes linearly over the surface with one corner clearly higher than the other. Despite the major height change occurring due to the leveling issue, these images provide good insight into the topography of the CS structure. The topography in the transverse specimen is especially apparent in the height comparison image on the bottom image of Figure 58. A "wave" like morphology can be seen which may be indicative of preferential milling during the ion-mill polishing step. Particle boundaries with higher levels of porosity or lack of adhesion may mill faster than individual grains creating this wave pattern. This preferential milling was also seen during an attempt at tomography generation using an SEM-FIB. Although these instruments do not use the same type of beam for milling (Gallium vs Argon) a similar outcome may have occurred.

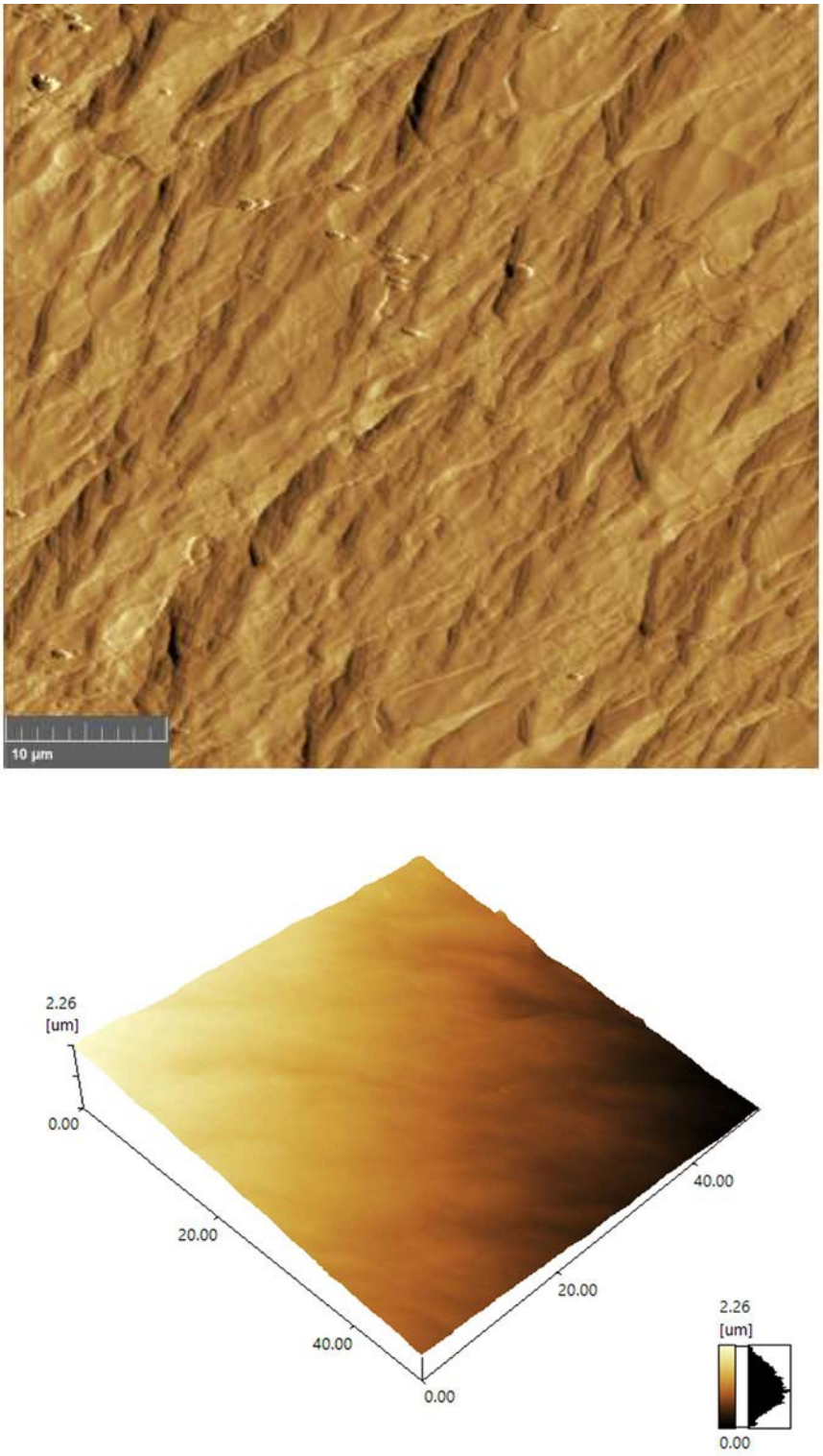


**Figure 57 (Top) CS Spray direction deflection image in tapping mode. (Bottom) 3D view of spray direction sample in tapping mode showing sample height and topography.**

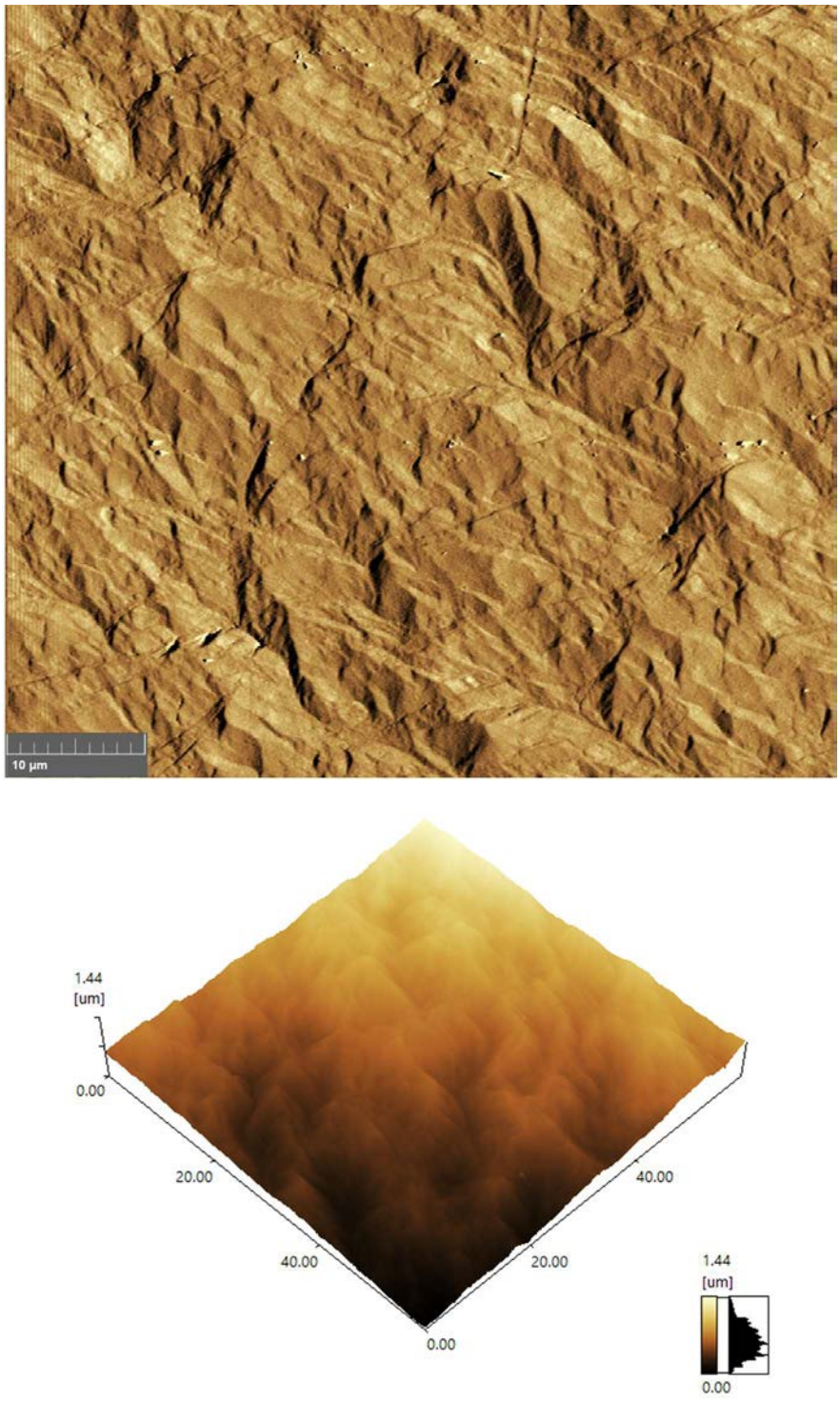


**Figure 58 (Top) CS Transverse direction deflection image in tapping mode. (Bottom) 3D view of transverse direction sample in tapping mode showing sample height and topography.**

### 4.8.1 Nano 3D Mechanical Mapping

The reported values from the SPM mapping for young's modulus were significantly lower (-10^3) than a typical value reported for copper. There were several attempts to locate the source of the discrepancy by manipulating the sensitivity, approach and release points, tip radius, cantilever spring constant, calculation model, as well as others. For this reason, these data were only used as a relative comparison since both transverse and spray direction CS specimens generated values of similar magnitude. Figures 59 and 60 show deflection images with highlighted mapping window and nanomechanical map for LDR and HDR respectively on a CS Spray direction sample. The nano map plots young's modulus within the outlined region and a lighter color indicates a higher value. Both nanomechanical maps were taken with 64 points over a 2x2 µm region with the LDR capturing a single grain, and HDR capturing many highly deformed grains. Despite the LDR in Figure 59 reporting a higher individual value on the legend, the overall image pattern in Figure 60 is lighter indicating higher average young's modulus over the captured area. Figures 61 and 62 show the same type of comparison as the spray direction with HDR and LDR areas of interest captured in 64-point 2x2 µm windows, but on the CS transverse direction specimen. The results were less definitive for the transverse direction specimen which is supported by the weak correlation from the indentation experiments. The LDR region was mostly mixed values with an average value somewhere in the middle of the range. However, the HDR region reported a maximum value nearly double the LDR region but with the remaining portion of the map falling on the lower end of the range.

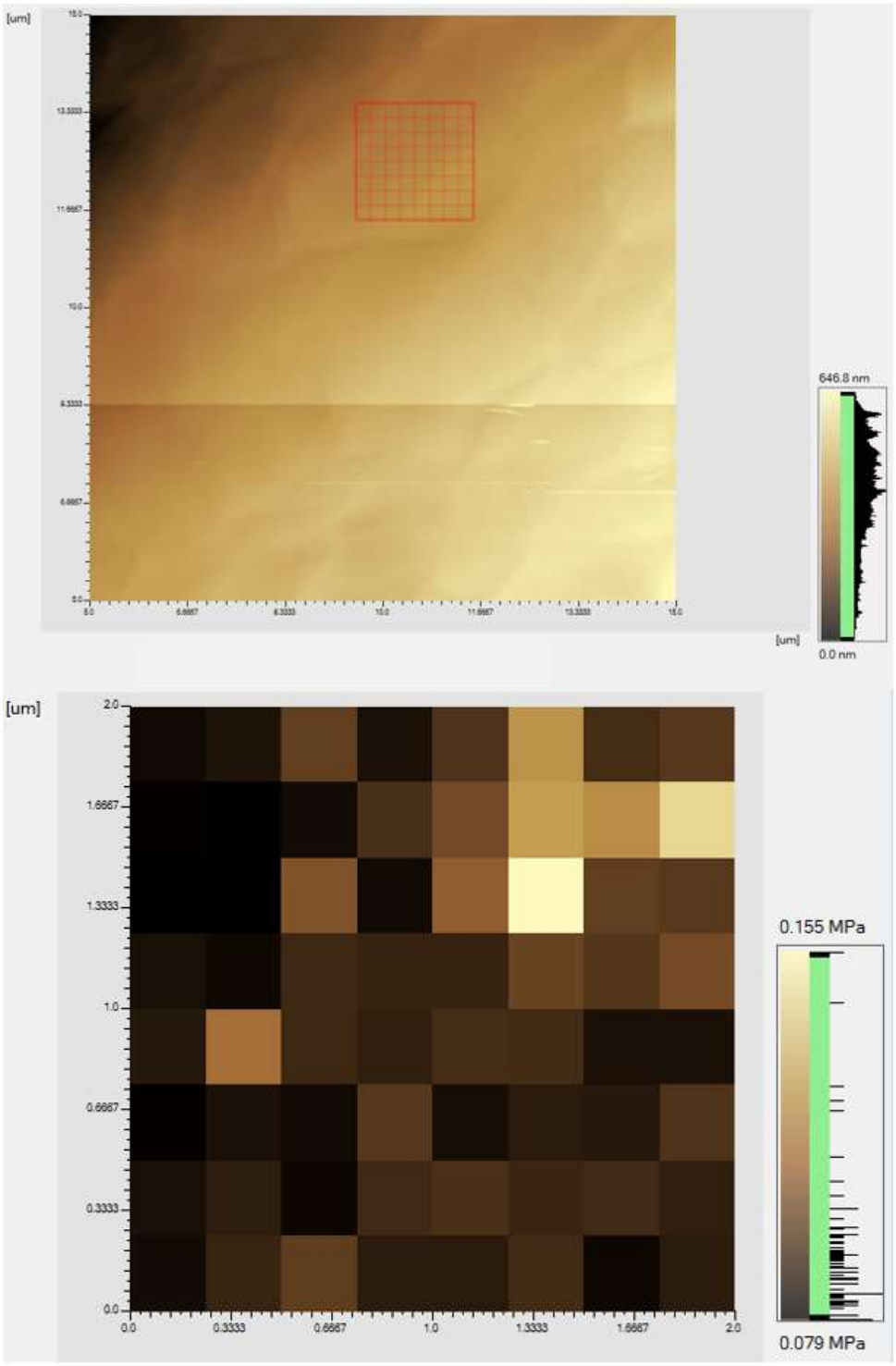


**Figure 59 (Top) Deflection image taken in contact mode with nano mapping window highlighted over single grain - Spray direction CS specimen. (Bottom) 3D nano mechanical map for grain in highlighted window.**

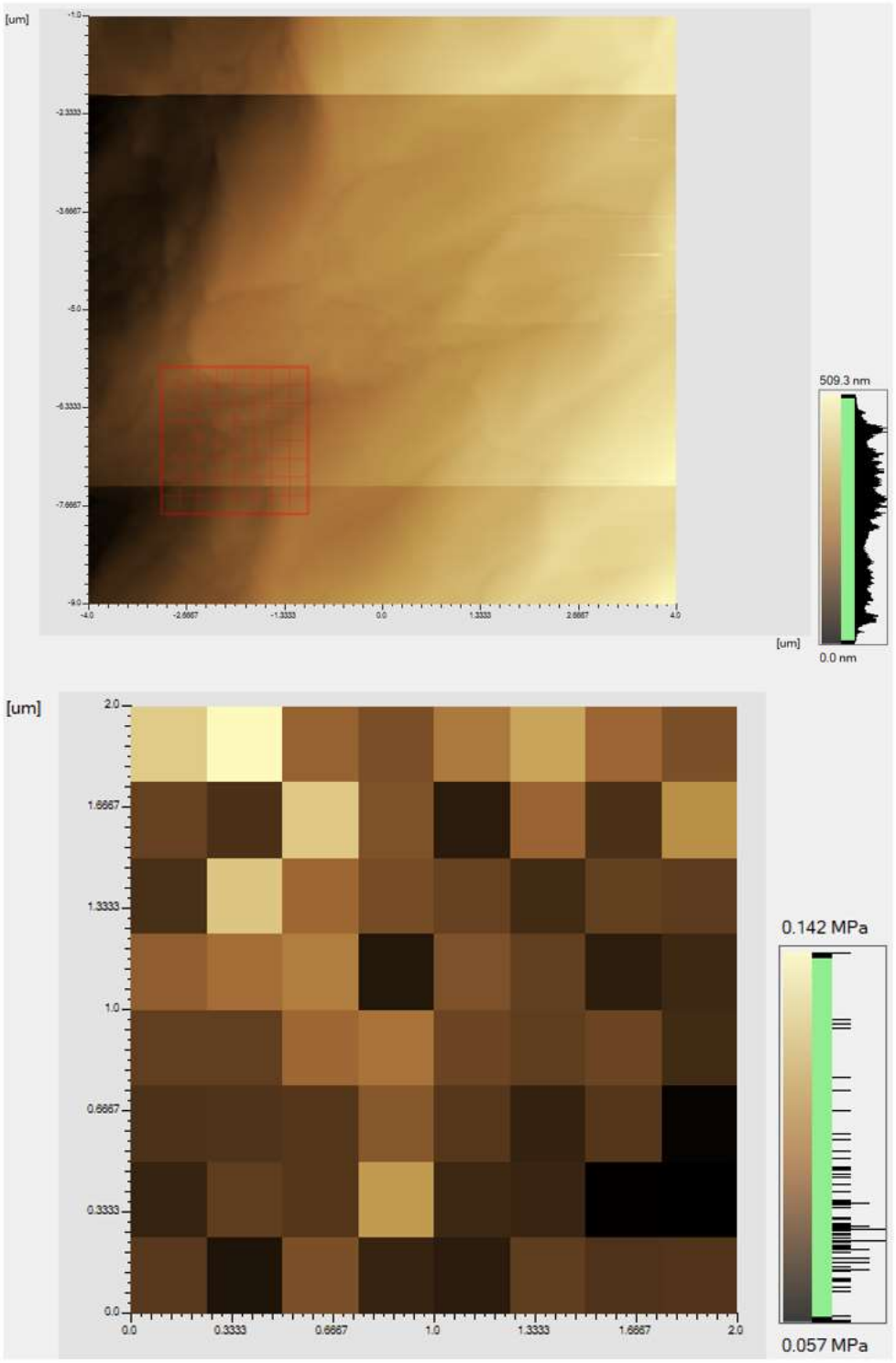


**Figure 60 (Top) Deflection image taken in contact mode with nano mapping window highlighted over many small grains - Spray direction CS specimen. (Bottom) 3D nano mechanical map for highly deformed grains in highlighted window.**

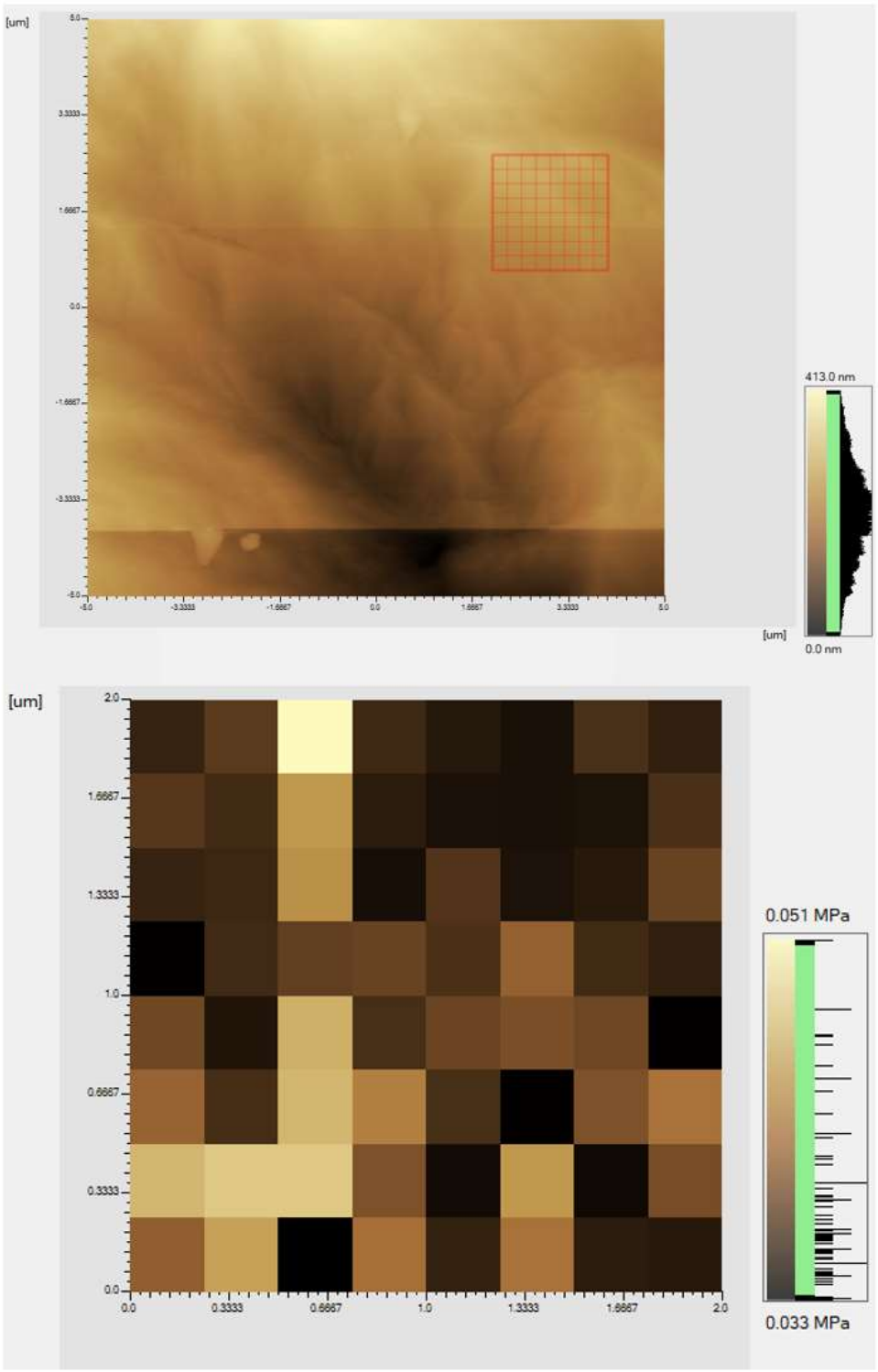


**Figure 61 (Top) Deflection image taken in contact mode with nano mapping window highlighted over single grain - Transverse direction CS specimen. (Bottom) 3D nano mechanical map for grain in highlighted window.**

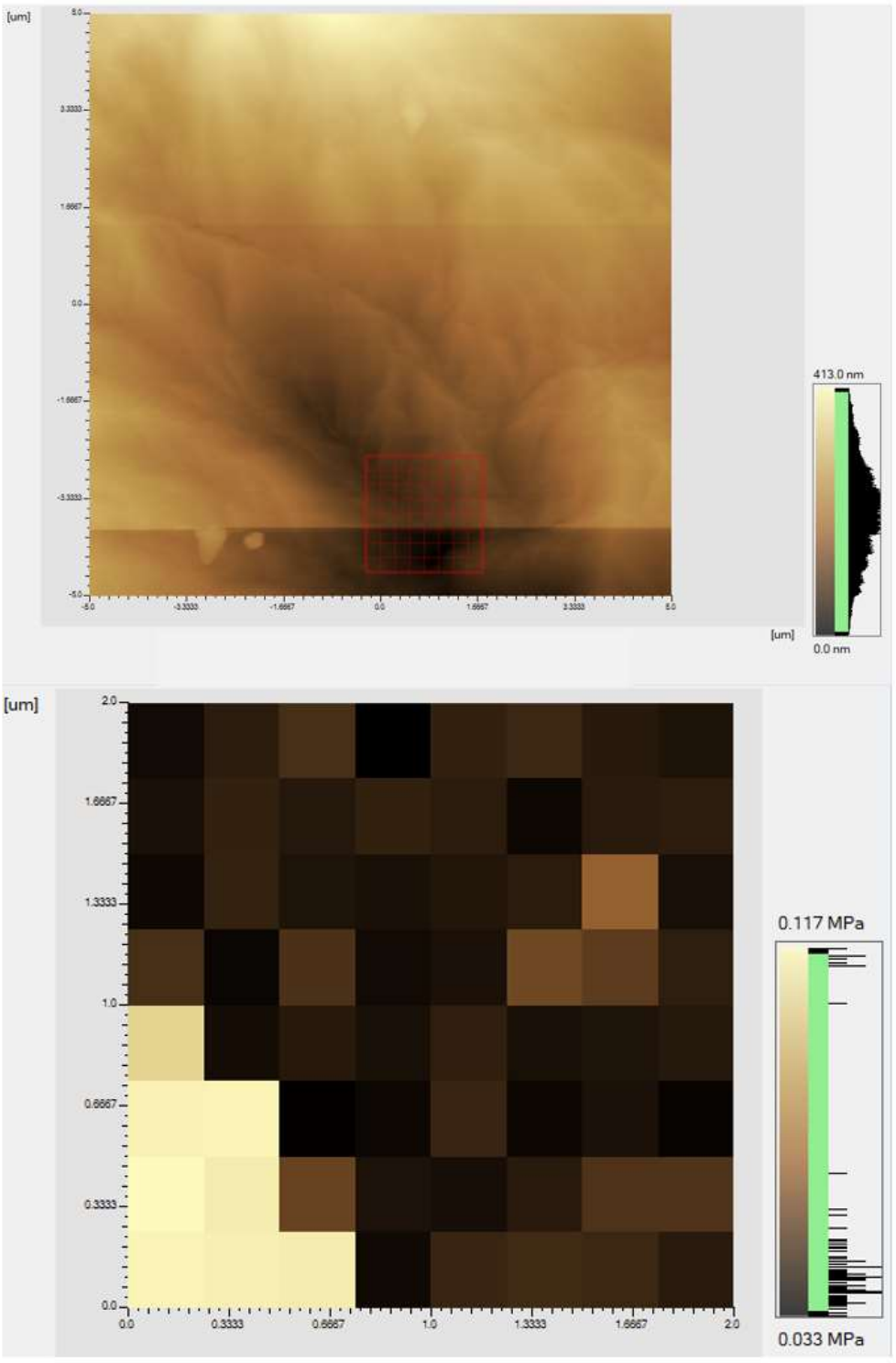


**Figure 62 (Top) Deflection image taken in contact mode with nano mapping window highlighted over many small grains - Transverse direction CS specimen. (Bottom) 3D nano mechanical map for highly deformed grains in highlighted window.**

# Chapter 5: Conclusions and Future Works

Before drawing conclusions on the microstructural effects on microhardness it should be noted that the possibility of heating during long term ion milling may have affected the microhardness. The effects of heating from ion milling may have resulted in minor amounts of recrystallization but should not have affected grain sizes and therefore should not have skewed the effect of grain size which is the major focus of this study.

Overall, a partial correlation has been established between grain size and microhardness of CS copper. The increase in hardness with a decrease in grain size was more apparent in the sprayed directions of the materials. This difference could stem from issues associated with the sample preparation process or it may be an intrinsic property of CS material. The CS process produces inhomogeneous structures with high variability in microhardness, however the transverse direction exhibits less variability than the spray direction. This result correlates to the difference in microstructure observed in these two orientations. When measured in the spray direction, the volume captured within the indents may be sampling several LDR's of stacked particles beneath the surface lending to its lower hardness. Further research into this comparison would prove valuable in validating microhardness as tool for evaluating macroscopic properties for engineering applications.

Correlating between SPM and SEM imaging also proved too difficult to establish an efficient and repeatable enough procedure. An attempt was made to first image samples on the SPM in contact mode collecting nanomechanical maps in a region marked with fiduciary

indicators. The samples were then transferred to the SEM with the goal of imaging the same region as well as collecting an EBSD scan then indented. This comparison between SPM, EBSD, and Microhardness would have ideally provided a more complete correlative data set for each individual indent.

With several methodology questions answered during the experimentation process a new understanding for multi-instrument correlation for CS material has been established. With the development of new equipment producing significantly (10x) faster EBSD scans a method previously impossible may now be performed. The individual indent images with a 60 µm FOV proved the most superior in terms of accurate area fraction assessment. Using updated SEM equipment, individual indent regions could potentially be scanned using EBSD stitching to generate a region where a full array could be indented in a single HMV-G session, but each indent would have its own 60 µm FOV pole figure for grain identification and assessment. Additionally, Aztec post-processing software allows for accurate grain size and distribution measurement given a small enough FOV is selected. In future works it would be valuable to refine the ion milling procedure to avoid heating and the reduction in microhardness discussed previously. Additionally, a continued methodology assessment to alleviate sample preparation and data generation errors would prove most valuable before establishing a clear experimentation procedure for this multi-instrument correlative method.

# References


[1] B. AlMangour, "Fundamentals of cold spray processing: Evolution and future perspectives," in *Cold-Spray Coatings: Recent Trends and Future Perspectives*, P. Cavaliere, Ed. 2018, Available: https://doi.org/10.1007/978-3-319-67183-3_1. DOI: 10.1007/978-3-319-67183-3_1.

[2] S. Yin *et al*, "Microstructure and mechanical anisotropy of additively manufactured cold spray copper deposits," *Materials Science and Engineering: A,* vol. 734, pp. 67-76, 2018. Available: https://www.sciencedirect.com/science/article/pii/S0921509318310311. DOI: https://doi.org/10.1016/j.msea.2018.07.096.

[3] C. A. Widener, O. C. Ozdemir and M. Carter, "Structural repair using cold spray technology for enhanced sustainability of high value assets," *Procedia Manufacturing,* vol. 21, pp. 361-368, 2018. Available: https://dx.doi.org/10.1016/j.promfg.2018.02.132. DOI: 10.1016/j.promfg.2018.02.132.

[4] P. Poza and M. Á Garrido-Maneiro, "Cold-sprayed coatings: Microstructure, mechanical properties, and wear behaviour," *Progress in Materials Science,* vol. 123, pp. 100839, 2022. Available: https://www.sciencedirect.com/science/article/pii/S0079642521000633. DOI: https://doi.org/10.1016/j.pmatsci.2021.100839.

[5] V. K. Champagne and D. J. Helfritch, "Mainstreaming cold spray – push for applications," *Null,* vol. 30, *(6),* pp. 396-403, 2014. Available: https://doi.org/10.1179/1743294414Y.0000000277. DOI: 10.1179/1743294414Y.0000000277.

[6] W. Sun *et al*, "Current Implementation Status of Cold Spray Technology: A Short Review," *J. Therm. Spray Technol.,* vol. 31, *(4),* pp. 848-865, 2022. Available: https://doi.org/10.1007/s11666-022-01382-4. DOI: 10.1007/s11666-022-01382-4.

[7] G. Benenati and R. Lupoi, "Development of a Deposition Strategy in Cold Spray for Additive Manufacturing to Minimize Residual Stresses," *Procedia CIRP; 5th CIRP Global Web Conference - Research and Innovation for Future Production (CIRPe 2016),* vol. 55, pp. 101-108, 2016. Available: https://www.sciencedirect.com/science/article/pii/S2212827116309313. DOI: 10.1016/j.procir.2016.08.042.

[8] A. Sova *et al*, "Potential of cold gas dynamic spray as additive manufacturing technology," *Int J Adv Manuf Technol,* vol. 69, *(9-12),* pp. 2269-2278, 2013. Available: https://link.springer.com/article/10.1007/s00170-013-5166-8. DOI: 10.1007/s00170-013-5166-8.

[9] R. N. Raoelison, C. Verdy and H. Liao, "Cold gas dynamic spray additive manufacturing today: Deposit possibilities, technological solutions and viable applications," *Mater Des,* vol. 133, pp. 266-287, 2017. Available: https://www.sciencedirect.com/science/article/pii/S026412751730744X. DOI: 10.1016/j.matdes.2017.07.067.

[10] W. Li *et al*, "Solid-state additive manufacturing and repairing by cold spraying: A review," *Journal of Materials Science & Technology,* vol. 34, *(3),* pp. 440-457, 2018. Available: https://dx.doi.org/10.1016/j.jmst.2017.09.015. DOI: 10.1016/j.jmst.2017.09.015.

[11] S. Yin *et al*, "Cold spray additive manufacturing and repair: Fundamentals and applications," *Additive Manufacturing,* vol. 21, pp. 628-650, 2018. Available: https://www.sciencedirect.com/science/article/pii/S2214860417302993. DOI: 10.1016/j.addma.2018.04.017.

[12] M. Ashokkumar *et al*, "An overview of cold spray coating in additive manufacturing, component repairing and other engineering applications," vol. 31, *(1),* pp. 514-534, 2022. Available: https://doi.org/10.1515/jmbm-2022-0056. DOI: 10.1515/jmbm-2022-0056.

[13] R. Sinclair-Adamson *et al*, "Residual Stress Distributions in Cold-Sprayed Copper 3D-Printed Parts," *J. Therm. Spray Technol.,* vol. 29, *(6),* pp. 1525-1537, 2020. Available: https://doi.org/10.1007/s11666-020-01040-7. DOI: 10.1007/s11666-020-01040-7.

[14] S. Kumar, "Influence of processing conditions on the mechanical, tribological and fatigue performance of cold spray coating: a review," *Surface Engineering,* vol. 38, *(4),* pp. 324-365, 2022. Available: https://doi.org/10.1080/02670844.2022.2073424. DOI: 10.1080/02670844.2022.2073424.

[15] M. Walker, "Microstructure and bonding mechanisms in cold spray coatings," *Materials Science and Technology,* vol. 34, *(17),* pp. 2057-2077, 2018. Available: https://www.tandfonline.com/doi/abs/10.1080/02670836.2018.1475444. DOI: 10.1080/02670836.2018.1475444.

[16] S. Singh *et al*, "Influence of Cold Spray Parameters on Bonding Mechanisms: A Review," *Metals (Basel ),* vol. 11, *(12),* pp. 2016, 2021. Available: https://search.proquest.com/docview/2612813392. DOI: 10.3390/met11122016.

[17] T. Stoltenhoff, H. Kreye and H. J. Richter, "An analysis of the cold spray process and its coatings," *J. Therm. Spray Technol.,* vol. 11, *(4),* pp. 542-550, 2002. Available: https://doi.org/10.1361/105996302770348682. DOI: 10.1361/105996302770348682.

[18] F. Gärtner *et al*, "The cold spray process and its potential for industrial applications," *J. Therm. Spray Technol.,* vol. 15, *(2),* pp. 223-232, 2006. Available: https://doi.org/10.1361/105996306X108110. DOI: 10.1361/105996306X108110.

[19] K. Sundberg *et al*, "Finite Element Modeling of Single-Particle Impacts for the Optimization of Antimicrobial Copper Cold Spray Coatings," *J. Therm. Spray Technol.,* vol. 29, *(8),* pp. 1847-1862, 2020. Available: https://doi.org/10.1007/s11666-020-01093-8. DOI: 10.1007/s11666-020-01093-8.

[20] H. Assadi *et al*, "Bonding mechanism in cold gas spraying," *Acta Materialia,* vol. 51, *(15),* pp. 4379-4394, 2003. Available: https://www.sciencedirect.com/science/article/pii/S135964540300274X. DOI: https://doi.org/10.1016/S1359-6454(03)00274-X.

[21] A. Papyrin, *Cold Spray Technology.* (1. ed. ed.) Amsterdam [u.a.]: Elsevier, 2007.

[22] P. C. King, S. H. Zahiri and M. Jahedi, "Focused ion beam micro-dissection of cold-sprayed particles," *Acta Materialia,* vol. 56, *(19),* pp. 5617-5626, 2008. Available: https://www.sciencedirect.com/science/article/pii/S1359645408005338. DOI: 10.1016/j.actamat.2008.07.034.

[23] B. Yu *et al*, "Microstructural and bulk properties evolution of cold-sprayed copper coatings after low temperature annealing," *Materialia,* vol. 7, pp. 100356, 2019. Available: https://dx.doi.org/10.1016/j.mtla.2019.100356. DOI: 10.1016/j.mtla.2019.100356.

[24] H. Singh, M. Kumar and R. Singh, "An overview of various applications of cold spray coating process," *Materials Today: Proceedings,* vol. 56, pp. 2826-2830, 2022. Available: https://www.sciencedirect.com/science/article/pii/S2214785321066645. DOI: 10.1016/j.matpr.2021.10.160.

[25] V. K. Champagne *et al*, "Applications," in *Modern Cold Spray: Materials, Process, and Applications*, J. Villafuerte, Ed. 2015, Available: https://doi.org/10.1007/978-3-319-16772-5_10. DOI: 10.1007/978-3-319-16772-5_10.

[26] V. Champagne and D. Helfritch, "The unique abilities of cold spray deposition," *International Materials Reviews,* vol. 61, *(7),* pp. 437-455, 2016. Available: https://doi.org/10.1080/09506608.2016.1194948. DOI: 10.1080/09506608.2016.1194948.

[27] T. Liao *et al*, "Multifunctional cold spray coatings for biological and biomedical applications: A review," *Prog Surf Sci,* vol. 97, *(2),* pp. 100654, 2022. Available: https://www.sciencedirect.com/science/article/pii/S0079681622000016. DOI: 10.1016/j.progsurf.2022.100654.

[28] T. Hussain, S. Yue and C. -. Li, "Characteristics of feedstock materials," in *Modern Cold Spray: Materials, Process, and Applications*, J. Villafuerte, Ed. 2015, Available: https://doi.org/10.1007/978-3-319-16772-5_3. DOI: 10.1007/978-3-319-16772-5_3.

[29] V. K. Champagne and D. J. Helfritch, "A demonstration of the antimicrobial effectiveness of various copper surfaces," *J. Biol. Eng.,* vol. 7, *(1),* pp. 8-8, 2013. . DOI: 10.1186/1754-1611-7-8.

[30] R. G. Neo *et al*, "Effect of Spray Distance and Powder Feed Rate on Particle Velocity in Cold Spray Processes," *Metals,* vol. 12, *(1),* 2022. . DOI: 10.3390/met12010075.

[31] K. Sakaki, "7 - the influence of nozzle design in the cold spray process," in *The Cold Spray Materials Deposition Process*Anonymous Elsevier Ltd, 2007, pp. 117-126.

[32] P. King, M. Yandouzi and B. Jodoin, "The physics of cold spray," in *Modern Cold Spray: Materials, Process, and Applications*, J. Villafuerte, Ed. 2015, Available: https://doi.org/10.1007/978-3-319-16772-5_2. DOI: 10.1007/978-3-319-16772-5_2.

[33] C. Borchers *et al*, "Microstructural and macroscopic properties of cold sprayed copper coatings," *J. Appl. Phys.,* vol. 93, *(12),* pp. 10064-10070, 2003. Available: https://doi.org/10.1063/1.1573740. DOI: 10.1063/1.1573740.

[34] N. K. Singh *et al*, "A Modeling Study of Bonding Mechanisms Between Similar and Dissimilar Materials in Cold Spraying on Polymeric Substrates," *J. Therm. Spray Technol.,* vol. 31, *(3),* pp. 508-524, 2022. Available: https://doi.org/10.1007/s11666-022-01348-6. DOI: 10.1007/s11666-022-01348-6.

[35] M. R. Rokni *et al*, "Review of Relationship Between Particle Deformation, Coating Microstructure, and Properties in High-Pressure Cold Spray," *J Therm Spray Tech,* vol. 26, *(6),* pp. 1308-1355, 2017. Available: https://link.springer.com/article/10.1007/s11666-017-0575-0. DOI: 10.1007/s11666-017-0575-0.

[36] T. Schmidt *et al*, "Development of a generalized parameter window for cold spray deposition," *Acta Materialia,* vol. 54, *(3),* pp. 729-742, 2006. Available: https://dx.doi.org/10.1016/j.actamat.2005.10.005. DOI: 10.1016/j.actamat.2005.10.005.

[37] V. Champagne Jr *et al*, "The Effects of Gas and Metal Charcteristics on Sprayed Metal Coatings," *Modell Simul Mater Sci Eng,* vol. 13, pp. 1119, 2005. . DOI: 10.1088/0965-0393/13/7/008.

[38] W. Wong *et al*, "Influence of Helium and Nitrogen Gases on the Properties of Cold Gas Dynamic Sprayed Pure Titanium Coatings," *J. Therm. Spray Technol.,* vol. 20, *(1),* pp. 213-226, 2011. Available: https://doi.org/10.1007/s11666-010-9568-y. DOI: 10.1007/s11666-010-9568-y.

[39] S. Yin *et al*, "Significant influence of carrier gas temperature during the cold spray process," *Surface Engineering,* vol. 30, *(6),* pp. 443-450, 2014. Available: https://www.tandfonline.com/doi/abs/10.1179/1743294414Y.0000000276. DOI: 10.1179/1743294414Y.0000000276.

[40] R. N. Raoelison *et al*, "Cold gas dynamic spray technology: A comprehensive review of processing conditions for various technological developments till to date," *Additive Manufacturing,* vol. 19, pp. 134-159, 2018. Available: https://dx.doi.org/10.1016/j.addma.2017.07.001. DOI: 10.1016/j.addma.2017.07.001.

[41] S. Yin *et al*, "Deposition behavior of thermally softened copper particles in cold spraying," *Acta Materialia,* vol. 61, *(14),* pp. 5105-5118, 2013. Available: https://www.sciencedirect.com/science/article/pii/S1359645413003145. DOI: 10.1016/j.actamat.2013.04.041.

[42] B. C. Sousa *et al*, "Understanding the Antipathogenic Performance of Nanostructured and Conventional Copper Cold Spray Material Consolidations and Coated Surfaces," *Crystals,* vol. 10, *(6),* 2020. . DOI: 10.3390/cryst10060504.

[43] G. Chen *et al*, "A comparative study of Ti-6Al-4V powders for additive manufacturing by gas atomization, plasma rotating electrode process and plasma atomization," *Powder Technol,* vol. 333, pp. 38-46, 2018. Available: https://www.sciencedirect.com/science/article/pii/S0032591018302857. DOI: 10.1016/j.powtec.2018.04.013.

[44] B. Jodoin *et al*, "Effect of particle size, morphology, and hardness on cold gas dynamic sprayed aluminum alloy coatings," *Surface and Coatings Technology,* vol. 201, *(6),* pp. 3422-3429, 2006. Available: https://www.sciencedirect.com/science/article/pii/S025789720600778X. DOI: https://doi.org/10.1016/j.surfcoat.2006.07.232.

[45] K. Roy, S. Kar and R. N. Das, "Chapter 5 - computational chemistry," in *Understanding the Basics of QSAR for Applications in Pharmaceutical Sciences and Risk Assessment*, K. Roy, S. Kar and R. N. Das, Eds. 2015, Available: https://www.sciencedirect.com/science/article/pii/B9780128015056000053. DOI: 10.1016/B978-0-12-801505-6.00005-3.

[46] S. Rahmati *et al*, "Deformation of copper particles upon impact: A molecular dynamics study of cold spray," *Computational Materials Science,* vol. 171, pp. 109219, 2020. Available: https://www.sciencedirect.com/science/article/pii/S092702561930518X. DOI: https://doi.org/10.1016/j.commatsci.2019.109219.

[47] M. Grujicic *et al*, "Adiabatic shear instability based mechanism for particles/substrate bonding in the cold-gas dynamic-spray process," *Mater Des,* vol. 25, *(8),* pp. 681-688, 2004. Available: https://www.sciencedirect.com/science/article/pii/S026130690400069X. DOI: 10.1016/j.matdes.2004.03.008.

[48] A. Moridi *et al*, "Cold spray coating: review of material systems and future perspectives," *Surface Engineering,* vol. 30, *(6),* pp. 369-395, 2014. Available: https://doi.org/10.1179/1743294414Y.0000000270. DOI: 10.1179/1743294414Y.0000000270.

[49] D. R. Askeland and W. J. Wright, *The Science and Engineering of Materials.* (7. edition ed.) 2016.

[50] Y. Ha and A. Kimura, "Effect of Cold Rolling on Recrystallization Behavior of Al-Free and Al-Added 15Cr-ODS Ferritic Steels," *Crystals,* vol. 9, *(3),* 2019. . DOI: 10.3390/cryst9030145.

[51] Z. You *et al*, "Revisiting anisotropy in the tensile and fracture behavior of cold-rolled 316L stainless steel with heterogeneous nano-lamellar structures," *Nano Materials Science,* vol. 2, *(1),* pp. 72-79, 2020. Available: https://www.sciencedirect.com/science/article/pii/S2589965120300039. DOI: https://doi.org/10.1016/j.nanoms.2020.03.001.

[52] S. H. Whang, *Nanostructured Metals and Alloys.* 2011Available: https://ebookcentral.proquest.com/lib/[SITE_ID]/detail.action?docID=1584683.

[53] N. Hansen, "Hall–Petch relation and boundary strengthening," *Scr. Mater.,* vol. 51, *(8),* pp. 801-806, 2004. Available: https://www.sciencedirect.com/science/article/pii/S1359646204003434. DOI: https://doi.org/10.1016/j.scriptamat.2004.06.002.

[54] W. Sun *et al*, "Post-Process Treatments on Supersonic Cold Sprayed Coatings: A Review," *Coatings,* vol. 10, *(2),* pp. 123, 2020. Available: https://explore.openaire.eu/search/publication?articleId=doajarticles::adc1821a8347a0ab2dd940e83e5650b5. DOI: 10.3390/coatings10020123.

[55] Y. Xie *et al*, "Improvement of tensile strength of cold sprayed Fe deposits via in-process powder preheating," *Mater Lett,* vol. 316, pp. 132090, 2022. Available: https://www.sciencedirect.com/science/article/pii/S0167577X22004438. DOI: 10.1016/j.matlet.2022.132090.

[56] J. R. Cahoon, "An improved equation relating hardness to ultimate strength," *Metallurgical and Materials Transactions B,* vol. 3, *(11),* pp. 3040, 1972. Available: https://doi.org/10.1007/BF02652880. DOI: 10.1007/BF02652880.

[57] R. E. Smallman and A. H. W. Ngan, "Chapter 5 - characterization and analysis," in *Modern Physical Metallurgy (Eighth Edition)*, R. E. Smallman and A. H. W. Ngan, Eds. 2014, Available: https://www.sciencedirect.com/science/article/pii/B9780080982045000055. DOI: https://doi.org/10.1016/B978-0-08-098204-5.00005-5.

[58] E. Broitman, "Indentation Hardness Measurements at Macro-, Micro-, and Nanoscale: A Critical Overview," *Tribology Letters,* vol. 65, *(1),* pp. 23, 2016. Available: https://doi.org/10.1007/s11249-016-0805-5. DOI: 10.1007/s11249-016-0805-5.

[59] P. D. Eason, "A Structure Property Processing Comparison of Cold rolled PM Copper and Cold Gas Dynamically Sprayed Copper," *Journal of Powder Metallurgy & Mining,* vol. 1, *(1),* 2012. . DOI: 10.4172/2168-9806.1000101.

[60] A. J. Wilkinson and T. B. Britton, "Strains, planes, and EBSD in materials science," *Materials Today,* vol. 15, *(9),* pp. 366-376, 2012. Available: https://www.sciencedirect.com/science/article/pii/S1369702112701633. DOI: 10.1016/S1369-7021(12)70163-3.

[61] R. García and R. Pérez, "Dynamic atomic force microscopy methods," *Surface Science Reports,* vol. 47, *(6),* pp. 197-301, 2002. Available: https://www.sciencedirect.com/science/article/pii/S0167572902000778. DOI: https://doi.org/10.1016/S0167-5729(02)00077-8.

[62] S. K. Sharma, *Handbook of Materials Characterization.* 2018Available: http://hdl.handle.net/2078/ebook:119622. DOI: 10.1007/978-3-319-92955-2.

[63] Y. Leng. (). *Materials characterization : introduction to microscopic and spectroscopic methods*. Available: https://doi.org/10.1002/9783527670772.

# Appendix

## A.1.0 Additional Indentation Images

The following are all the indentation images with the underlying microstructure and their corresponding post-indentation image taken for the study.

### A.1.0.1 Spray Direction Cold Spray High Magnification Images

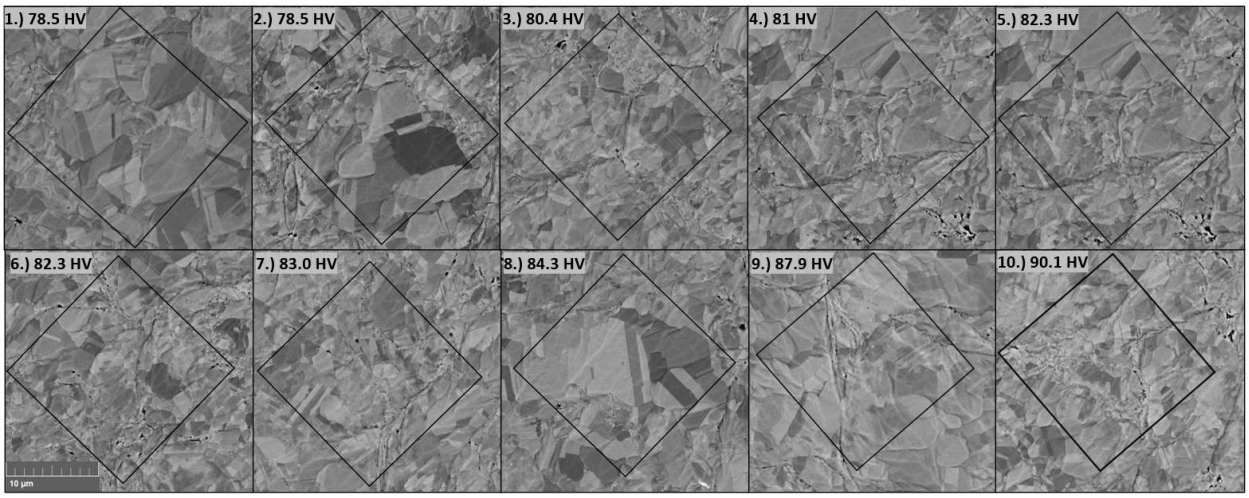


**Figure 63 High Magnification CS pre-indentation images in spray direction with associated microhardness values (BSE).**

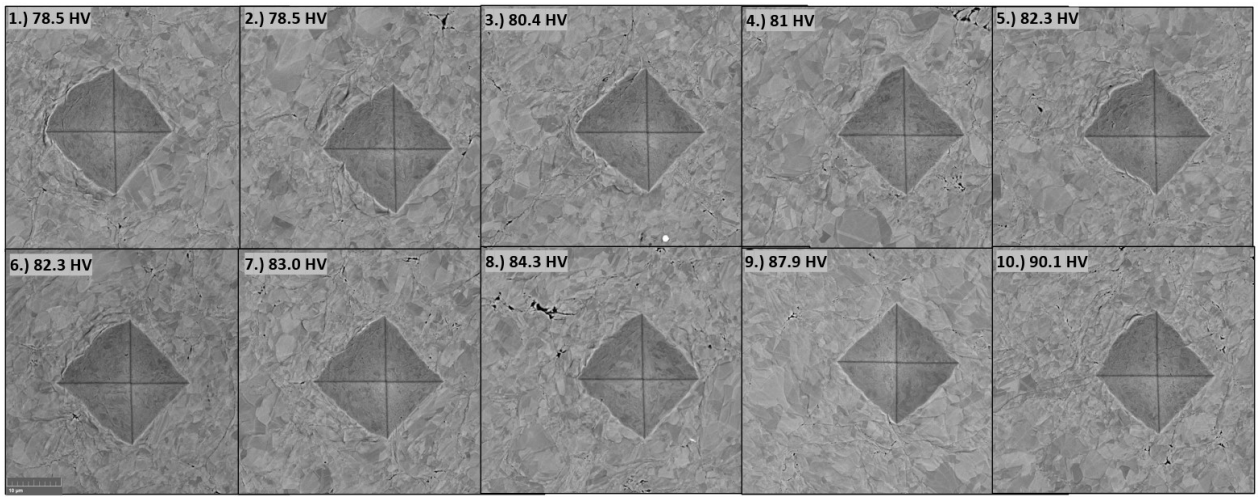


**Figure 64 High Magnification CS post-indentation images in spray direction with associated microhardness values (BSE).**

## A.1.0.2 Transverse Direction Cold Spray High Magnification Images

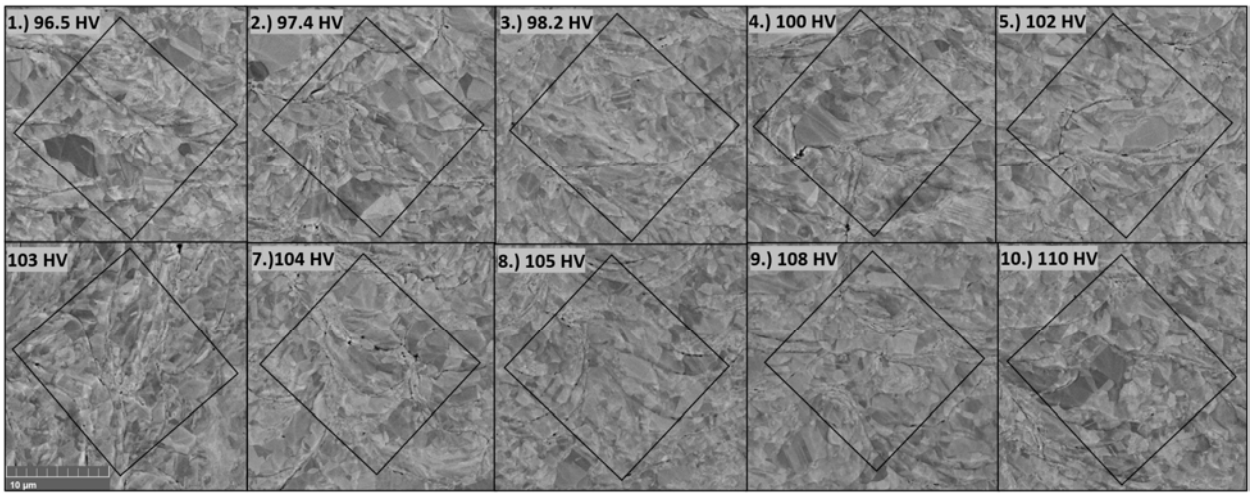


**Figure 65 High Magnification CS pre-indentation images in transverse direction with associated microhardness values (BSE).**

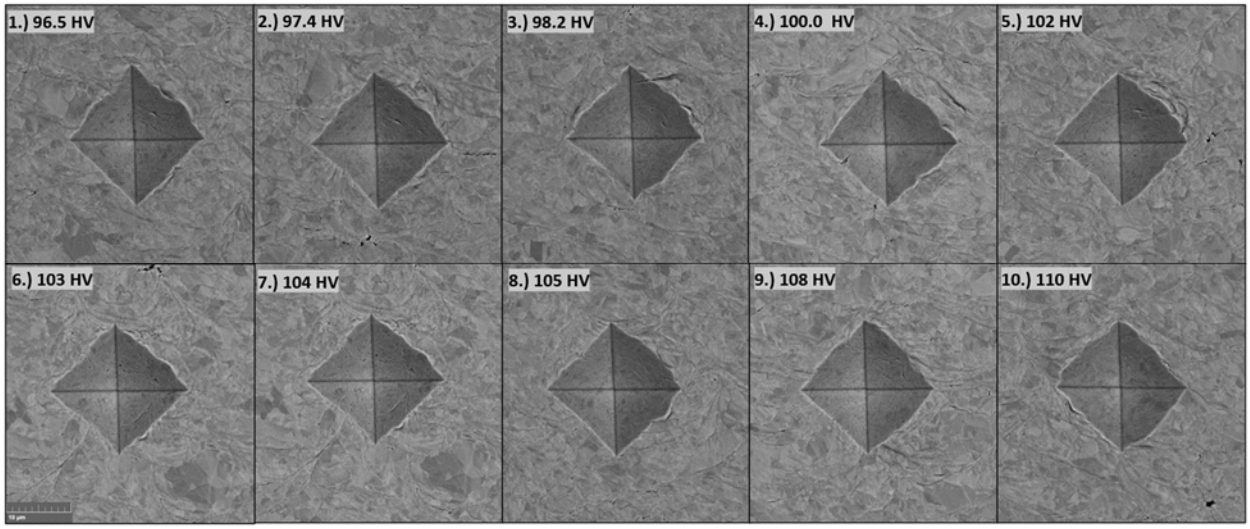


**Figure 66 High Magnification CS post-indentation images in transverse direction with associated microhardness values (BSE).**

## A.1.0.3 EBSD Array Cold Spray Indentation Images

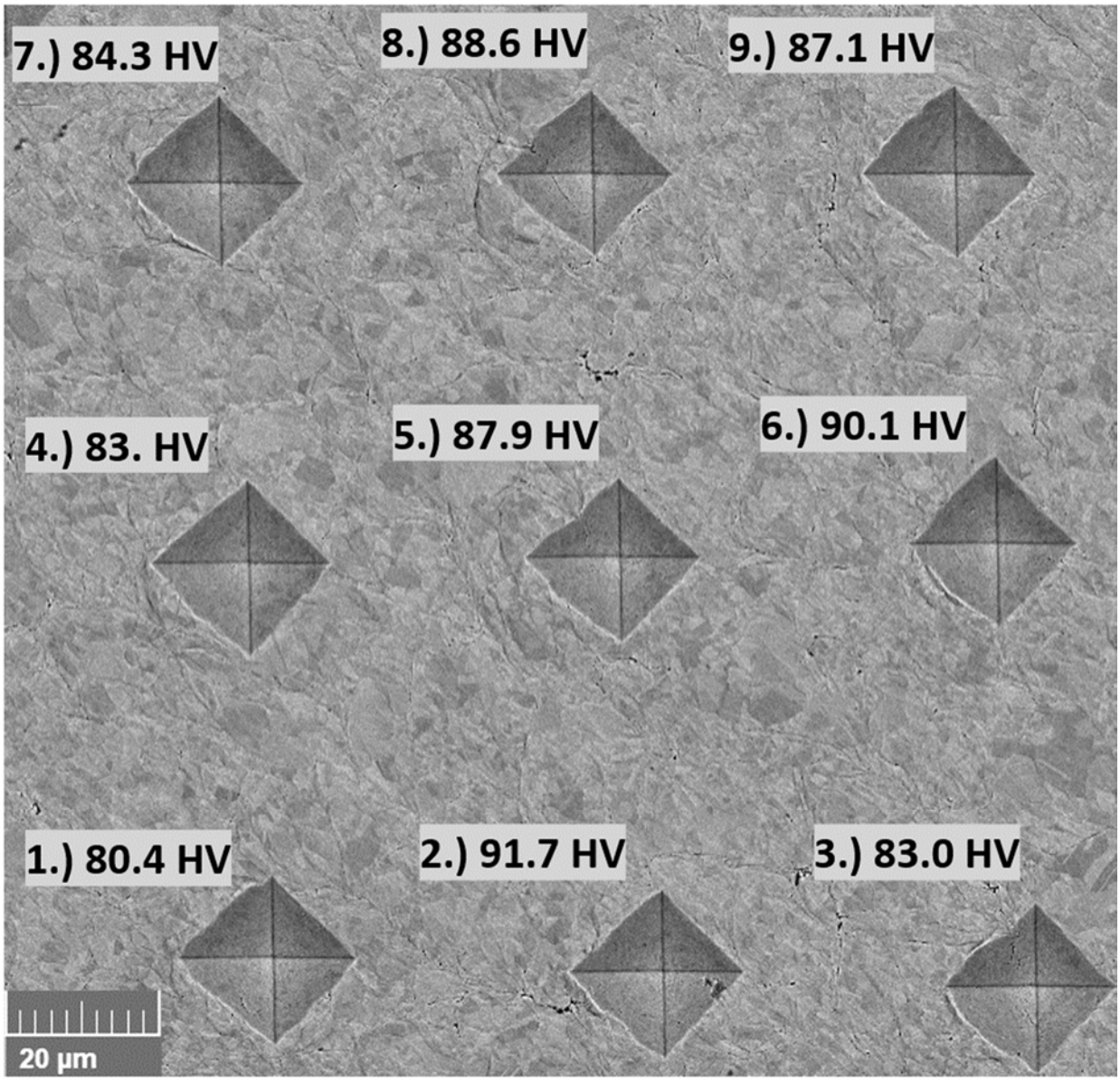


**Figure 67 Post-indentation CS image of EBSD 3x3 Array in spray direction with associated microhardness values (BSE).**

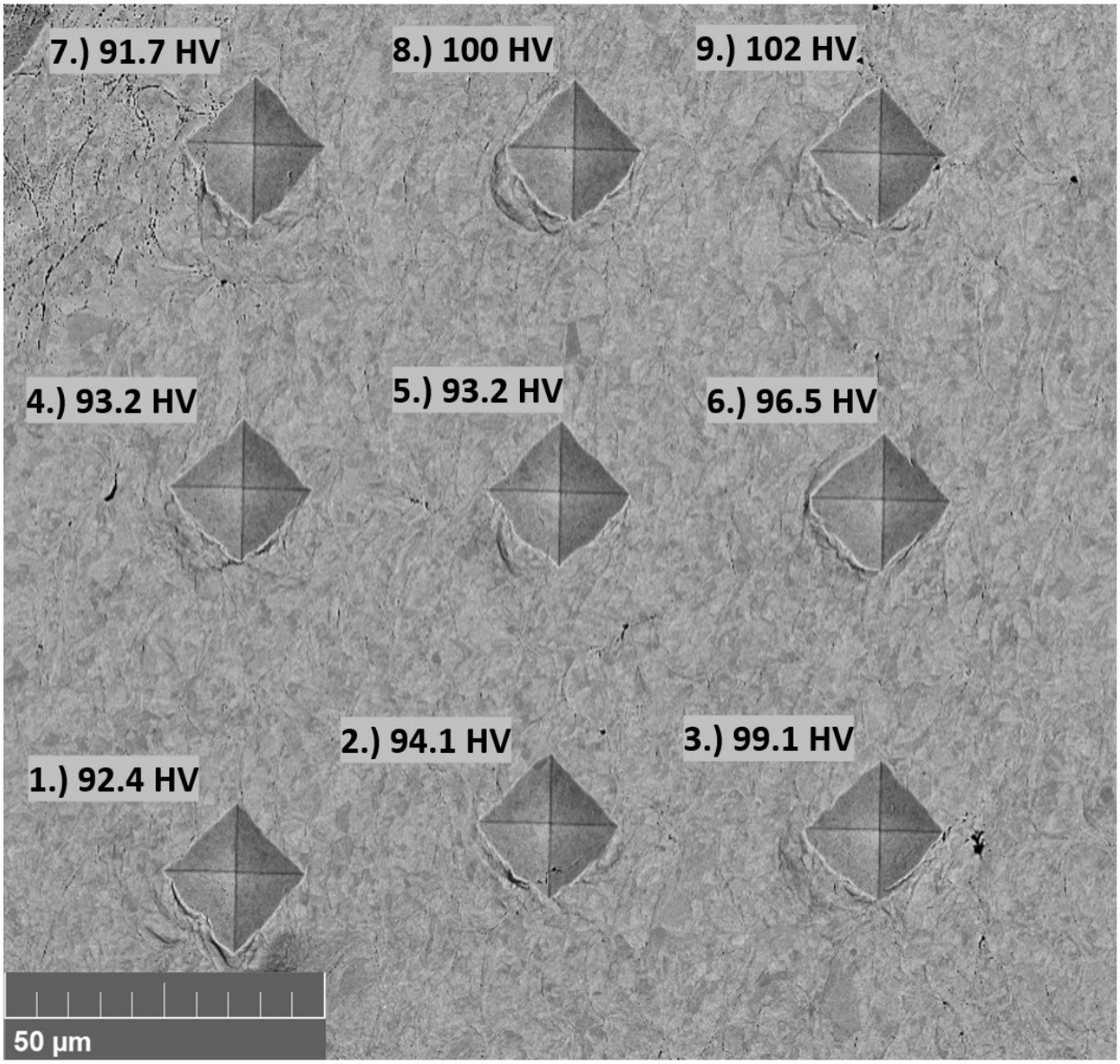


**Figure 68 Post-indentation CS image of EBSD 3x3 Array in transverse direction with associated microhardness values (BSE).**

## A.1.0.4 Low Magnification Indentation Images

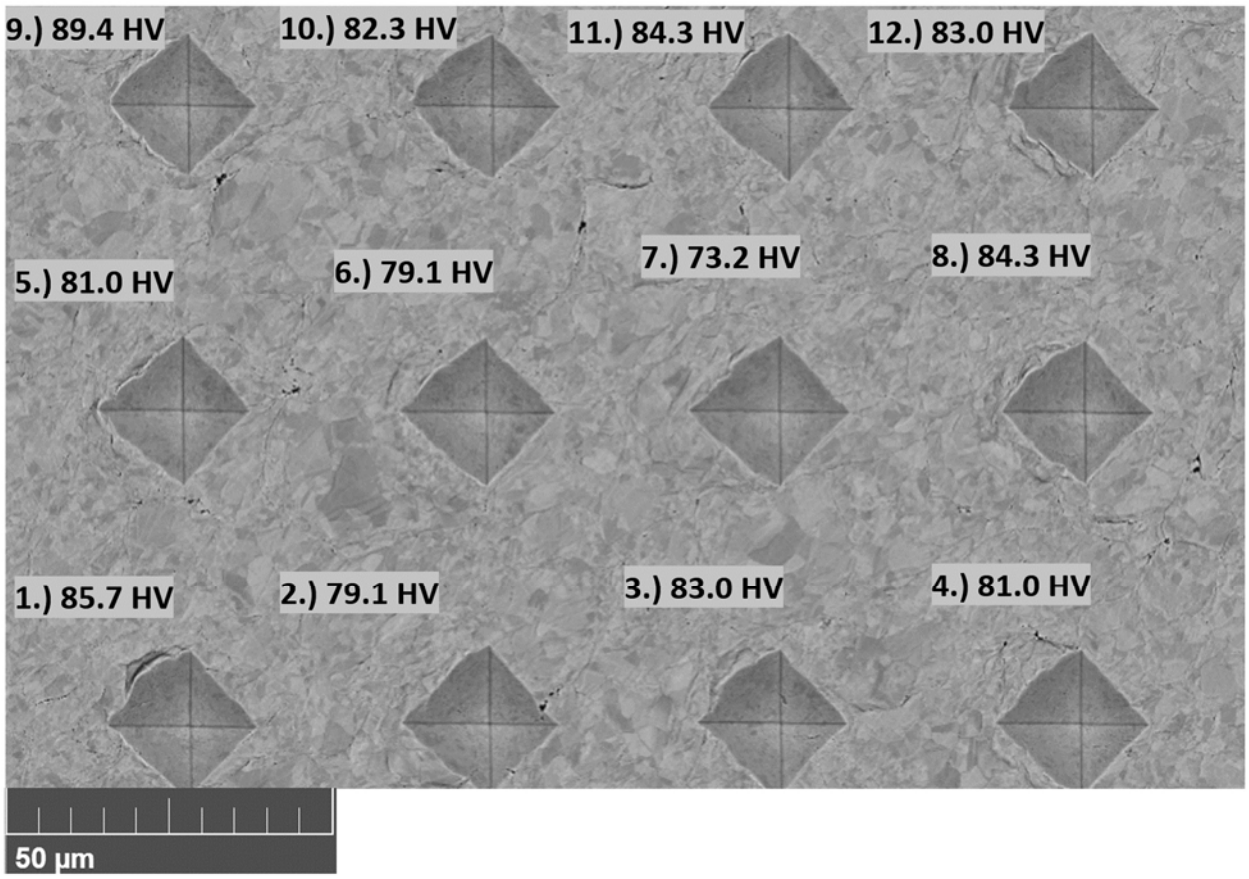


**Figure 69 Post-indentation CS image of low magnification 4x3 Array in spray direction with associated microhardness values (BSE).**

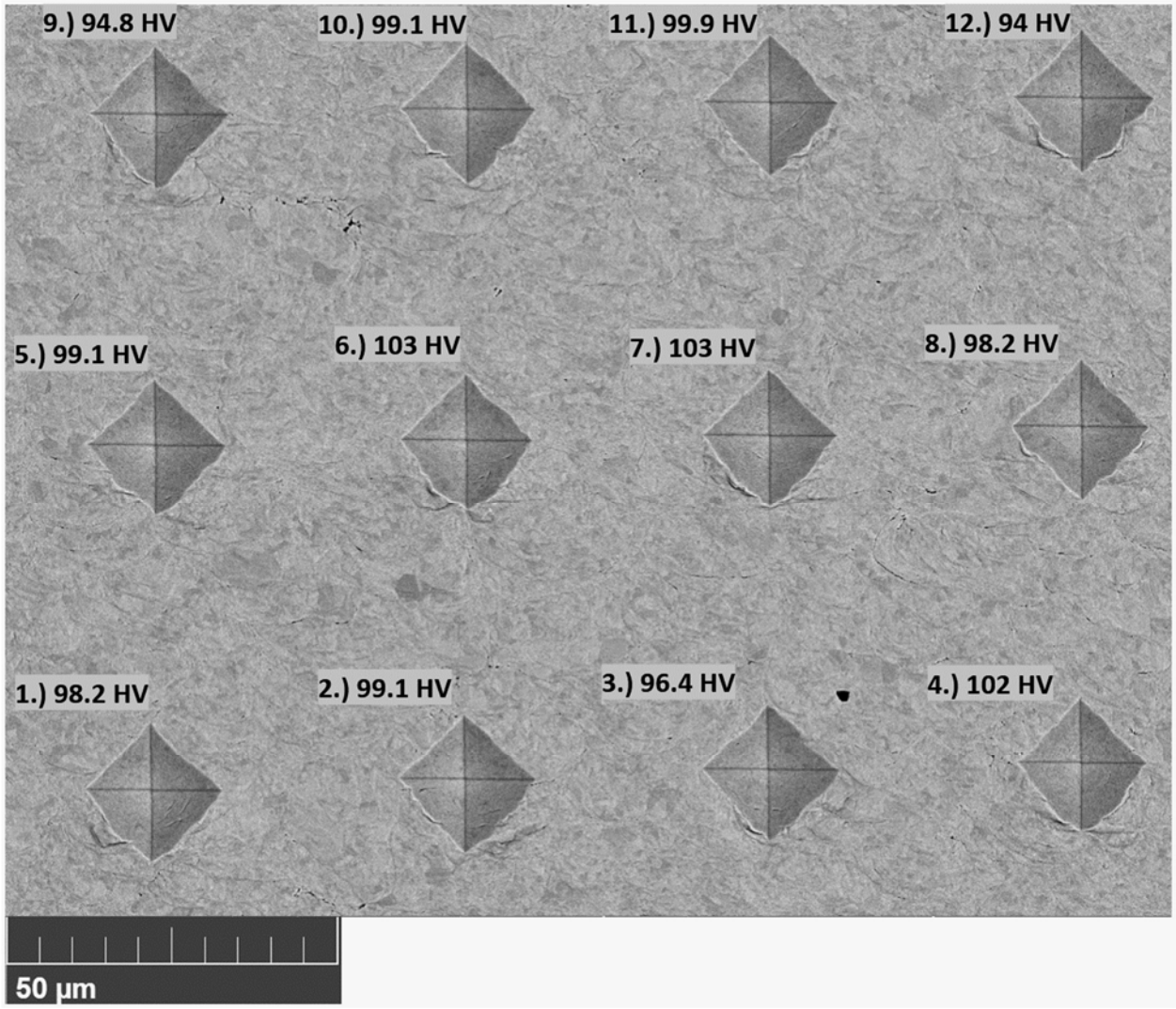


**Figure 70 Post-indent CS image of low magnification 4x3 array in transverse direction with associated microhardness values (BSE).**

## A.2.0 Cold Rolled Microstructural Characterization

An attempt was made to characterize 90% reduction CR specimens as a part of this research and the same experimental procedure was conducted. However, significant errors likely stemming from sample preparation arose during the process and the resulting microhardness values were too variable to have any confidence in the data. The figures and indentation data are shown below.

Figure 71 shows a micrograph of a CR specimen manufactured from the same pressed powder. The pressed powder compact was rolled until a 90% reduction in thickness was achieved. The specimen micrographs are oriented in the normal direction in which the pressed powder compact touched the rollers. Highly deformed grains are present throughout the microstructure with multiple regions that exhibit similar characteristics as the HDR's of CS. The microstructure appears to be considerably more homogenous than the sprayed material. Most of the grains within the image fall within 2 to 10 μm in size but some were less than a nanometer. The same tie-dye structure seen in the sprayed material which is indicative of a bent crystal is also slightly visible and is indicated in Figure 71. The EBSD data also shows the bent structure with clear gradients visible throughout the image. Figure 72 is a higher magnification micrograph with the region outlined in Figure 71. In Figure 72, the roughly polished microstructure is more apparent with a dimple indicated that may be an artifact of mechanical polishing.

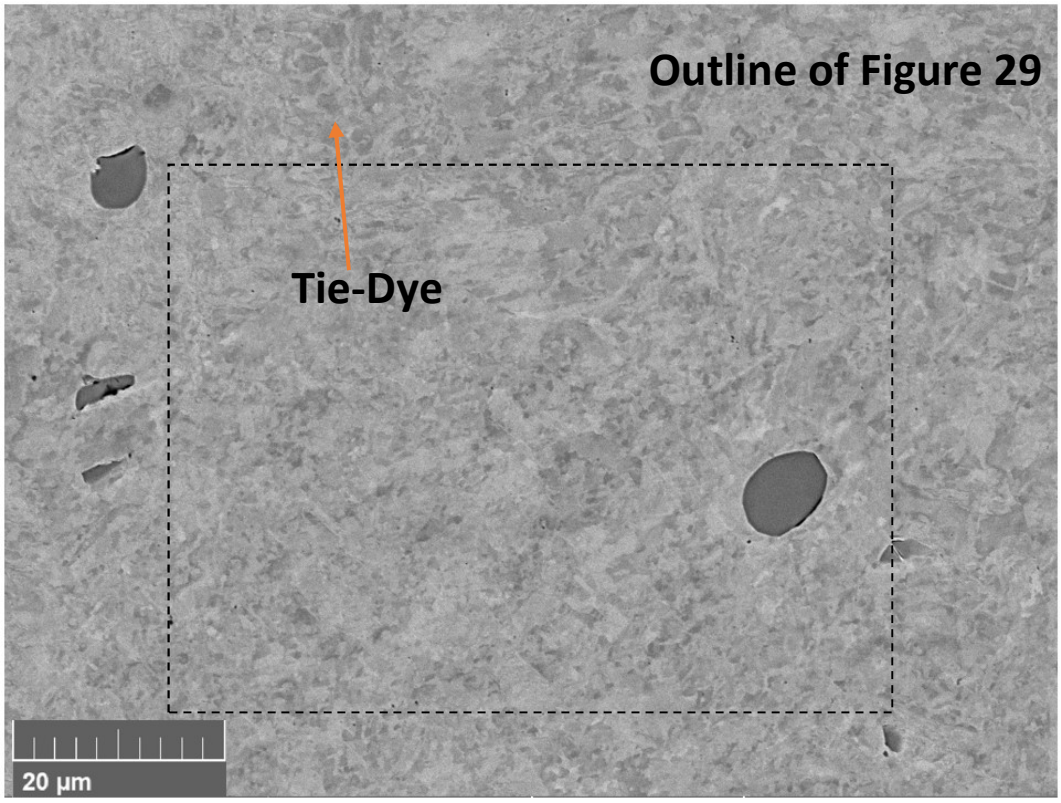


**Figure 71 BSE micrograph of CR specimen oriented in the normal direction. Arrow indicates tie-dye grain structure.**

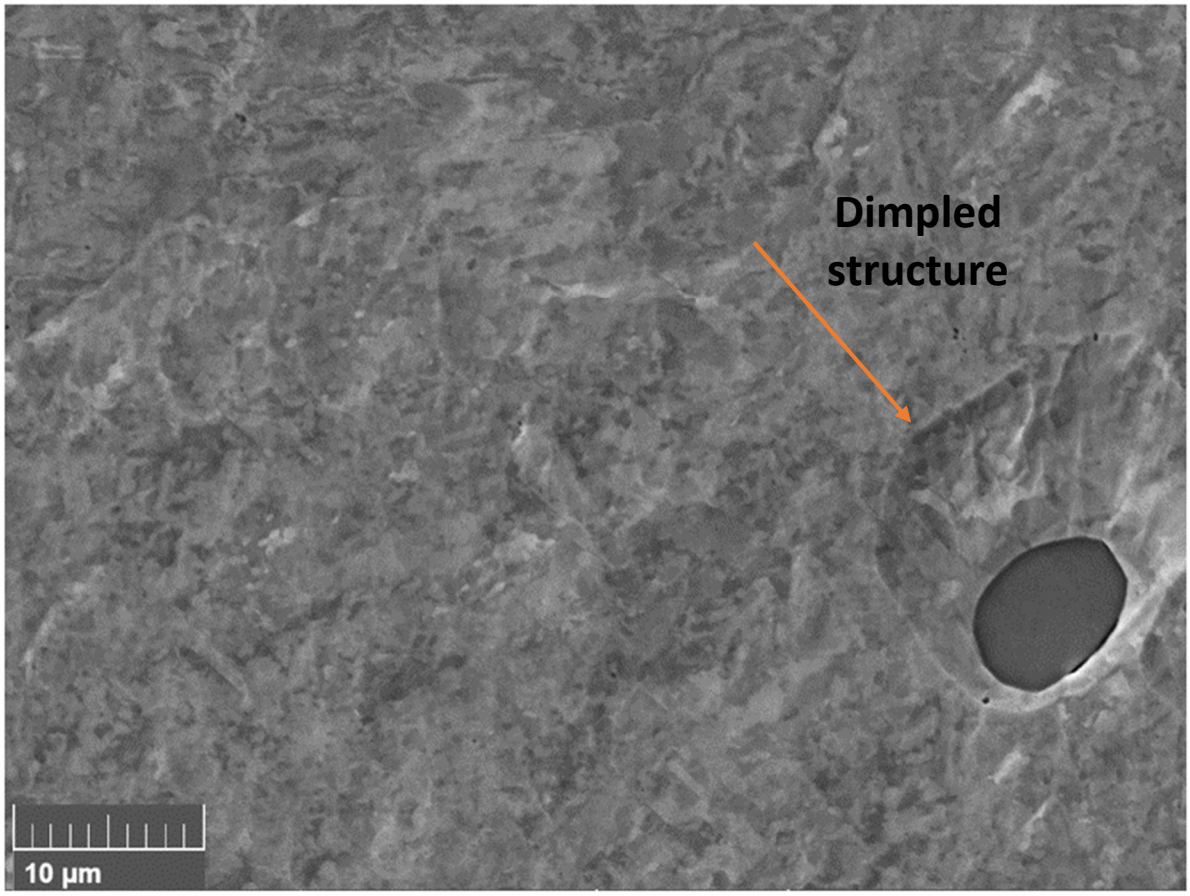


**Figure 72 SE micrograph of CR specimen. Arrow indicates dimple structure from possible mechanical pullout during polishing.**

## A.2.1 Cold Rolled High Magnification Imaging and Indentation

The high magnification images and associated indents showed considerable variability between microhardness with 63.2 HV for the lowest value and 124 HV for the highest microhardness value. Figures 73 and 74 are the high magnification images and their respective indents taken for the rolled material. The high variability in the indent data suggested there was likely substantial error in the sample preparation process.

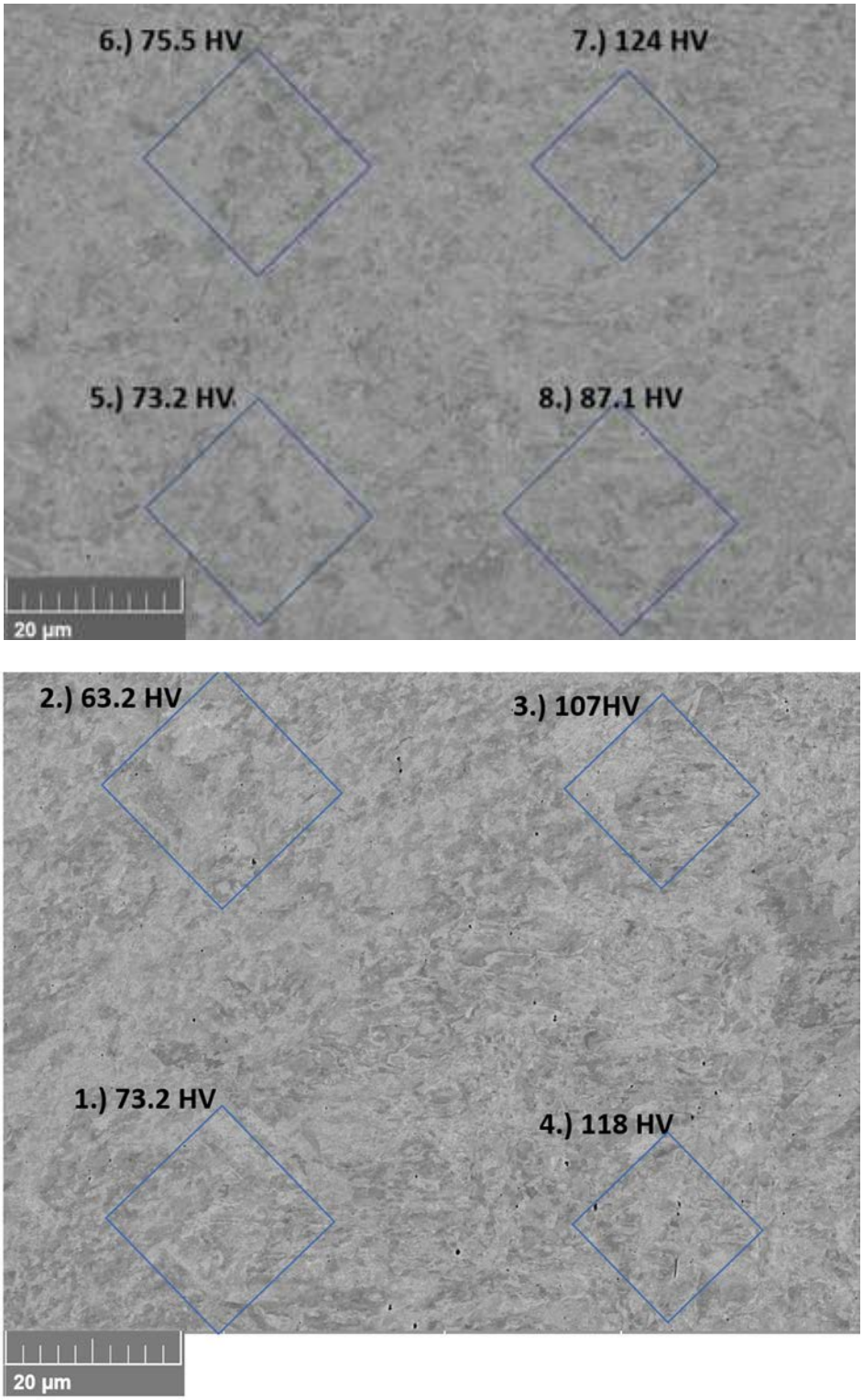


**Figure 73 BSE Micrograph of 8 microhardness indent outlines for CR normal direction specimen. Each outline is numbered with their associated microhardness value (BSE).**

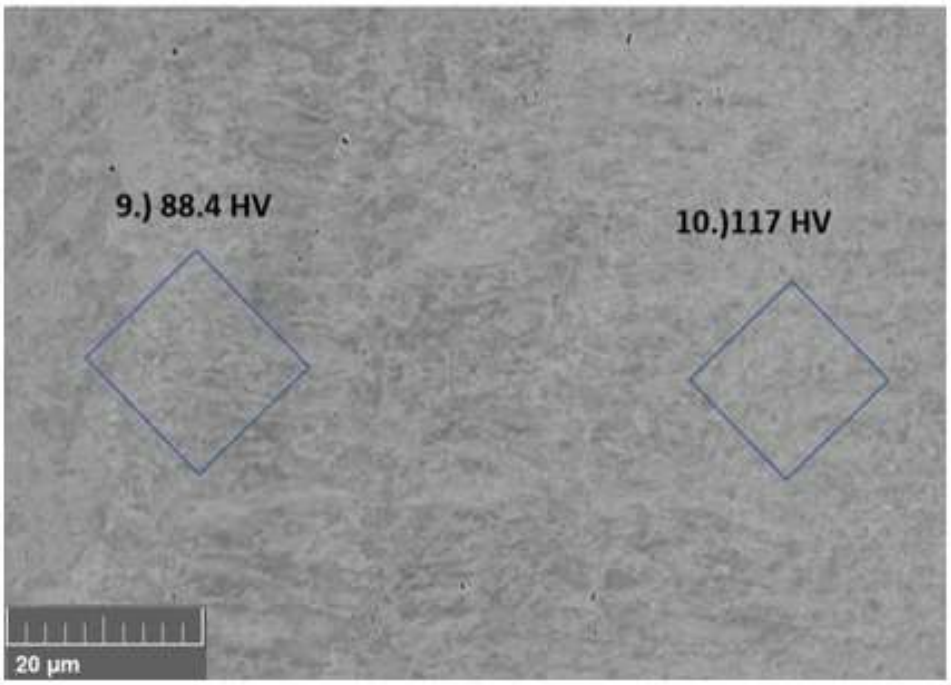


**Figure 74 BSE Micrograph of 2 microhardness indent outlines for CR normal direction specimen. Each outline is numbered with their associated microhardness value.**

## A.2.2 Cold Rolled EBSD and Indentation Arrays

Figure 75 shows an EBSD band contrast image and pole figure for the CR specimen. The pole figure reveals a considerably different grain structure than the sprayed or pressed powder materials. The high reduction rolling created flat and elongated grains with bent crystals. The pole figure also shows the microstructure appears to be separated by three distinct regions with much of the left side oriented in the 001 crystallographic direction and colored in red. The center of the micrograph contains mostly purple and blue coloring with heavily shaded gradients between the 111 and 001 crystallographic directions. The right third of the figure shows the most similar grain structure to the CS specimens with smaller grains. Figures 76 and 77 contain the 3x3 indent array with outlines over band contrast and inverse pole figures respectively. The indent values do not appear to show the same linear correlation between hardness and grain refinement as the CS specimens.

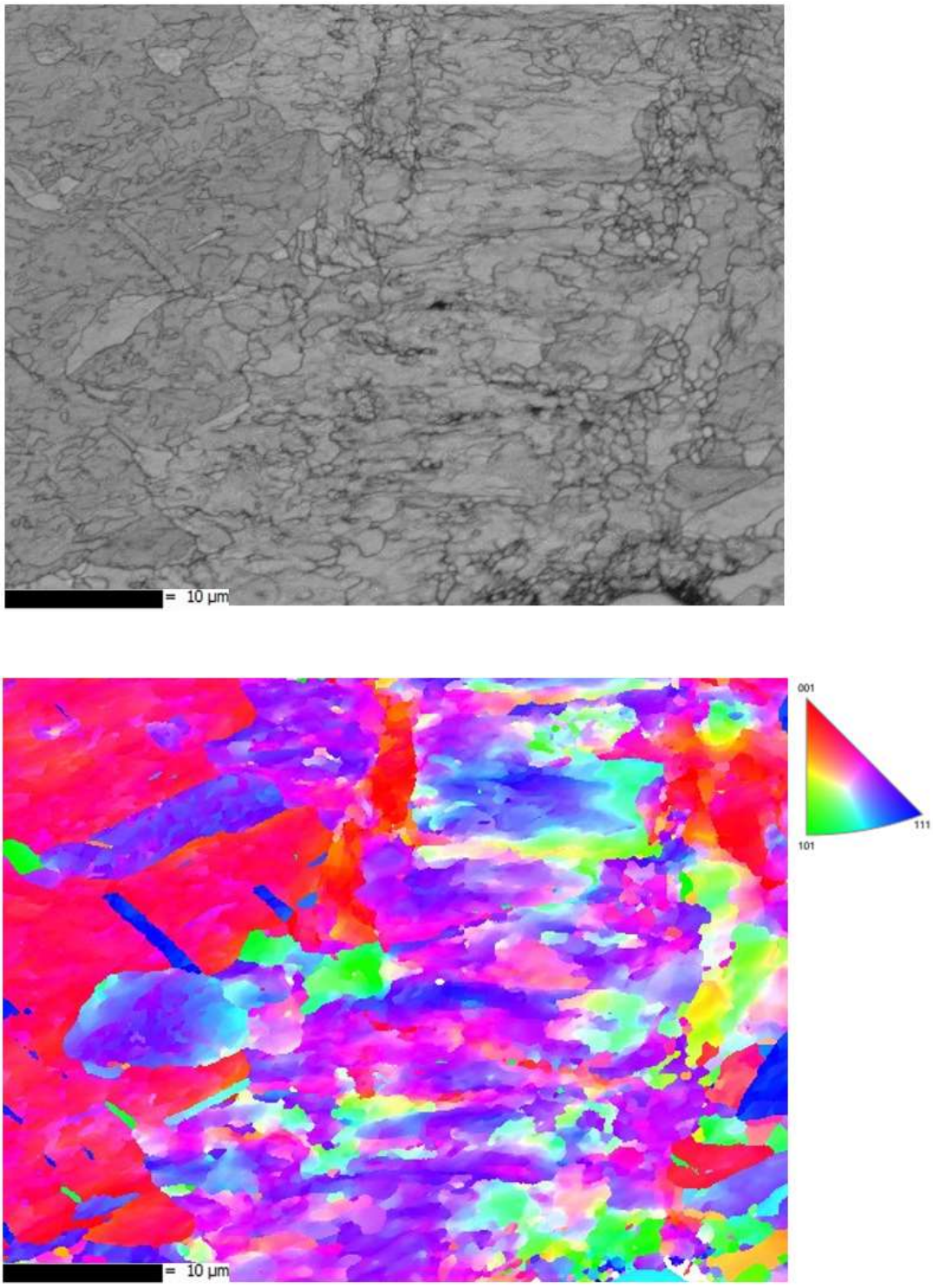


**Figure 75 CR specimen oriented in normal direction - (Top) Band contrast image - (Bottom) Z-Direction Pole figure.**

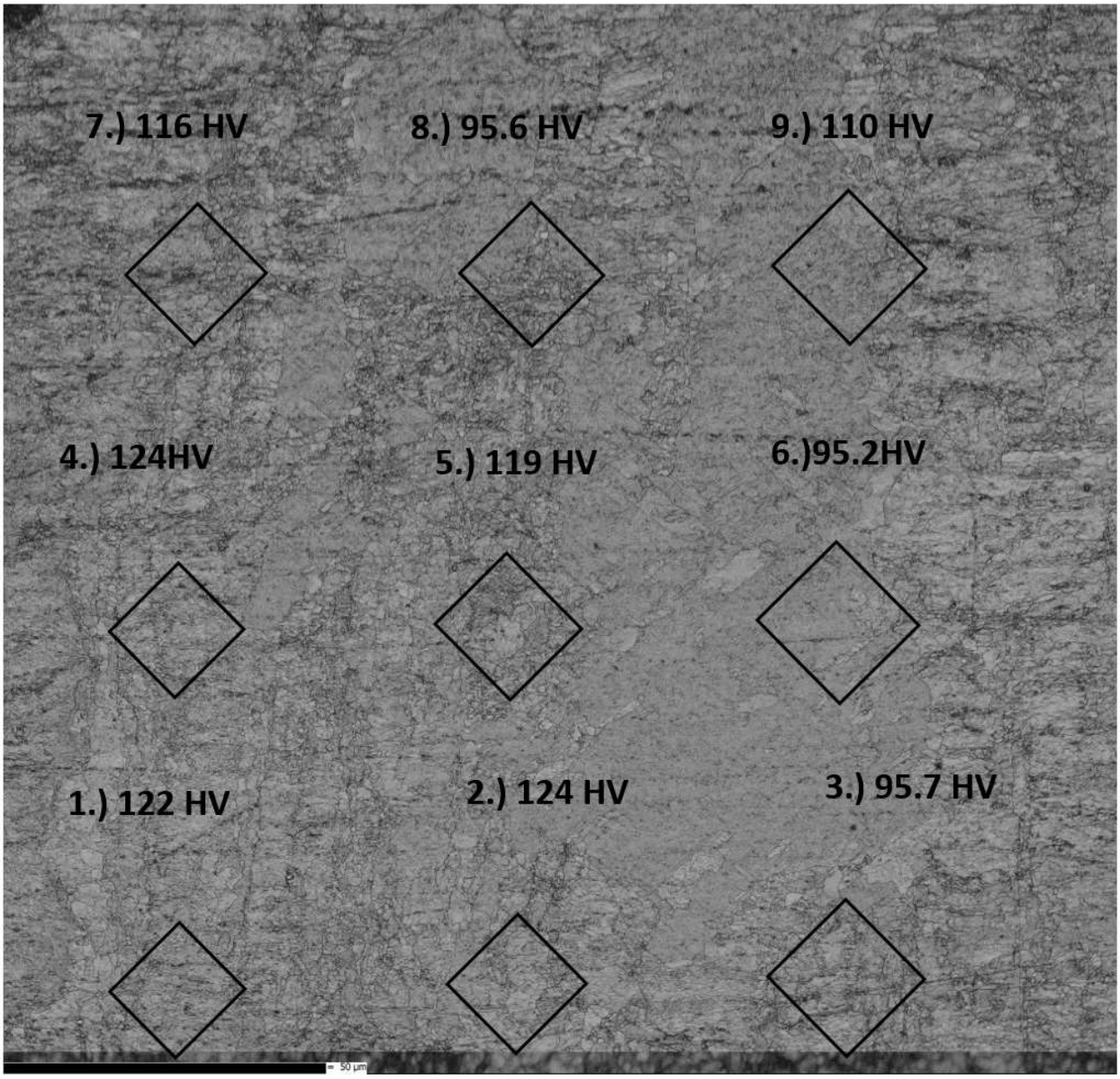


**Figure 76 Band contrast image of normal direction CR specimen with indent outline for 3x3 array and associated Vickers microhardness values.**

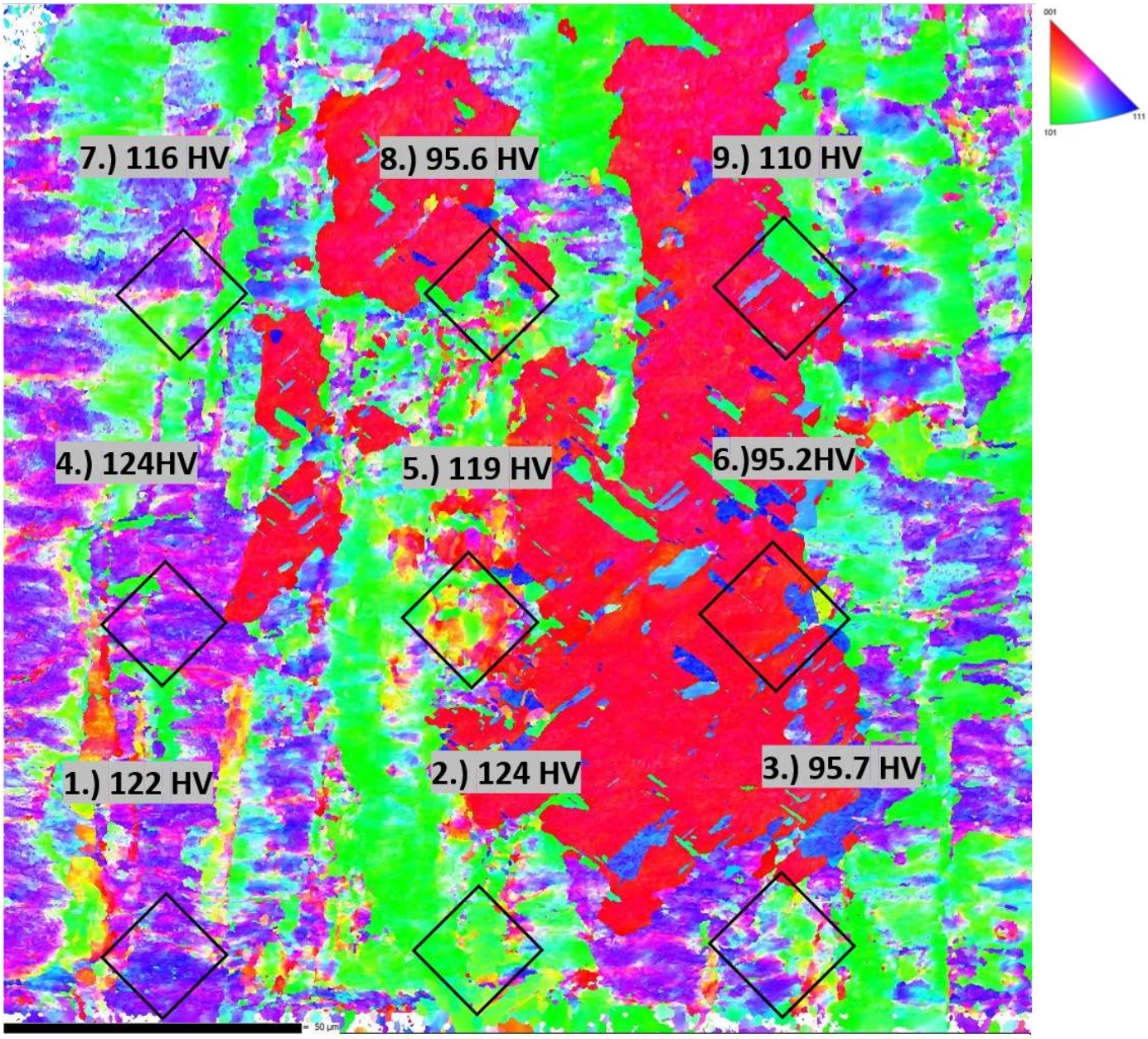


**Figure 77 Z-Direction EBSD Pole figure for normal direction CR specimen with indent outline for 3x3 array and associated Vickers microhardness values.**

## A.2.3 Cold Rolled Low Magnification Indentation Arrays

Figure 78 is the 3x3 array of indents taken in BSE with a larger FOV to capture more data. This array of indents was taken in a different area of the sample and produced slightly less variability but lower hardness overall. There is not a clear indicator to which type of grain structure produces which indent value.

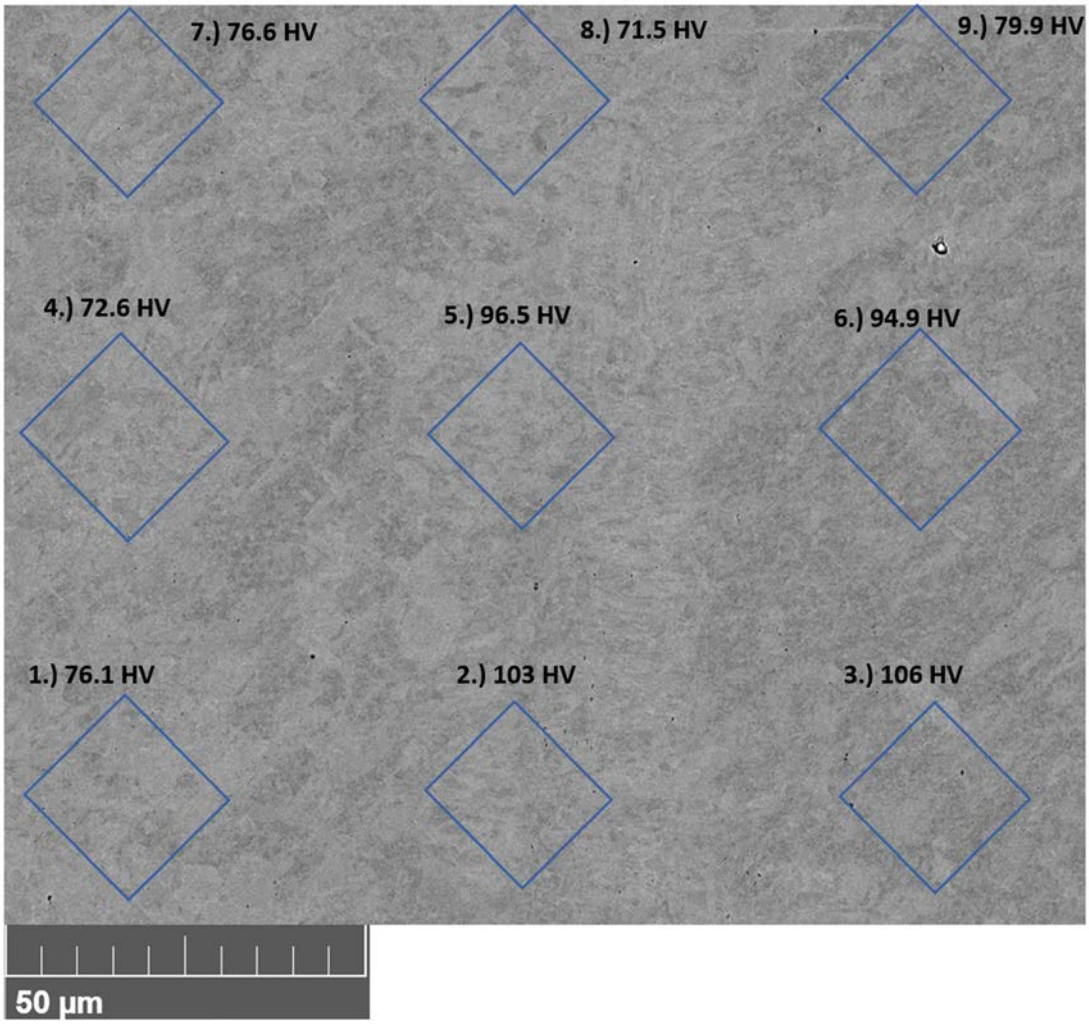


**Figure 78 CR specimen with indent outline for 3x3 array and associated Vickers microhardness values (BSE).**

## A.2.4 Cold Rolled Hardness Data

The following (Tables 12-14) are the microhardness data and associated statistics for the CR specimen. Overall, the data was too inconsistent to draw any meaningful conclusions and future work comparing CS to CR using the suggested improved methodology would prove valuable.

**Table 12 Associated Vickers microhardness data for CR high magnification images.**

| **Indent Number** | **Vickers Hardness Value** | **Statistics** | |
|---|---|---|---|
| **1** | 73.2 | **Average** | 92.66 |
| **2** | 63.2 | | |
| **3** | 107 | **High** | 124 |
| **4** | 118 | | |
| **5** | 73.2 | **Low** | 63.2 |
| **6** | 87.1 | | |
| **7** | 124 | **Standard Deviation** | 22.09 |
| **8** | 75.5 | | |
| **9** | 88.4 | **Variation Coefficient** | 23.83 |
| **10** | 117 | | |

**Table 13 Associated Vickers microhardness data for CR EBSD images.**

| Indent Number | Vickers Hardness Value | Statistics | |
|---|---|---|---|
| **1** | 122 | **Average** | 111.3 |
| **2** | 124 | | |
| **3** | 95.7 | **High** | 124 |
| **4** | 124 | | |
| **5** | 119 | **Low** | 95.2 |
| **6** | 95.2 | | |
| **7** | 116 | **Standard Deviation** | 12.6 |
| **8** | 95.6 | | |
| **9** | 110 | **Variation Coefficient** | 11.3 |

**Table 14 Associated Vickers microhardness data for CR low magnification images.**

| Indent Number | Vickers Hardness Value | Statistics | |
|---|---|---|---|
| **1** | 76.1 | **Average** | 86.24 |
| **2** | 103 | | |
| **3** | 106 | **High** | 106 |
| **4** | 72.6 | | |
| **5** | 95.6 | **Low** | 71.5 |
| **6** | 94.9 | | |
| **7** | 76.6 | **Standard Deviation** | 13.6 |
| **8** | 71.5 | | |
| **9** | 79.9 | **Variation Coefficient** | 15.7 |